ornl

ORNL/Sub/84-47992/1

OAK RIDGE NATIONAL LABORATORY

MARTIN MARIETTA

19980513 136

High Temperature Coating Study to Reduce Contact Stress Damage of Ceramics

Final Report

J. Schienle and J. Smyth

Prepared by
Garrett Turbine Engine Company
A Division of Garrett Corporation
2739 East Washington Street
P.O. Box 5217
Phoenix, Arizona 85010
Under Subcontract 86X-47992C

U61958

Accession Number: 1958

Publication Date: Mar 01, 1987

Title: High Temperature Coating Study to Reduce Contact Stress Damage of Ceramics

Personal Author: Schienle, J.; Smyth, J.

Corporate Author Or Publisher: Garrett Turbine Engine Co., 2739 E. Washington, St., Phoenix, AZ 85010 Report Number: ORNL/Sub/84-47992/1

Descriptors, Keywords: Evaluation Microstructure Zirconium Yttrium Oxidation Friction Stress Heat Engine SiC Si3N4 Coating Test Measurement Property Strength Silicon Carbide Nitride

Pages: 098

Cataloged Date: Oct 10, 1989

Contract Number: DE-AC05-84OR21400

Document Type: HC

Number of Copies In Library: 000001

Record ID: 20858

Source of Document: NTIS

HIGH TEMPERATURE COATING STUDY TO REDUCE
CONTACT STRESS DAMAGE OF CERAMICS

J. Schienle and J. Smyth

Date Published — March 1987

FINAL REPORT

TABLE OF CONTENTS

LIST OF ILLUSTRATIONS

LIST OF ILLUSTRATIONS

LIST OF ILLUSTRATIONS

LIST OF ILLUSTRATIONS

LIST OF TABLES

CERAMIC TECHNOLOGY FOR ADVANCED HEAT ENGINES PROJECT

J. Schienle, J. Smyth

ABSTRACT

Silicon nitride (Si_3N_4) and silicon carbide (SiC) ceramics are susceptible to contact stress damage at ceramic component interfaces in gas turbine engines. The objective of this research program was to develop adherent coating compositions and procedures that will improve contact-stress damage resistance of Si_3N_4 and SiC.

Yttria (Y_2O_3) stabilized zirconia (ZrO_2) coatings were applied by electron beam - physical vapor deposition (EB-PVD) to three substrate materials: reaction bonded Si_3N_4 (RBSN), sintered Si_3N_4, and sintered SiC (SSC). Several controlled substrate pretreatments (both mechanical and chemical) were used to aid in obtaining a better understanding of the mechanisms of coating adherence. Each coating/substrate system was evaluated for coating adherence before and after oxidation exposure. The coating/substrate interfaces were evaluated for microstructural characteristics. Based on the results, pretreatment and coating approaches projected to improve coating adherence were selected. Specimens were prepared to evaluate the coating adherence before and after oxidation exposure. The systems exhibiting the best coating adherence after oxidation exposure were identified. Additional specimens for each of these systems were prepared for analysis of the coating thermal spall resistance, friction, and contact damage resistance. The friction and contact damage resistance of uncoated RBSN, SSN, and SSC were also evaluated.

1.0 INTRODUCTION

Significant improvements in turbine engine operating efficiencies can be obtained through the use of uncooled ceramic components at material temperatures above those attainable with high-temperature metal alloys. Both The Department of Energy (DOE) and The Department of Defense (DOD) advanced turbine engine programs provide evidence that improved performance can be realized. However, these programs have also demonstrated that an expanded technology base is required to achieve reliable, cost-effective ceramic components.

During the past decade, a number of programs have focused on introducing ceramic materials, such as silicon nitride (Si_3N_4) and silicon carbide (SiC), into gas turbine engines. Due to the hard, brittle nature of ceramic materials, high localized surface stresses in contact regions do not redistribute as in metals. In many cases,

1

the localized stresses exceed the baseline strength of the ceramic, thus damaging the surface of a component and reducing its strength. As a result, contact stress damage can cause ceramic turbine engine components to fail unpredictably and prematurely.

Finite-element analyses of ceramic contacts show that localized tensile stresses can occur under certain contact conditions. The analytically derived stress distribution is shown schematically in Figure 1. For uniaxial loading, tensile stresses are generated on the surface at the edges of the contact zone, but the magnitude is small compared to the compressive stress beneath the surface. However, when a sliding force is added (i.e., a bi-axial loading condition), a large tensile spike occurs on the surface at the trailing edge of the contact zone. Four of the factors controlling the magnitude of this tensile stress spike are

    o   Contact load
    o   Contact geometry
    o   Coefficient of friction
    o   Elastic moduli

NORMAL LOADING   BIAXIAL LOADING

TENSILE

STRESS DISTRIBUTION

COMPRESSIVE

CONTACT AREA

CONTACT AREA

TENSILE SPIKE

• LOCALIZED AT SURFACE

• TRAILING EDGE AT CONTACT

• AMPLITUDE DEPENDENT UPON FRICTION
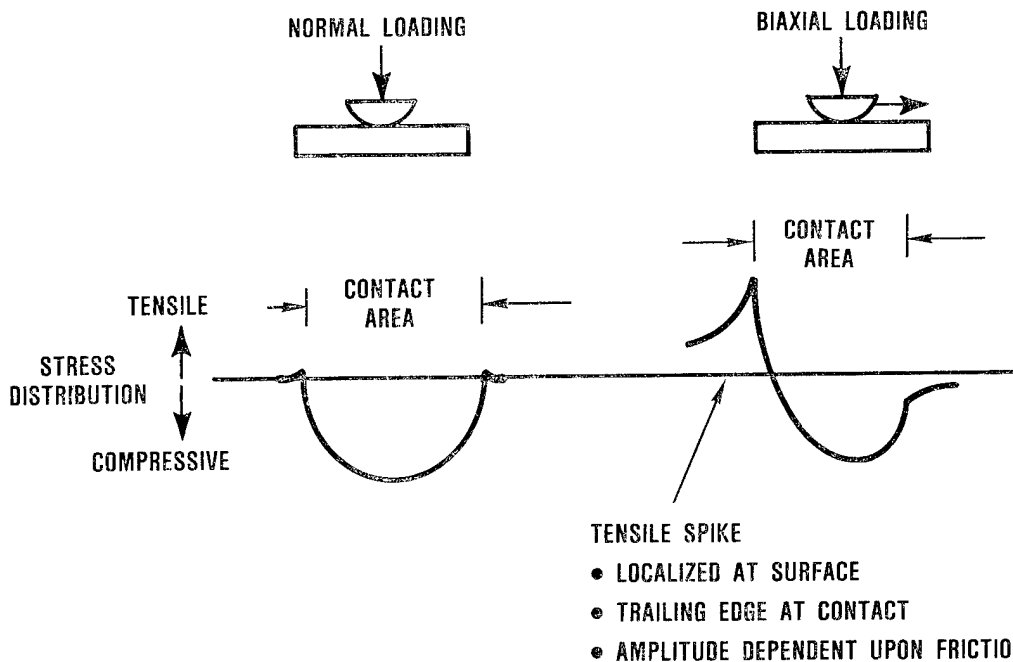
Figure 1. Biaxial loading generates a large tensile stress spike.

Contact load and contact geometry have a very significant effect on contact stresses and can be partially controlled through proper engine and component design, as well as through the control of dimensional tolerances of mating surfaces. In addition, significant benefits can be achieved if the sensitivity of ceramic components to contact stress damage can also be lessened by reducing the relative coefficient of friction (to reduce the sliding force component) and

the elastic moduli (to distribute the load over a larger area). A primary approach to controlling these factors is the use of coatings.

The feasibility of using ceramic coatings to improve the contact stress damage resistance of Si_3N_4 and SiC ceramics has been demonstrated using plasma sprayed oxide coatings[1]. However, the coating adherence was not adequate for long term use in gas turbine environments. The objective of this research program was to develop coating compositions and procedures that will yield long term adherence and reduce or eliminate contact-stress damage to Si_3N_4 and SiC ceramics.

This program used an alternate coating method, electron beam physical vapor deposition (EB-PVD), as the coating process because it offers good control of coating composition, thickness, and morphology. The coating composition selected for evaluation was 20 percent yttria (Y_2O_3) stabilized zirconia (ZrO_2). The Garrett Turbine Engine Company (GTEC) uses this EB-PVD coating composition as a thermal barrier coating (TBC) for metallic components. Also, the feasibility of using this coating on Si_3N_4 and SiC ceramics was demonstrated prior to the start of the program.

Three substrate materials were selected for this study: reaction bonded Si_3N_4 (RBSN), sintered Si_3N_4 (SSN), and sintered SiC (SSC).

The program was divided into four technical tasks:

o   Task 1 - Coating Adherence and Characteristics Investigation

o   Task 2 - Advanced Pretreatment and Coating Studies

o   Task 3 - Contact Stress Testing and Friction Measurements

o   Task 4 - Post-Contact Strength Measurements

2.0 SUMMARY

The objective of this research program was to develop adherent coating compositions and procedures that will reduce or eliminate contact-stress damage to Si_3N_4 and SiC heat engine components. The program was divided into four technical tasks:

o   Task 1 - Coating Adherence and Characteristics Investigation
o   Task 2 - Advanced Pretreatment and Coating Studies
o   Task 3 - Contact Stress Testing and Friction Measurements
o   Task 4 - Post-Contact Strength Measurements

This four task approach addressed the application, adherence, and contact load tolerance of yttria stabilized zirconia applied by electron beam - physical vapor deposition (EB-PVD). The substrate materials evaluated were reaction bonded Si_3N_4 (RBSN), sintered Si_3N_4 (SSN), and sintered SiC (SSC). During Task 1, coating adherence evaluations were conducted to obtain an increased understanding of the coating adherence mechanisms. Several substrate pretreatments were evaluated for their effect on as-coated adherence and adherence after static air oxidation. The substrate pretreatments included diamond grinding (baseline), lapping, oxidation, etching, and sputtering interlayers of Al, Si, Mo, or Ti. The Task 1 adherence information was then used in Task 2 to develop coating/substrate systems with improved adherence characteristics. The Task 2 pretreatment approaches focused on preventing interfacial oxidation and improving the mechanical adherence. The former approach included the application of oxygen diffusion barrier interlayers of Al_2O_3, AlN, or mullite; the latter included roughening the substrate surface before coating. Other pretreatments evaluated included high purity interlayers (Chemical Vapor Deposition (CVD) SiC) and ion mixing. The adherence of ZrO_2 deposited at higher temperatures and EB-PVD mullite coatings were also evaluated. The Task 2 systems exhibiting the best coating adherence were then evaluated for contact damage resistance in Tasks 3 and 4.

TASK 1

Coating studies conducted under Task 1 demonstrated that the EB-PVD process could produce adherent coatings of Y_2O_3 stabilized ZrO_2 on machined surfaces of RBSN, SSN, and SSC (Baseline). Analyses of coating/substrate interfaces suggested the presence of a thin layer of zirconium silicate at the interface. Neither oxidation or etching pre-treatments of the machined substrates changed the level of coating adherence relative to the baseline. All of the sputtered interlayers produced less adherent coatings relative to the baseline.

A major conclusion of Task 1 was that mechanical mechanisms contribute significantly to overall coating adherence. RBSN, which has the roughest surface of the materials evaluated due to its 15 percent residual porosity, consistently exhibited better adherence than SSN

and SSC substrates irrespective of substrate pretreatment. Also, lapping the machined substrates resulted in decreased adherence relative to the baseline. The effect of lapping was more significant for SSN and SSC than for RBSN. This difference was not surprising since lapping should not change the frequency and distribution of the RBSN's surface porosity. These results support the predominance of mechanical adherence for RBSN.

Static air oxidation of coated specimens significantly degraded the coating adherence for all coating/substrate systems. Analyses of coating/substrate interfaces indicated that the adherence loss was caused by additional growth of the zirconium silicate bond layer. The adherence loss observed for the sputtered interlayer specimens was probably due to oxidation of the metallic interlayer. Since ZrO_2 is known to be permeable to oxygen, oxidation of the Si_3N_4 and SiC substrates was anticipated. Although the oxidation and interlayer pretreatments were aimed at inhibiting degradation in interfacial bonding, these pretreatments were unsuccessful in preventing adherence loss. It was concluded that approaches aimed at reducing or eliminating the oxidation problem should be emphasized in subsequent tasks.

TASK 2

Coating studies under Task 2 demonstrated the feasibility of using an oxygen diffusion barrier between the EB-PVD ZrO_2 coating and the substrate to prevent adherence loss on oxidation. CVD Al_2O_3 interlayers on RBSN yielded excellent as-coated adherence which was retained after 100 hours at 1200C in static air. CVD AlN interlayers on RBSN resulted in relatively poor initial adherence but excellent adherence after oxidation. The AlN evidently oxidized to form Al_2O_3 which improved adherence. A sol-gel Al_2O_3 interlayer worked best for SSN and SSC yielding fair adherence both before and after oxidation.

Task 2 studies also demonstrated that ZrO_2 adherence could be improved significantly by roughening the substrate surface. Laser-texturing improved both the as-coated and oxidized coating adherence for SSC. This was particularly encouraging since no interlayer was used to prevent oxidation at the interface. Results were not as encouraging for laser textured RBSN and SSN. However, the surface cavities were much deeper than on SSC and were not successfully filled in with ZrO_2 which suggests potential for improvement. One negative aspect of laser texturing is that improved coating adherence is accompanied by a strength loss associated with the surface cavities.

The other Task 2 pretreatment and coating approaches did not provide improved coating adherence. High purity CVD SiC interlayer and ion mixing pretreatments decreased coating adherence. Depositing EB-PVD ZrO_2 at a higher temperature (1040C rather than 980C) did not have any effect on coating adherence and attempts to deposit mullite coatings by EB-PVD were unsuccessful (the silica in the mullite evaporated more easily than the alumina resulting in silica rich coatings).

The two pretreatments yielding the best ZrO_2 coating adherence for each substrate were selected for testing in Tasks 3 and 4. Emphasizing the coating adherence after oxidation, the pretreatments shown in Table 1 were selected.

Table 1. Pretreatments selected for tasks 3 and 4

RBSN	SSN	SSC
CVD Al_2O_3	sol-gel Al_2O_3	sol-gel Al_2O_3
CVD AlN	laser machining	laser machining

TASK 3

During Task 3, each coating/substrate system was evaluated for strength, thermal spalling resistance, and friction.

The strength characteristics were determined by comparing the post-oxidation (1200C for 100 hours) flexure strength of each coating/substrate system with the as-machined substrates. Laser-textured substrates were also evaluated since Task 2 results identified a strength loss associated with this process.

Both coated RBSN systems exhibited residual effects on strength. A strength loss was observed at room temperature which was recovered at elevated temperatures. At 1375C, both systems exhibited higher strengths than the baseline.

Both coated SSN systems exhibited a strength loss. However, the strength loss was due to the degradation of the SSN substrate during oxidation rather than to the pretreatment and/or coating procedures.

Both coated SSC system exhibited no significant changes in strength relative to as-machined SSC.

The thermal spalling resistance of each coating/substrate system was evaluated using cyclic thermal exposures to 1000C and 1375C. The results were encouraging considering the large thermal expansion mismatch between the coating and the substrate. ZrO_2/CVD Al_2O_3/RBSN had the best spalling resistance (no spalling observed). ZrO_2/laser-textured SSN and ZrO_2/laser-textured SSC performed nearly as well, exhibiting only minor edge spalling in some cases during 1000C testing. ZrO_2/CVD AlN/RBSN exhibited relatively good spalling resistance; only one of four spalled during 1375C tests. ZrO_2/sol-gel Al_2O_3/SSN and ZrO_2/sol-gel Al_2O_3/SSC had poor spalling resistance. Limited spalling occurred during 1000C cyclic exposures, but frequent spalling occurred during the 1375C tests.

The friction characteristics of the substrate materials and each of the ZrO_2 coated systems were determined up to 1375C. Contact test procedures were used for friction assessment so the same specimens could be flexure tested for retained strength to assess contact damage resistance. First, the thresholds for contact damaging uncoated substrates were determined using a point contact geometry. Then, the friction characteristics of the coated systems were determined using

loading conditions below and above the thresholds for damaging the uncoated substrate (the coated specimens tested above the substrate damage thresholds were used to assess contact damage resistance under Task 4). When testing above the damage thresholds, frequent spalling was observed. The results suggested the coatings would not provide contact damage resistance under cyclic loading conditions.

Surprisingly, the ZrO_2 coatings had higher friction coefficients than the uncoated substrates, and the coefficients of friction increased with temperature. The higher friction coefficients relative to the uncoated substrate may have resulted from the SSC contact pin becoming embedded in the low modulus coating, which may create a plowing effect and increase apparent friction. A potential solution is to deposit a dense layer over the porous, compliant coating to inhibit the plowing effect. In addition, the increased friction at elevated temperature is due to the oxidation of the SSC contact pin. Therefore, the increased friction at elevated temperature would not be expected if the contact pins were also coated since two stable oxides would be in contact.

TASK 4

During Task 4, post-contact flexure test results demonstrated that the coatings can prevent contact damage.

No contact damage resulted from room temperature contact testing.

At 1000C contact damage was prevented in most cases. A few specimens did exhibited contact damage. In these few cases the coating remained adherent throughout testing. It appears that well bonded EP-PVD ZrO_2 coatings can transmit damage to the substrate under certain conditions.

During 1200C and 1375C contact testing, contact damage was prevented for all systems except for the ZrO_2/sol-gel Al_2O_3/SSN system. All specimens from this system spalled at 1200C and exhibited contact damage.

In conclusion, a technology base for depositing adherent EB-PVD Y_2O_3 stabilized ZrO_2 coatings on Si_3N_4 and SiC was developed. These EB-PVD coatings improved the contact damage resistance of Si_3N_4 and SiC. However, uncoated Si_3N_4 and SiC substrates also had much higher contact damage resistance than originally anticipated. Because of the high load conditions required to damage the uncoated substrate, coated specimen tested under the same severe conditions tended to exhibit coating spalling during the single cycle contact tests. Therefore, additional work is required to obtain coatings with cyclic durability. The coating technology developed under this program may have immediate applicability for impact resistance coatings or non-stick coatings in heat engines.

3.0 TECHNICAL PROGRESS SUMMARY

3.1 TASK 1 - COATING ADHERENCE AND CHARACTERISTICS INVESTIGATION

Task 1 focused on determining the chemical and mechanical mechanisms of coating adherence. Based on Task 1 results, coating approaches projected to improve the adherence of the EB-PVD zirconia were selected for Task 2, Advanced Pretreatment and Coating Studies.

3.1.1 Specimen Preparation and Inspection

The substrate materials used in this program were reaction bonded silicon nitride (RBSN)*, sintered silicon nitride (SSN)**, and sintered silicon carbide (SSC)***. RBSN and SSC were selected because substantial baseline strength and contact data were available. SSN was selected to provide a dense Si_3N_4 to compare with the porous RBSN. The substrate test bars for Task 1 were selected from existing stock at GTEC and were diamond ground with a 320-grit wheel. The test bars were 0.250 by 0.125 inches in cross section and at least 1.0 inch in length. Half of these specimens were lapped smooth on one surface. The variation in surface roughness between the diamond ground and lapped surfaces provided for an assessment of the contribution of mechanical factors to the overall adherence.

Each specimen received one of the nine pretreatments listed in Table 2.

Table 2. Task 1 precoating surface treatments

Surface Treatments	As-machined	Lapped
No Treatment	6	6
Light Oxidation[+]	6	6
Heavy Oxidation[+]	6	6
Sputter Etch[++]	6	6
Reactive Ion Etch[++]	6	6
Al Interlayer[++]	6	6
Si Interlayer[++]	6	6
Mo Interlayer[++]	6	6
Ti Interlayer[++]	6	6

108 specimens each of RBSN, SSN, and SSC (Total of 324 specimens)
[+]Pretreatment conducted at GTEC
[++]Pretreatment conducted at Temescal, Berkeley, CA

---

*RBN-104 from the AiResearch Casting Company (ACC) Torrance, California.
**Code 2 from ACC.
***Hexoloy SA from Sohio Engineered Materials, Niagara Falls, New York.

Specimens with no surface treatment were used as a baseline for comparison. Preliminary studies suggested that the EB-PVD zirconia coatings adhere relatively well to substrates with no pretreatment.

Light and heavy oxidation pretreatments were conducted to study the effect of growing a silica (SiO_2) layer on the substrate prior to zirconia coating. Since zirconia is permeable to oxygen, it was anticipated that the substrate would oxidize during post-coating heat treatment. The light and heavy oxidation pretreatments were static air exposures at 1000C for 1 hour and 1204C for 4 hours, respectively.

Sputter etching was conducted to study the effect of etching all silica off the substrate prior to coating. Due to heat generated during machining and lapping, minor oxidation of the substrate can occur. Each substrate was RF sputter etched with argon ions.

Reactive ion etching was conducted to determine the effect of removing material from the substrate surface. The reactive etching agent used was silicon tetrafluoride (SiF_4).

Four sputter deposited coatings, nominally one micron in thickness, were used as interlayers between the zirconia coating the substrate: aluminum (Al), silicon (Si), molybdenum (Mo), and titanium (Ti). Al was deposited anticipating that it would oxidize during heating to form alumina (Al_2O_3) and then react with the SiO_2 on the substrate to form mullite. Mullite is desirable because its thermal expansion lies between that of zirconia and Si_3N_4 or SiC.

Si was selected because its reactivity with other metals could improve the chemical bonding of the zirconia coating (which has excess zirconium on the bond interface).

Mo was deposited anticipating the formation of $MoSi_2$ which forms a very stable interface with carbides. Also, $MoSi_2$ has slow oxidation kinetics and, therefore may produce a stable interface with the ZrO_2 coating.

Ti was selected for several reasons. Titanium dioxide (TiO_2) forms a very stable interface with EB-PVD ZrO_2, titanium carbide (TiC) forms a very stable interface with carbides, and titanium nitride (TiN) forms a stable interface with nitrides. Also, Ti-silicides have a melting point higher than both constituents and have excellent oxidation resistance.

After pretreatment, the substrates were EB-PVD coated with 75 to 125 microns of zirconia stabilized with 20 percent yttria*. The coatings were applied at 980C. The initial few microns were deposited under oxygen deficient conditions (excess Zr) resulting in the thin, dense, equiaxed ZrO_2 coating desired for bonding. Oxygen was then introduced into the coating chamber resulting in a columnar microstructure with intercolumnar porosity, a structure which had an improved strain tolerance and compliance. The EB-PVD Y_2O_3 stabilized ZrO_2 microstructure is illustrated in Figure 2.

On visual inspection of the as-coated specimens, the EB-PVD coatings appeared adherent. A typical as-coated specimen is illustrated in Figure 3. The coatings varied in color, ranging from white to blue

---

*Coatings were applied at Temescal, Berkeley, California.

COLUMNAR ZrO2 →

DENSE ZrO2 →

RBSN SUBSTRATE →

96327-1

ZrO_2-20% Y_2O_3 ON RBSN

50μm
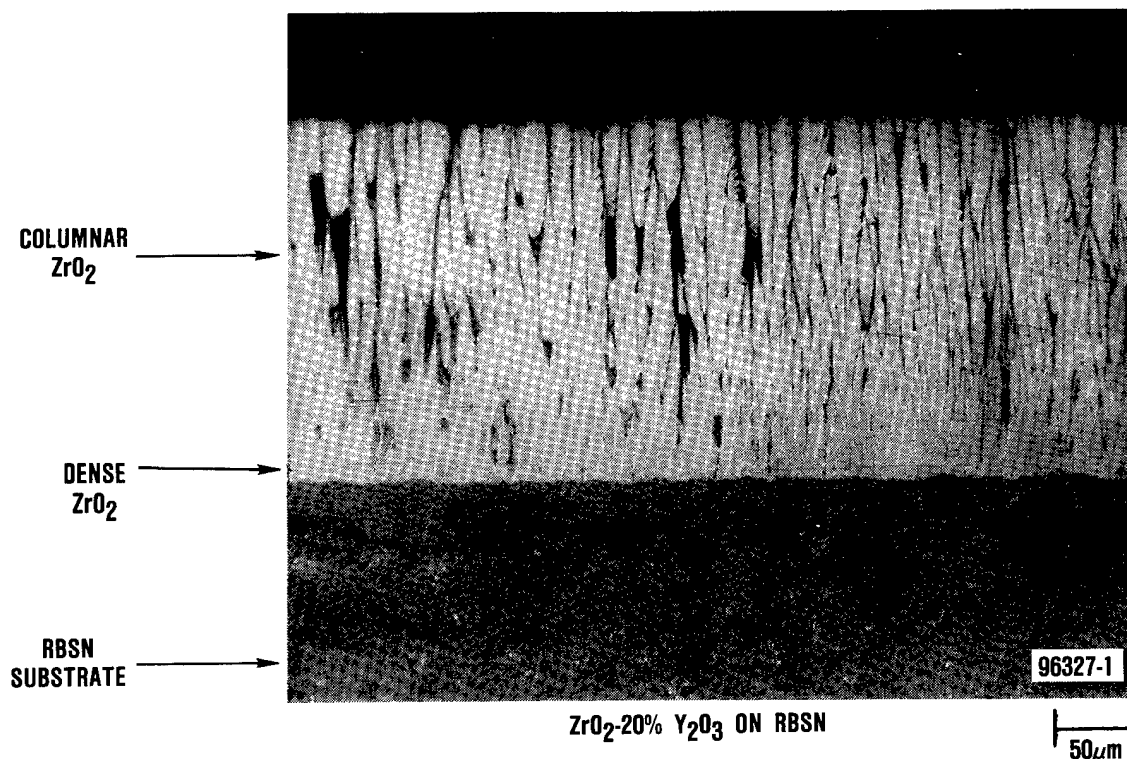
Figure 2. The EB-PVD zirconia coating grades from dense and microgranular at the interface to porous and columnar as it increases in thickness.

in Figure 3. The coatings varied in color, ranging from white to blue or gray. The color difference is typically associated with the stoichiometry of the ZrO_2 coating; white being stoichiometric and blue or gray being non-stoichiometric (oxygen deficient). In most cases the coatings were smooth and free of surface defects. Some specimens did exhibit small pits or bumps on the coatings which were attributed to "spitting" from the molten zirconia pool during coating. In some cases, the gray coatings were cracked or crazed. This effect could not be connected with any substrate, pretreatment or coating run.

Prior to evaluating adherence, some of the specimens received static air heat treatments at 1200C for 24 hours to evaluate the effect of oxidation exposures on the various coating/substrate systems. Visual inspection showed all coatings to be white regardless of their color prior to oxidation, indicating that all coatings were stoichiometric after oxidation exposure. For most systems, other than color change, little change in the appearance of the coatings was noted. The only significant change noted was that the ZrO_2 coatings on the Mo interlayer specimens cracked and spalled during heat treatment (Figure 4). Initially, it was felt that Mo was forming volatile oxides. Therefore, spare Mo interlayer specimens were heat treated in vacuum to eliminate oxidation effects. However, both the Mo and the
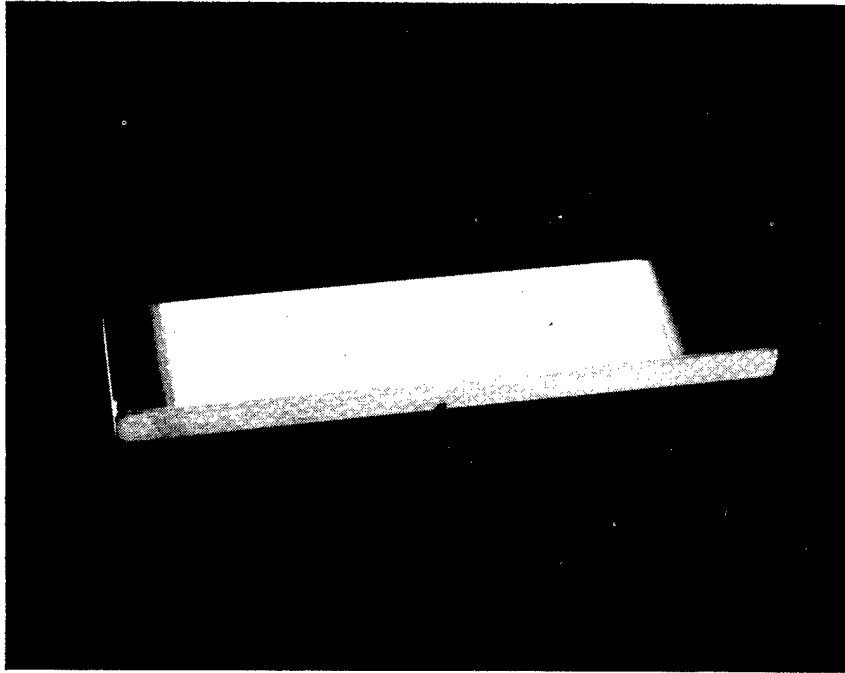
Figure 3. The EB-PVD zirconia appeared adherent to the substrates in the as-coated condition.

ZrO_2 spalled off together in sheets. Based on these results, the cause of spalling appears to be due to a thermal expansion mismatch or due to Mo reacting with the substrate and/or the coating. For all other coating/substrate systems, the ZrO_2 coating appeared clean and adherent after oxidation.

3.1.2 Adherence Testing

3.1.2.1 Adherence Assessment Procedures. The coating adherence was evaluated during Task 1 using three techniques: Scratch testing, flexure testing, and indentation testing.

Scratch testing was used primarily as a screening test. The test consists of sliding a moderately sharp implement across the coated surface. Visual observations were used to grade adherence. Coatings with poor adherence easily debond and flake off in sections. Moderately-adherent coatings require higher pressure to induce debonding, while adherent coatings show little or no debonding and only abrade.

Flexure testing was performed on as-coated specimens to examine the effects of mechanical shock on the various coating/substrate systems. Observation of the coating integrity in the contact area under the flexure load pins also was used to assess coating adherence. Flexure tests also provided preliminary evaluations of potential substrate degradation due to the coating process. Flexure tests were conducted such that the coated side of the specimen was in tension. An Instron Universal Testing Machine was used to load the specimen in four-point bending. The inner and outer spans of the test fixture
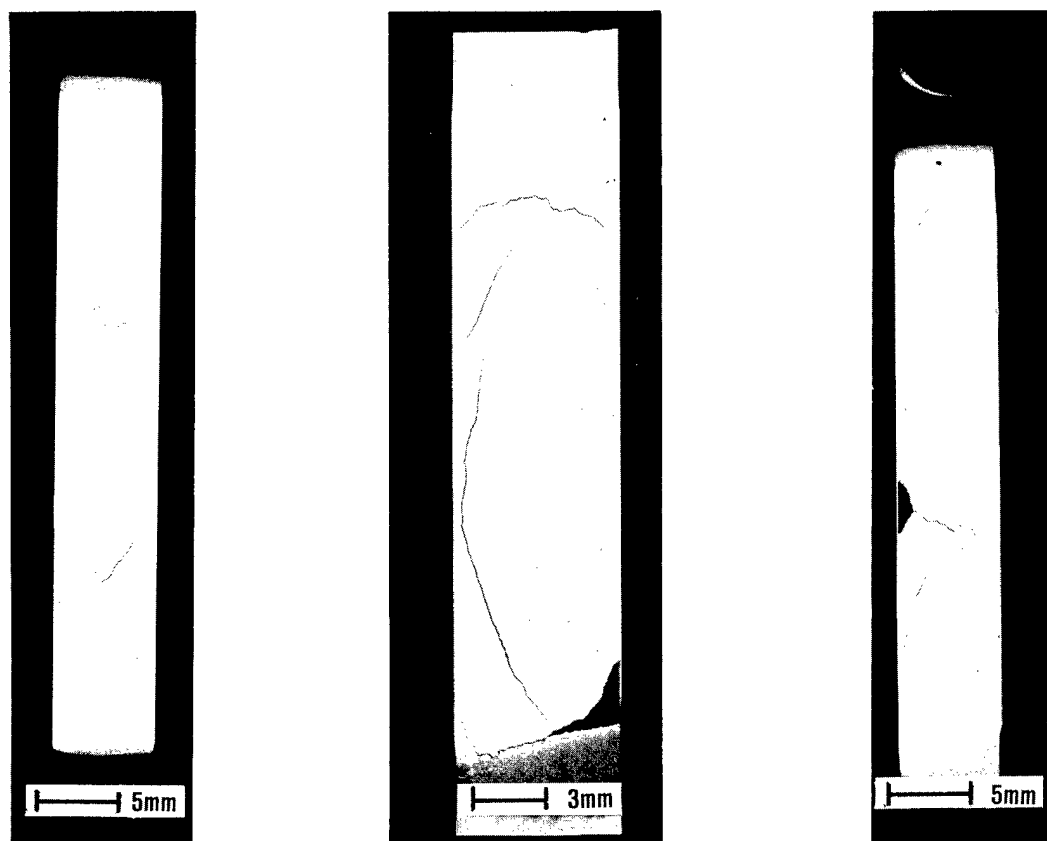
REACTION-BONDED Si$_3$N$_4$ SINTERED Si$_3$N$_4$ SINTERED SiC

Figure 4. Molybdenum interlayer specimens exhibited severe coating cracking during the ZrO$_2$ coatings on oxidation exposure.

were 12.7 and 25.4 mm, respectively. The Instron crosshead speed was 0.5 mm per minute. After testing, all fracture surfaces were examined up to 40X using an optical binocular microscope. Visual observations were used to assess coating adherence. A coating with "good" to "excellent" adherence will remain attached to all fractured pieces of the substrate. A weakly-bonded coating will usually spall adjacent to the fracture and under the flexure load pins. The strength of the specimen was considered in the adherence assessment since stronger specimens are subjected to higher loads and a more severe mechanical shock during testing.

Indentation testing* was also used to assess coating adherence. Testing consisted of applying a Vicker's indent normal to the coating. The Vicker's indenter is a sharp four-sided pyramid which produces

---

*Indentation tests were conducted at The University of California, Berkeley under the direction of Dr. A.G. Evans.

deformation in the coating and a wedging or buckling action at the coating/substrate interface. Four indentations were applied to each specimen at loads of 5, 10, 15, and 20 kg. The average radius of debond was used to assess coating adherence. The coating debond area was clearly visible and could be measured. Indentation is preferred to the methods described above since it is a more controllable test and gives quantitative information.

3.1.2.2 Adherence Test Results. In general, the adherence results from scratch, flexure, and indentation tests were in agreement. The trends observed are summarized below:

As-Coated Adherence

o   Relatively good adherence was observed for most coating/substrate systems.

o   RBSN substrates exhibited better coating adherence than SSN and SSC.

o   As-machined substrates yielded better adherence than lapped surfaces for SSN and SSC; no difference was observed for RBSN.

o   Oxidation and etching pretreatments had no significant effect on coating adherence.

o   All sputter-deposited interlayers tended to decrease coating adherence.

Adherence After Oxidation

o   The coating adherence for all coating/substrate systems was reduced significantly relative to the as-coated adherence.

o   RBSN substrates exhibited better coating adherence than SSN and SSC.

o   As-machined substrates yielded better adherence than lapped surfaces.

o   Pre-oxidation and etching pretreatments had no significant effect on coating adherence.

o   Sputter-deposited interlayers yielded poor coating adherence.

The results obtained using each of the adherence tests are discussed individually in the following paragraphs.

Scratch testing revealed a range of adherences for the various coating/substrate systems. As-coated RBSN, with pre-oxidation or etching pretreatments, exhibited the best adherence. Scratching with moderate pressure did not cause debonding and resulted only in minor abrasion of the coating surface. Heavy pressure was required to cause debonding. The degree of adherence appeared to be less for as-coated SSN and SSC with the same pretreatments, but could still be classified as good. All three substrate materials exhibited less adherence when a sputtered interlayer was applied. Coatings on sputter-coated substrates debonded with moderate pressure of the test implement. Scraping could then cause the locally-debonded coating to spall off. Substrates with machined finishes tended to yield better coating

adherence than lapped substrates. This trend appeared to be independent of the substrate or pretreatment.

After oxidation exposure at 1200C for 24 hours, the coating adherence was reduced in all cases. Although the adherence loss was significant for all coating/substrate systems, the general trends observed for as-coated systems still existed. RBSN exhibited better coating adherence than SSN and SSC substrates; machined surfaces yielded better adherence than lapped; and interlayer specimens yielded the poorest adherence. As reported in Section 3.1.1, the Mo interlayer specimens cracked and spalled on heat treatment. Specimens with pre-oxidation heat treatments generally appeared to have slightly better retained coating adherence. Heavily pre-oxidized RBSN exhibited the best overall adherence after oxidation exposure, although the level of adherence was much less than observed for the as-coated specimens.

Since oxidation exposure had a detrimental effect on coating adherence, studies involving heat treatments of 1200C for 100 hours and 1400C for 24 hours were conducted to obtain additional information. The adherence characteristics observed after 100 hours of exposure at 1200C were similar to those observed after 24 hours at the same temperature. RBSN still exhibited the best adherence; machined substrates gave better adherence than lapped; and interlayer specimens exhibited the poorest adherence. The results suggested that the interface may stabilize within the first 24 hours of heat treatment. After oxidation exposure at 1400C for 24 hours, a slight reduction in coating adherence relative to the 1200C exposures was observed. However, some differences in the adherence trends were noted. SSC systems now appeared to have better adherence than RBSN and SSN. Also, the adherence loss for Si interlayer specimens after the 1400C exposure was not as significant as seen after the 1200C exposures (though the adherence loss relative to the as-coated condition was still significant).

Flexure testing revealed the same general adherence trends as identified using scratch testing. RBSN substrates exhibited the best coating adherence regardless of surface preparation or pretreatment. In most cases, the as-coated ZrO_2 remained adhered to the RBSN substrates up to the fracture surface (Figure 5) with no debonding or spalling. In addition, the coatings adhered to SSN and SSC, however some debonding and chipping at the fracture surfaces did occur more frequently with the SSN material (Figure 6).

Machined surfaces exhibited better coating adherence than lapped surfaces. Coatings on lapped substrates frequently debonded under the flexure load pins.

The metallic interlayer pretreatments reduced coating adherence relative to the baseline (specimens with no pretreatment). The worst adherence was observed for metallic interlayers on specimens with lapped substrates. These specimens frequently exhibited spalling (Figure 7).

The strength results, summarized in Table 3, suggest that the pretreatment and coating.procedures do not significantly affect the
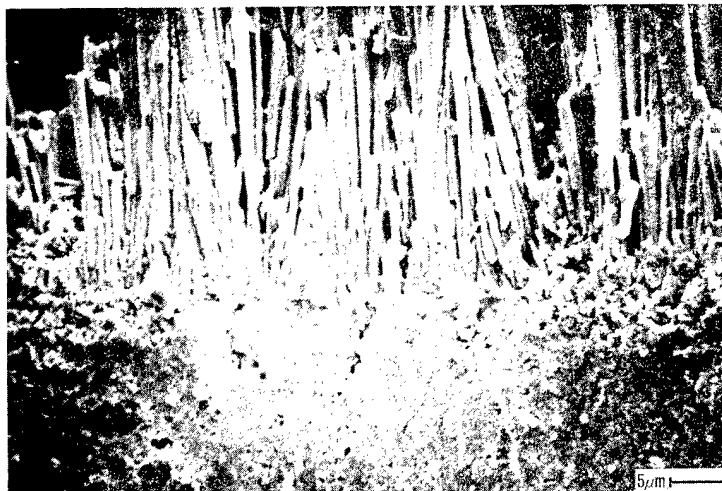
ZrO$_2$ COATING

AS-MACHINED RBSN
SUBSTRATE

5μm
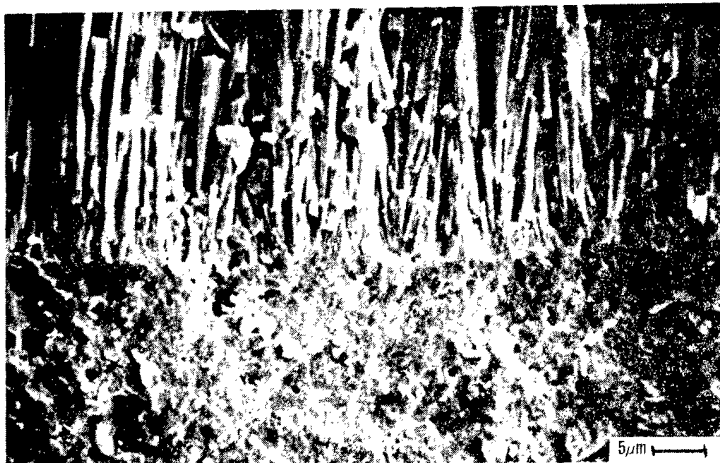
ZrO$_2$ COATING

HEAVILY-PREOXIDIZED
RBSN SUBSTRATE

5μm

ZrO$_2$ COATING

RBSN SUBSTRATE
WITH Si INTERLAYER

3μm

Figure 5.   As-coated zirconia remained adherent to RBSN substrates
with various pretreatments through flexure testing.

DEBONDED
AND CHIPPED →

20μm ⊢———⊣

ZrO₂ COATING ON AS-MACHINED SINTERED Si₃N₄

DEBONDED →

10μm ⊢———⊣

ZrO₂ COATING ON SINTERED Si₃N₄ WITH A Si INTERLAY
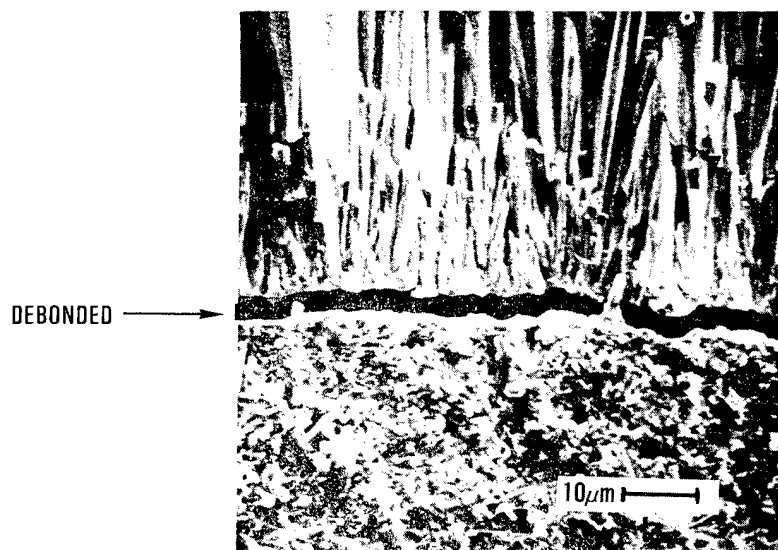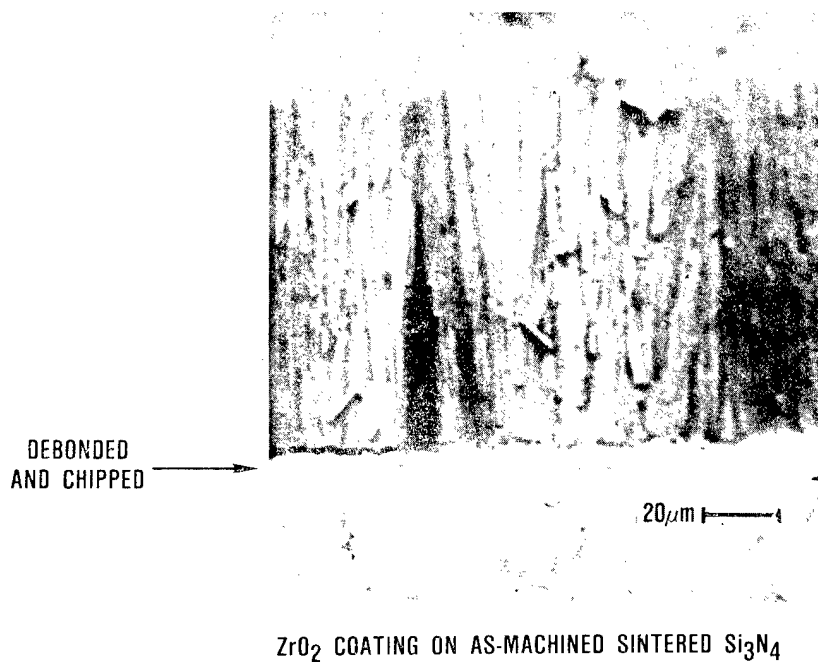
Figure 6.   In some instances, flexure testing resulted in debonding
      and/or chipping of zirconia coatings on sintered silicon
      nitride substrates.

| LAPPED RBSN WITH
Ti INTERLAYER | LAPPED SSN WITH
Ti INTERLAYER | LAPPED RBSN WITH
Mo INTERLAYER |
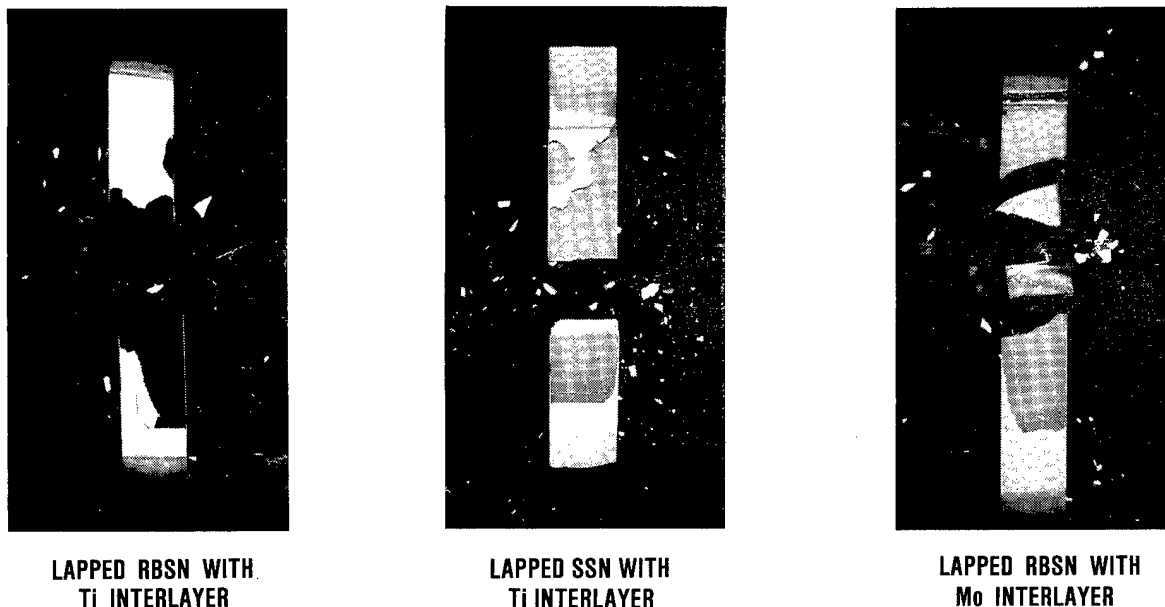
Figure 7.   The worst zirconia adherence was observed for lapped
substrates with metallic interlayers.

Table 3.   Comparison of the strength of coated test bars with
GTEC's baseline data on substrate strength.

Substrate	Average baseline strength MPa (ksi)	Average coated strength MPa (ksi)
RBSN	364.0 ±60.0 (52.8 ±8.7)	306.1 ±41.4 (44.4 ±6.0)
SSN	582.6 ±76.5 (84.5 ±11.1)	533.0 ±90.3 (77.3 ±13.1)
SSC	382.0 ±51.4 (55.4 ±7.3)	371.6 ±66.2 (53.9 ±9.6)

substrate strength.   The slightly reduced strengths of RBSN and SSN
were probably coincidental since the substrates for Task 1 were
selected from spare stock.

The indentation test results are summarized in Figure 8, where
the average radius of the debonded area is plotted as a function of
the indentation load.   The range of debonding observed is illustrated
in Figure 9.   The results are in agreement with those obtained by
scratch testing and flexure testing.   The best coating adherence was
observed for RBSN (both machined and lapped) with pre-oxidation or
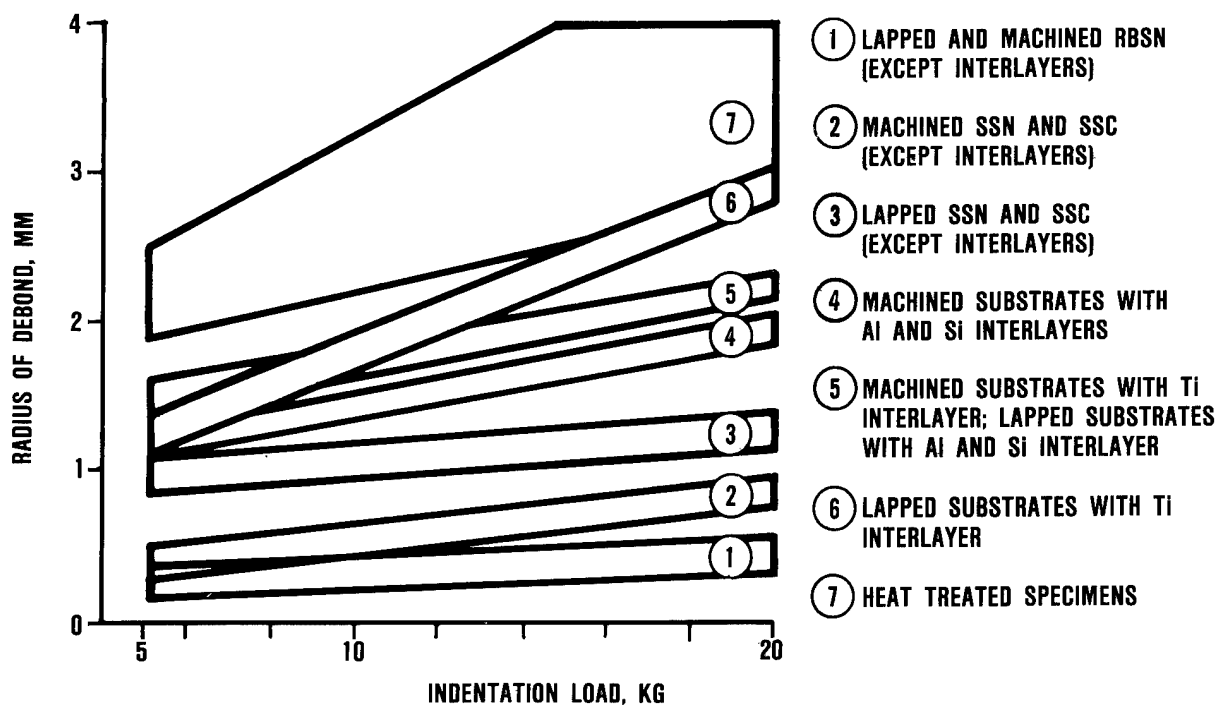
Figure 8.   Indentation results are summarized plotting the radius of
       debond versus indentation load.   The highest curve (#7)
       represent poorest observed, the lowest curve (#1) represents
       the best adherence.
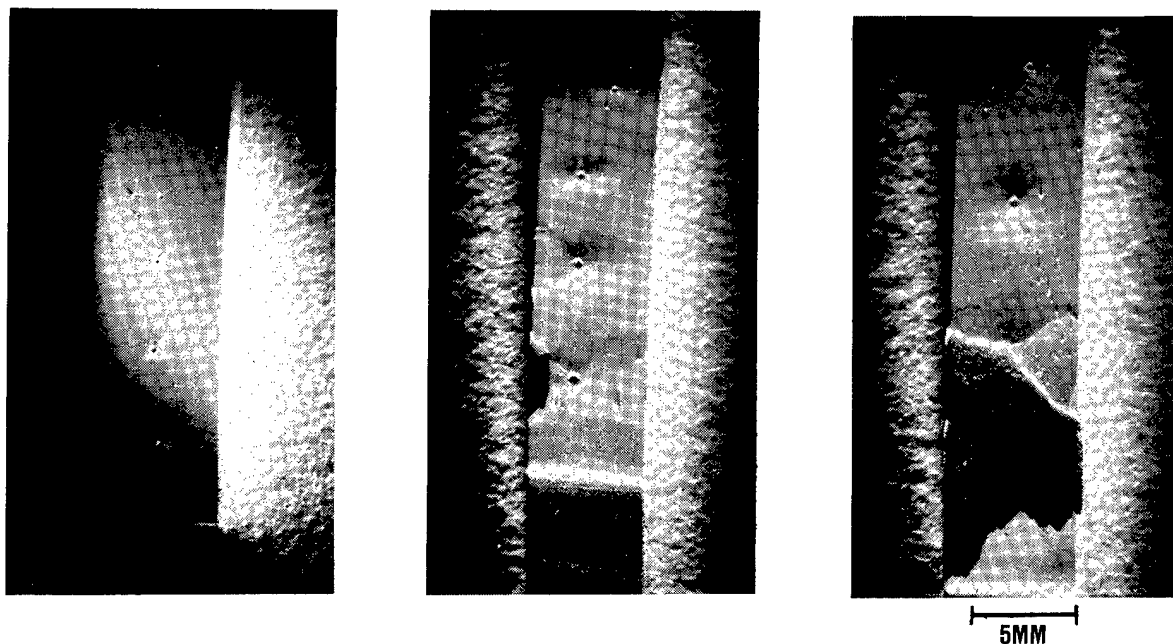
Figure 9.   Indentation testing provided the range of debonding
       observed above.

etching pretreatments. SSN and SSC as-machined substrates yielded slightly less adherence. Lapping the SSN and SSC substrates resulted in lesser adherence than for as-machined SSN and SSC. The sputtered metallic interlayers degraded as-coated adherence for all three substrate materials. Titanium yielded poorer coating adherence than aluminum or silicon. The ZrO_2 coatings adhered better to interlayers sputtered on as-machined substrates. After oxidation exposure at 1200C for 24 hours, all coated specimens, regardless of substrate or pretreatment, had poor coating adherence. In many cases, the heat-treated specimens exhibited debonding that extended to the edges of the specimen (Figure 10) so that the debond area could not be quantified accurately to be included in Figure 8. Therefore, the degree of adherence loss on oxidation exposure is greater than illustrated in Figure 8.

Indentation testing was effective in assessing the adherence of ZrO_2 coatings before heat treatment. However, this technique was not

5mm
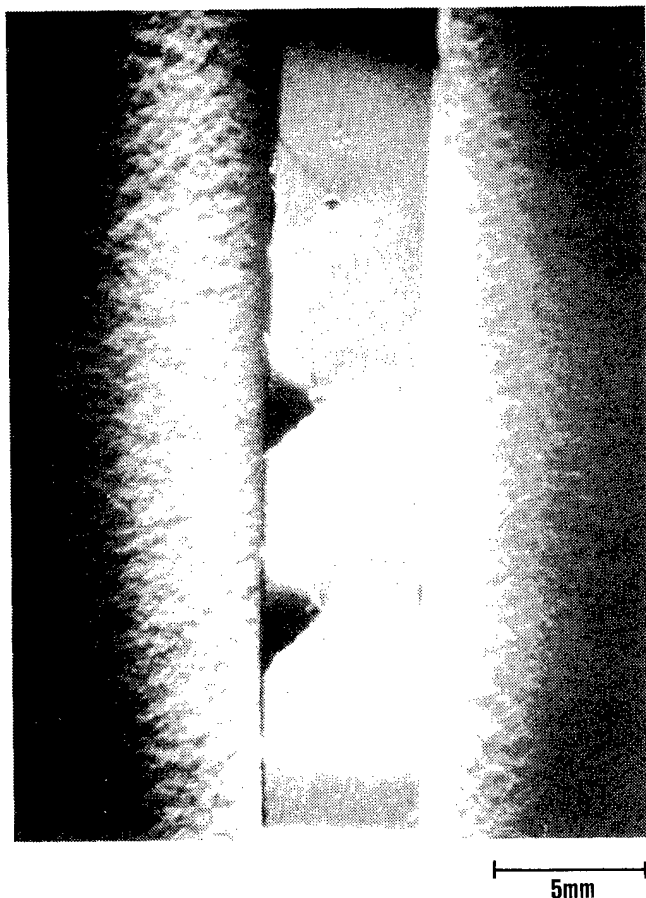
Figure 10. Many-heat treated specimens exhibited debonding that extended to the edges of the specimen and therefore did not provide comparative information.

as useful for quantitatively characterizing the weakly adherent coatings after heat treatment since extensive debonding and chipping occurred during testing. Evidently, the localized stress conditions imposed by the Vicker's indenter are too severe for evaluating the weaker coatings. In addition, they appear to be much more severe than likely to occur in a heat engine. A test using less severe stress conditions would compliment the indentation results in evaluating weaker coating/substrate systems. Also, conditions better simulating heat engine application conditions are desired for predicting the coating's performance in use.

3.1.3 Evaluation of Alternate Adherence Assessment Techniques

It was recognized in Task 1 that an alternate quantitative adherence assessment technique was needed for evaluating poorly adherent coating systems, as well as the adherent ones. Therefore, the development and evaluation of alternate methods of adherence assessment which better simulate application conditions was initiated. Tests considered were those which enabled the load distributing capabilities of the low-modulus EB-PVD coating to control the stresses present at the coating/substrate interfaces. Two techniques were evaluated: Blunt indentation testing and line contact* testing.

3.1.3.1 **Blunt Indentation Testing.** Blunt indentation testing involves procedures similar to those of Vicker's indentation testing but involves the use of a 3.175-mm-diameter sapphire ball indenter. The sharp Vicker's indenter severely deforms the coating and penetrates to the coating/substrate interface during testing. The ball indenter produces a less severe stress concentration, is closer to conditions likely to occur in a heat engine, and is less likely to cause the large degree of debonding observed with Vicker's indentation.
As expected, results from ball indentation suggested a less severe stress concentration. However, other than deformation of the coating from the ball indenter, no visual damage resulted, leaving no means for assessing the coating adherence (Figure 11). Modifying this technique to induce damage would involve the use of a smaller diameter ball. Because this modification was a step back toward Vicker's indentation, efforts in developing new indentation procedures were not continued.

3.1.3.2 **Line Contact Testing.** Line contact testing involved subjecting the coating to biaxial stress conditions by displacing a line contact load across the coating surface. Figure 12 illustrates the test rig used for contact testing. With this apparatus, a normal force is applied to the specimen through a dead-weight load system

---

*Line contact describes the contact geometry between a cylinder and a flat plate.
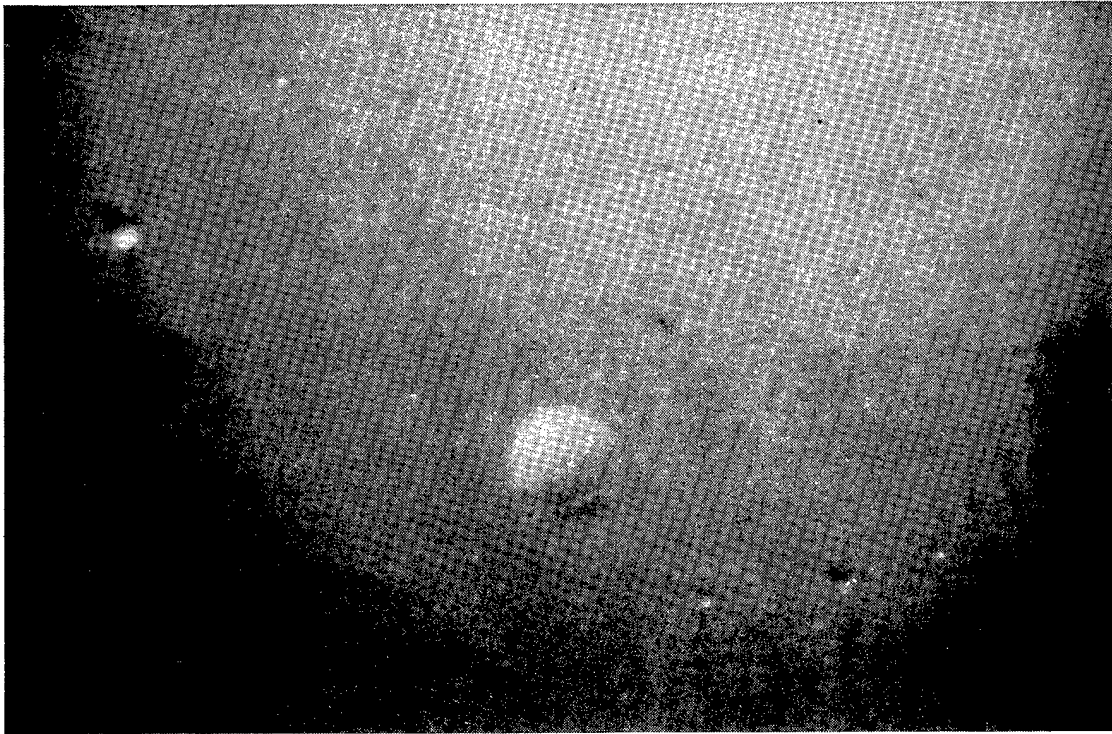
Figure 11. A 20 kg ball indentation provides no information for
       assessing coating adherence. No damage, other than deformation
       of the coating, occurred.

while a tangential force is applied through displacement of the
Instron crosshead. The tangential force is monitored by a load cell
located in the crosshead. This mode of loading was identified in
prior studies to be a critical condition to evaluate.[2] Contact test-
ing was originally planned for use in Task 3 of the program for
determining friction characteristics and the resistance to contact
damage. However, exploratory tests indicated that line contact test-
ing is also useful for coating adherence characterization.

     Contact tests were conducted in the static mode (i.e., normal and
tangential loads are applied but no sliding was initiated) and in the
sliding mode (i.e., normal and tangential loads are applied where the
tangential load was sufficient to cause sliding).

     Static tests were conducted using up to 27.2 kg normal load, with
tangential loads 20 percent of the normal (preliminary tests suggested
25 to 30 percent of the normal load is required to initiate sliding).
No significant damage to the coatings occurred under these test condi-
tions, as illustrated in Figure 13. In no case did the coating spall
or chip regardless of substrate material or pretreatment. A few
specimens exhibited debonding at the highest loads, but the debonding
was contained to the thin line of contact.

     Emphasis shifted to sliding contact tests since static tests did
not generate significant damage to the coatings. For sliding contact
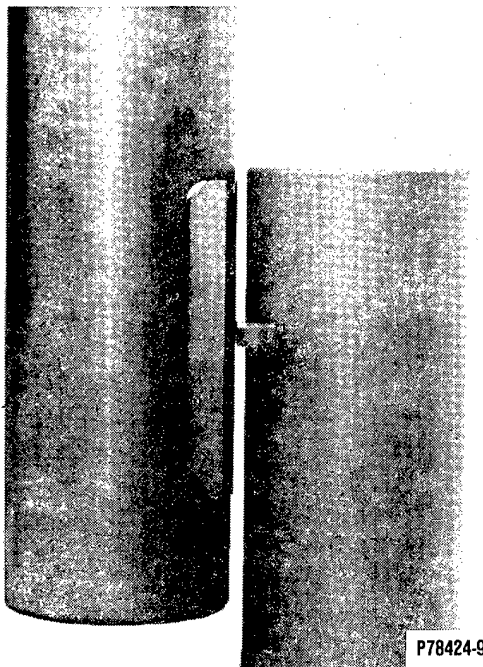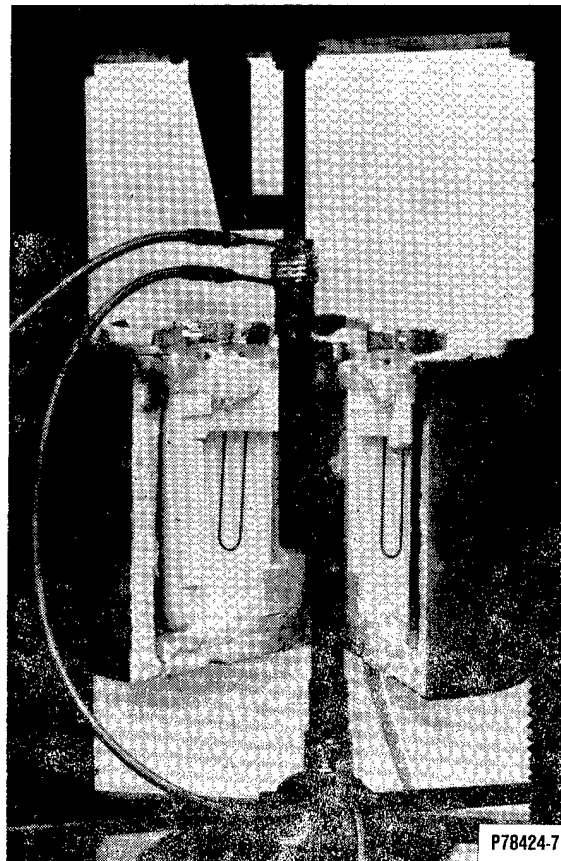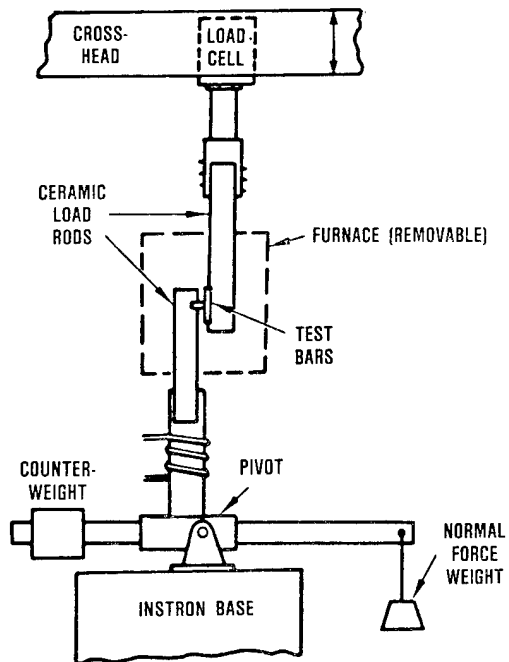
Figure 12.   The GTEC Contact Test Rig applies a normal load through a
      dead weight loading system while a tangential force is applied
      through displacement of the Instron crosshead.

LOAD

◄ 27.2 KG NORMAL
   5.4 KG TANGENTIAL

◄ 22.7 KG NORMAL
   4.5 KG TANGENTIAL

◄ 18.1 KG NORMAL
   3.6 KG TANGENTIAL

◄ 13.6 KG NORMAL
   2.7 KG TANGENTIAL

LOAD

◄ 27.2 KG NORMAL
   5.4 KG TANGENTIAL

◄ 22.7 KG NORMAL
   4.5 KG TANGENTIAL

◄ 18.1 KG NORMAL
   3.6 KG TANGENTIAL

◄ 13.6 KG NORMAL
   2.7 KG TANGENTIAL

MACHINED RBSN
Si INTERLAYER PRETREATMENT
POST-COATING OXIDATION

MACHINED RBSN
Al INTERLAYER PRETREATMENT
POST-COATING OXIDATION
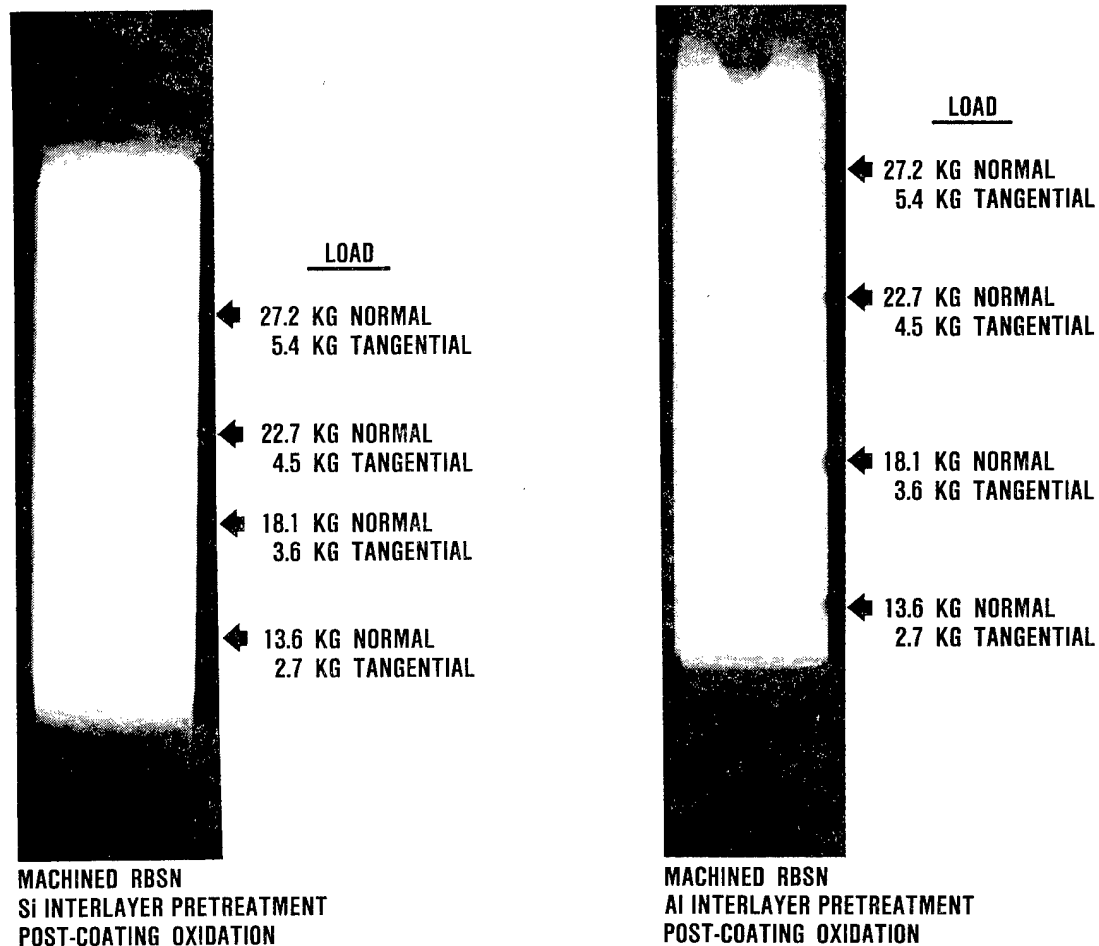
Figure 13. No significant damage to the coatings occurred during
         static line contact testing. The specimens shown above have
         relatively poor coating adherence based on results form
         scratch, flexure, and indentation tests.

tests, a normal contact load was displaced 1.52 mm. An 11.3-kg normal
load was used in this study. Results suggested this test can be used
for coating adherence evaluation. Figure 14 compares the effects of
static and sliding contact test conditions on coated specimens.   In
most cases, sliding tests using a 11.3 kg normal load could induce
damage, while static tests using a 27.2 kg normal load could not.
     From the contact test results, it was concluded that sliding line
contact should be used to complement the indentation test in future
adherence assessment tasks. The preliminary contact tests showed that
sliding line contact is an attractive technique for adherence assess-
ment since it is amenable to the poorly adherent coatings. Also, the
sliding contact test may better assess which systems would perform
best in a contact stress application since the test simulates contact
conditions at ceramic component interfaces.

24

STATIC TEST
27.2 KG NORMAL
5.4 TANGENTIAL

SLIDING TEST*
11.3 KG NORMAL
1.524 MM
DISPLACEMENT

STATIC TEST
27.2 KG NORMAL
5.4 TANGENTIAL

SLIDING TEST
11.3 KG NORMAL
1.524 MM
DISPLACEMENT

STATIC TEST
27.2 KG NORMAL
5.4 TANGENTIAL

SLIDING TEST*
11.3 KG NORMAL
1.524 MM
DISPLACEMENT

LAPPED RBSN
LIGHT OXIDATION
PRETREATMENT

LAPPED SSN
NO PRETREATMENT

MACHINED SSC
LIGHT OXIDATION
PRETREATMENT

NO DAMAGE ON STATIC
OR SLIDING TEST

NO DAMAGE ON STATIC TEST
DEBONDING ON SLIDING TEST

NO DAMAGE ON STATIC TEST
SPALLING ON SLIDING TEST

*DIRECTION OF CONTACT SLIDING MOTION

Figure 14. In most cases, sliding tests using 11.3 kg normal load could induce damage where static tests using 27.2 kg normal load did not.

3.1.4 Interface Analysis

Interface analyses* were performed to determine the nature of the coating adherence degradation observed on oxidized specimens. Since zirconia is permeable to oxygen, oxidation of the substrate was anticipated. Polished specimens were prepared so that coating/substrate interfaces could be examined using a high-resolution scanning electron microscope (SEM). Energy-dispersive X-ray (EDX) analysis was used to provide chemical information.

Four specimens were prepared for evaluation: ZrO_2/RBSN and ZrO_2/SSN both before and after oxidation exposure. The SEM results suggested that a silicate layer at the interface was responsible for the adherence loss. For as-coated ZrO_2/RBSN and ZrO_2/SSN, a thin layer was detected at the coating/substrate interface. It was suspected that this layer was a zirconium silicate since the major constituents detected by EDX were Si and Zr. The results suggest that ZrO_2 coatings adhere to the silicate since most as-coated specimens without sputtered interlayers exhibited relatively good adherence. This silicate layer probably formed during coating since oxidizing

*Interface analyses were conducted at The University of California, Berkeley, under the direction of Dr. A.G. Evans.

conditions existed (i.e., oxygen was bled into the coating chamber during deposition). The micrographs shown in Figure 15 indicate significant growth of the silicate layer during subsequent oxidation. For ZrO_2/RBSN, the silicate layer (not visible for the as-coated specimen) grew to approximately 1 micron in thickness during heat treatment. Some porosity appears to be present within the silicate but this may have resulted from pullout during polishing. The hypothesis for the adherence degradation observed is that the silicate layer after growth is cohesively weak. Similar effects were observed for the ZrO_2/SSN system; the silicate layer grew between 2 and 3 microns in thickness. The thicker silicate layer may be a result of the sintering additives present in SSN.

3.1.5 Task 1 Summary and Conclusions

The EB-PVD process produced controlled coatings of ZrO_2 20-percent Y_2O_3 with good to excellent adherence on machined surfaces of
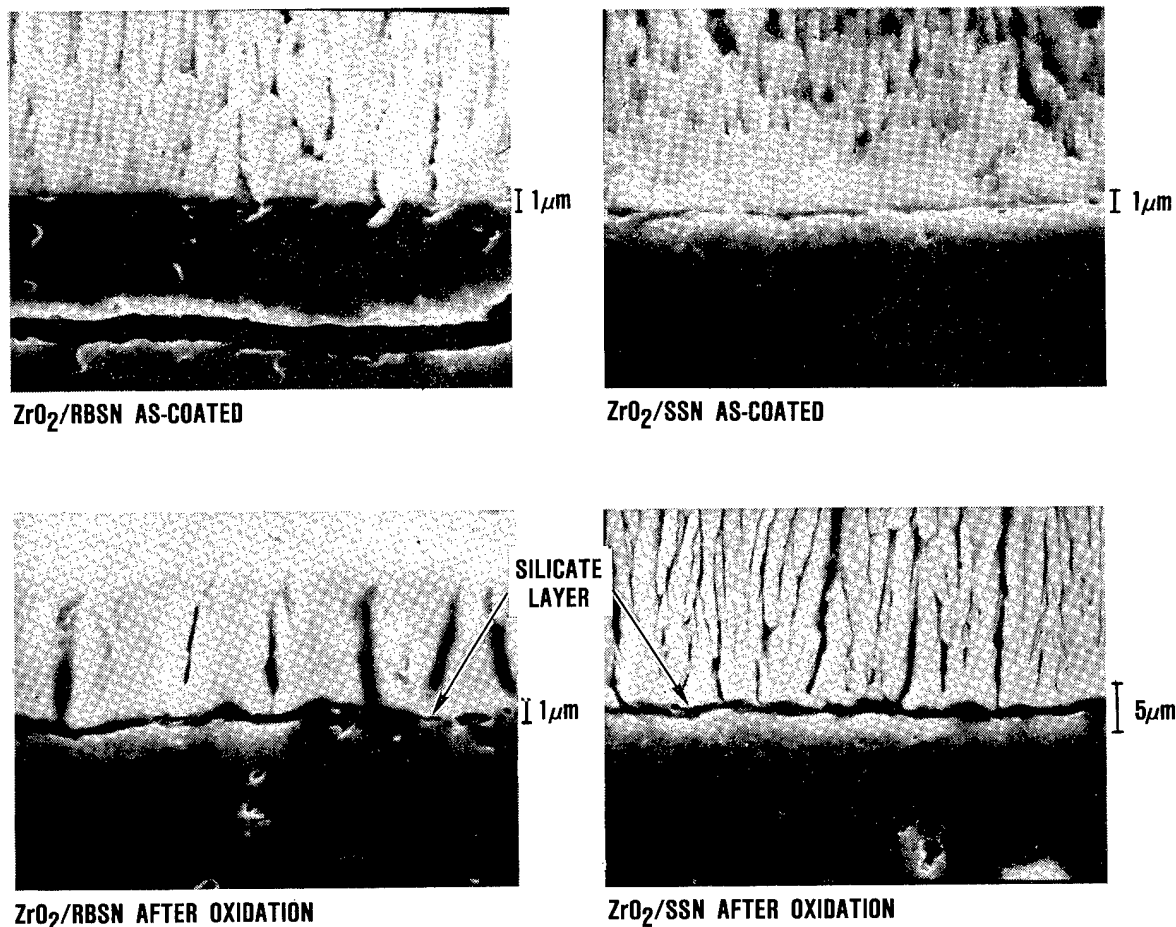
Figure 15. Oxide growth at the coating substrate interface takes place during oxidation exposure.

RBSN, SSN, and SSC. The coating procedures appeared not to have any detrimental effects on substrate strength. SEM and EDX results suggested that the bond interface between the ZrO_2 and as-machined substrate is a thin film of zirconium silicate.

Mechanical adherence contributed significantly to the overall adherence of EB-PVD ZrO_2. RBSN, which has the roughest surface of the substrate materials due to its 15-percent residual porosity, consistently exhibited better adherence than the dense SSN and SSC substrates. Also, lapping the 320-grit ground surfaces prior to coating resulted in poorer adherence in most cases.

Of the various oxidation, etching, and sputter coating pretreatments, none imparted any additional adherence to the as-coated specimens. The oxidation and the etching pretreatments did not have any significant effect on the as-coated adherence relative to baseline substrates. The sputtered interlayers (aluminum, silicon, molybdenum, and titanium) decreased the level of coating adherence relative to the baseline.

Static air oxidation exposures of coated specimens significantly degraded the coating adherence for all coating/substrate systems. The loss of adherence was attributed to the growth of the silicate layer at the coating substrate interface. Since ZrO_2 is known to be permeable to oxygen, it was anticipated that oxidation of the substrates would occur in cases where the ZrO_2 was deposited on bare Si_3N_4 or SiC substrates. Since the oxidation and sputtered interlayer pretreatments were unsuccessful in preventing adherence loss, it was concluded that approaches aimed at reducing or eliminating adherence loss due to oxidation should be emphasized in subsequent tasks.

Vicker's indentation was an effective technique for characterizing strongly adherent coatings. However, the interfacial stress conditions imposed by the Vicker's indenter were too severe for the weakly bonded coatings observed after oxidation. For oxidized specimens, extensive debonding and chipping occurred on testing. Therefore, alternate adherence assessment methods utilizing less severe stress conditions were screened during Task 1 for potential use in later adherence evaluations. Subsequently, test procedures for line contact testing were developed which are applicable to both poorly and well-bonded coatings. Using both contact and indentation testing was expected to be more appropriate for coating adherence assessment than using only indentation testing.

3.2 TASK 2 - ADVANCED PRETREATMENT AND COATING STUDIES

During Task 2, developmental coating and adherence assessments continued. Adherence evaluation was modified to include contact testing, and emphasis was placed on coating adherence after post-coating oxidation heat treatment. Based on Task 1 observations, directions for adherence improvements were defined for Task 2. Primary approaches were the use of an oxygen diffusion barrier at the coating/substrate interface to inhibit oxide growth and the use of surface

roughening techniques to improve the coating's mechanical bond. Based on Task 2 adherence assessment results, the best coating approaches evaluated were selected for assessment of contact damage resistance in Tasks 3 and 4.

3.2.1 Selection of Coating Approaches

The results of Task 1 provided two major conclusions concerning the direction for adherence improvements:

o   The growth of a silicate layer at the ZrO_2/substrate interface during oxidation exposure significantly degrades coating adherence.

o   Mechanical bonding to rougher surfaces contributes to coating adherence.

Therefore, Task 2 efforts were directed toward the development of oxygen diffusion barriers to inhibit interface oxidation, and toward surface preparations to improve the mechanical adherence of the coatings. In addition to these efforts, the use of high-purity interlayers, diffusion/gradation zones, higher coating temperatures, and mullite coatings were evaluated. These approaches are discussed in the following paragraphs.

3.2.1.1 **Oxygen Diffusion Barriers**. The objective of these efforts was to prevent substrate oxidation by depositing an oxygen diffusion barrier between the substrate and the coating. A secondary objective was to select an interlayer with good adherence to both the substrate and the coating. The candidate interlayers selected were CVD alumina, CVD aluminum nitride (AlN), EB-PVD alumina, EB-PVD mullite, and sol-gel alumina.

Three of the interlayers were alumina, each deposited by a different technique. Alumina is an attractive candidate due to its low oxygen permeability (10^{-14} g/cm/sec at 1200C).[3] Also, the results from a study involving EB-PVD ZrO_2 coatings on sapphire showed that EB-PVD ZrO_2 bonded well to Al_2O_3, and that adherence was retained through oxidation and cyclic thermal exposures.[4]

CVD aluminum nitride was selected since it may form a stable bond with the substrates (particularly RBSN and SSN) while providing oxidation resistance (the surface of the AlN should oxidize to form alumina and provide the oxygen diffusion characteristics described above).

EB-PVD mullite is an attractive interlayer since it combines low oxygen diffusion with a thermal expansion coefficient between that of ZrO_2 and Si_3N_4 or SiC.

3.2.1.2 **Surface Roughening**. Various techniques for roughening the substrate surface were explored since substrate surface topography influenced coating adherence during Task 1. Candidate techniques included 150-grit diamond grinding (compared with 320-grit), hydrofluoric acid (HF) etching, and laser-texturing. Diamond grinding the substrate surface with a 150-grit increased the depth of the machining grooves; HF etching removed surface silica from the substrate to

potentially exaggerate surface features; and laser-texturing produced a matrix of cavities on the substrate surface.

3.2.1.3 <u>High-Purity Interlayer</u>. The use of a high-purity CVD Si_3N_4 or SiC interlayer between the substrate and the EB-PVD ZrO_2 coating was also examined. This study was performed to assess the effect of sintering additives in the substrates on coating adherence and adherence degradation during oxidation.

3.2.1.4 <u>Diffusion/Gradation Zone</u>. Techniques for producing a gradation or interdiffusion zone between coating and substrate were explored in order to chemically root the zirconia coating to the substrate. Candidate techniques included ion implantation of aluminum or zirconium, and ion-mixing nitrogen with aluminum sputtered on substrate. Due to scheduling difficulties, only the latter was evaluated.

3.2.1.5 <u>Coating Temperature</u>. Studies on metal substrate coatings have determined that adherence can be improved by increasing coating temperature.[5] Prior plasma spray studies suggest a similar result for ceramic substrates.[6] Therefore the effect of coating at higher temperatures was evaluated.

3.2.1.6 <u>Mullite Coating</u>. Developmental runs were conducted to determine if a thick mullite coating could be deposited by EB-PVD and result in better adherence than ZrO_2. Mullite is a better oxygen barrier than zirconia and has a closer thermal expansion match to SiC and Si_3N_4 substrate materials.

3.2.2 Specimen Preparation and Inspection

The three substrate materials, RBSN, SSN, and SSC, were procured in the form of billets. The billets were machined into test bars measuring 6.35 by 3.23 by 50.8 mm having longitudinally ground surfaces. The substrate was then pretreated (if required) prior to EB-PVD coating.

3.2.2.1 <u>Oxygen Diffusion Barrier Studies</u>. Under Oxygen Diffusion Barriers studies, interlayer coatings were procured from several sources:

<u>CVD alumina</u> coatings* 2 to 2.5μm thick were applied at 920C. The microstructure consisted of nodular grains one to three microns in size (Figure 16). X-ray diffraction (XRD) of the as-coated specimens showed the coating to be a mixture of alpha and kappa phase Al_2O_3.

---

*Applied at Kennametal's Philip M. McKenna Laboratory, Greensburg, Pennsylvania.

CVD-Al$_2$O$_3$ ON RBSN

10 μM

CVD-Al$_2$O$_3$ ON SSN

10 μm
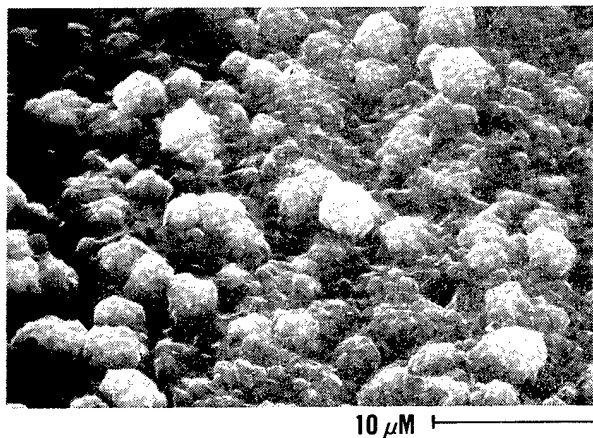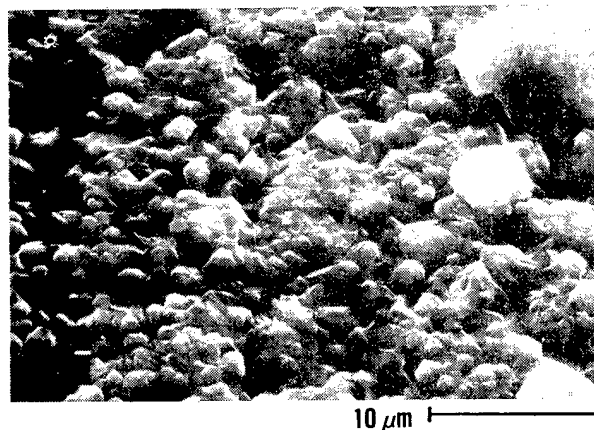
CVD-Al$_2$O$_3$ ON SSC
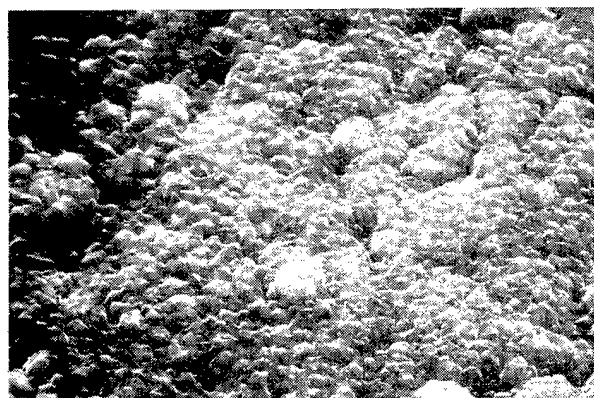
Figure 16. The microstructure of CVD alumina consists of nodular grains, one to three microns in size.

The specimens were heat treated in air at 1200C for 20 hours to convert the kappa-alumina to the alpha phase. XRD after heat treatment indicated complete conversion.

CVD aluminum nitride coatings* approximately 2 to 3μm thick were deposited using a fluidized bed technique.

EB-PVD alumina coatings** approximately 1μm in thickness were applied. The oxygen partial pressure in the coating chamber was varied to give two types of coating: stoichiometric Al_2O_3 and non-stoichiometric (Al-rich) Al_2O_3.

EB-PVD mullite coating** runs were conducted. However, mullite coatings could not be successfully applied by EB-PVD. The silica in the mullite material source evaporated more easily than the alumina resulting in silica rich coatings. Efforts to obtain a mullite oxygen diffusion barrier were not pursued further.

Sol-gel alumina coatings*** were developed and applied. The specimens were dipped in alumina sol, air dried, then calcined in air at 1200C. The resulting coating was approximately 0.5μm thick. During development efforts, thicker coatings were pursued, but usually cracked and/or spalled on drying or heating.

3.2.2.2 Surface Roughness Studies. Under Surface Roughness studies, all substrate treatments were conducted at GTEC.

Using 150-grit diamond grinding, approximately 50 microns was ground off one surface of each test bar.

HF Etching studies were conducted to roughen the substrate surface through etching of residual surface oxides. As-machined and oxidized (1200C for 24 hours in air) substrates were etched 10 minutes using a 10 percent HF solution. The resulting surface topographies were compared to un-etched, as-machined substrates. The resulting surface topographies suggested HF etching should not significantly enhance mechanical adherence (Figure 17). Therefore, the HF etching studies were not pursued further.

Laser-texturing was conducted using a 1.2 kw CO_2 laser. The laser was operated in a pulsed mode at 20 to 30 percent of the rated power to produce a matrix of surface cavities. Preliminary experiments indicated that 0.1mm diameter cavities 0.3mm deep resulted in a 20 percent loss for the substrates. Subsequently, the laser power was decreased 35 percent to reduce the cavity depth. The cavity depth obtained for SCC was reduced significantly (cavities were about 0.1mm deep). However, RBSN and SSN exhibited little change in cavity depth. Specimens from this laser run were subsequently coated with ZrO_2 for adherence evaluations.

---

*Applied at G.A. Technologies, San Diego, California.

**Applied at Temescal, Berkeley, California.

***Applied at Allied-Signal Engineered Materials Research Center, Des Plaines, Illinois.
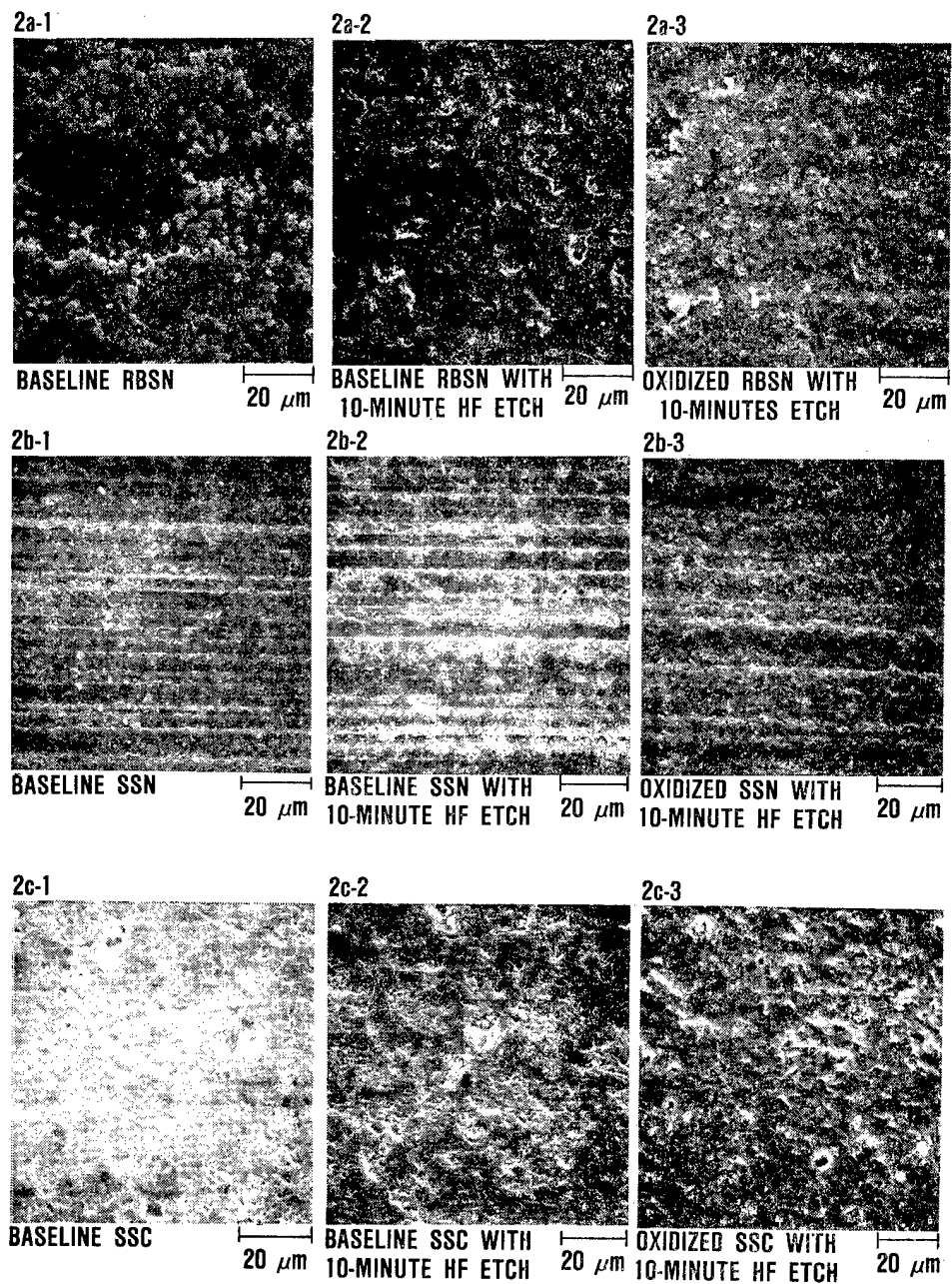
Figure 17. The surface topographies resulting from HF etching should not significantly enhance the mechanical adherence of the zirconia coating relative to baseline.

3.2.2.3 <u>High Purity Interlayer Studies</u>. In-house test bars of SSC have CVD SiC coatings* were used in preliminary evaluations. Efforts were not extended past preliminary investigations because of initial discouraging results (see Section 3.2.3.2).

3.2.2.4 <u>Diffusion Gradation Zone Studies</u>. A thin layer of aluminum was sputtered on each substrate then ion mixed with nitrogen ions**. Ion mixing was performed to drive aluminum atoms into the substrate for better bonding. Based on Task 1 results, aluminum was not expected to provide adequate bonding. Therefore, these specimens were heat treated 8 hours at 1200C in air in an effort to form an Al_2O_3 layer before subsequent EB-PVD coating.

3.2.2.5 <u>Coating Temperature and Mullite Coating Studies</u>. No pretreatment was required.

3.2.2.6 <u>EB-PVD Coating</u>. All specimens, except those under Coating Temperature and Mullite Coating Studies, were coated with EB-PVD zirconia using the procedures described in Section 3.1.1. For Coating Temperature Studies, the coating chamber was maintained at 1040C (the maximum temperature attainable by the equipment used) rather than 980C. Under Mullite Coating Studies, EB-PVD coating procedures for depositing zirconia were used. However, EB-PVD mullite could not be applied successfully to the substrates. The material source contained 80 weight percent alumina and 20 weight percent silica. Dense, non-columnar, silica rich films resulted from coating runs conducted at temperatures ranging from 700C to 1010C (Figure 18). The SiO_2 rich films probably resulted from the tendency of SiO_2 to evaporate more easily than the Al_2O_3. Efforts involving EB-PVD mullite coatings, as well as EB-PVD mullite oxygen diffusion barriers, were terminated.

The color of the as-deposited ZrO_2 coatings were either white or blue (no gray coatings, which were seen occasionally in Task 1, resulted). All coatings appeared as clean and adherent as those deposited during Task 1. Some of the coated specimens from each coating/substrate variation were heat treated 100 hours at 1200C to stabilize the interface prior to adherence investigations. Additional heat treatments at 1200C and 1400C for 24 hours were conducted under Coating Temperature Studies to compare with oxidation results from Task 1.

3.2.3 <u>Adherence Testing</u>

3.2.3.1 <u>Adherence Assessment Procedures</u>. Three techniques were utilized for coating adherence evaluations in Task 2: flexure testing, indentation testing, and line contact testing.

---

*CVD SiC coatings were applied at San Fernando Laboratories, Pacoima, California.

*Aluminum sputtering and ion mixing was performed at Oak Ridge National Laboratories (ORNL), Oak Ridge, Tennessee.

SILICA RICH COATING

87606 25KV 0.5U

87404 25KV 0.5U

RBSN SUBSTRATE   AI MAP   SI MAP
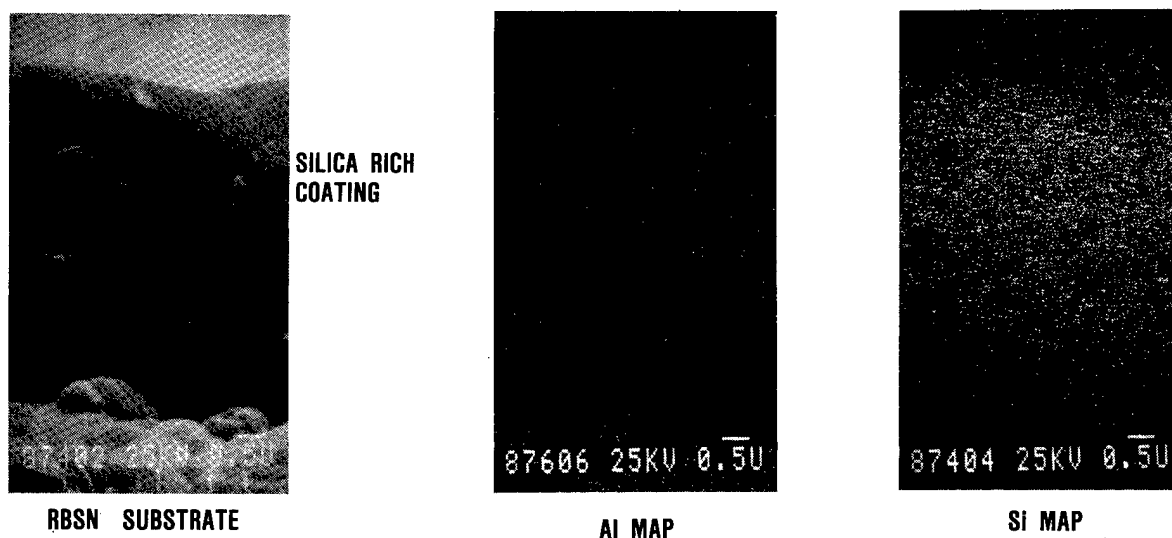
Figure 18. EB-PVD coating runs using 80 weight percent Al_2O_3 and
20 weight percent SiO_2 as a material source resulted in thin,
dense, non-columnar, silica rich films.

Flexure testing was conducted on as-coated specimens using the
procedures described in Section 3.1.2.1 for Task 1 adherence assess-
ment except that test fixture inner and outer spans of 19.05 and 38.1
mm,rather than 12.7 and 25.4 mm, were used since longer test bars were
available.

Indentation testing was conducted on both as-coated and heat-
treated specimens using the Task 1 procedures described in Section
3.1.2.1, except that loads of 5, 10, 20, and 30 kg were used instead
of 5, 10, 15, and 20 kg. Extending the test range to higher loads was
expected to provide a better assessment of more adherent coatings. It
was anticipated that very adherent coatings would exhibit little mea-
surable debonding when tested at the lower loads.

Line contact testing was used to evaluate the adherence of coated
specimens having post-coating heat treatments. The contact rig was
used for this testing and its operation is described in Section
3.1.3.1. Four tests were conducted per specimen with loads of 9.1,
13.6, 18.1, and 22.7 kg. The crosshead displacement was 1.52 mm. The
threshold normal load required for debonding, determined through
visual observations, was used to assess coating adherence. Typical
specimens from line contact testing are illustrated in Figure 19.

3.2.3.2 Adherence Test Results.

Oxygen Diffusion Barriers. CVD Al_2O_3 and CVD AlN interlayers
yielded the best adherence for RBSN. All other interlayers resulted
in lesser adherence. The best adherence characteristics for SSN and
SSC involved sol-gel alumina interlayers, although the level of
adherence was much less than that observed for the ZrO_2/CVD Al_2O_3/RBSN
and ZrO_2/CVD AlN/RBSN systems. Other interlayers resulted in less ad-
herence.

9.1 KG   13.6 KG   18.2 KG   22.7 KG

EXCELLENT ADHERENCE

9.1 KG   13.6 KG   18.2 KG   22.7 KG

FAIR ADHERENCE

9.1 KG   13.6 KG   18.2 KG   22.7 KG
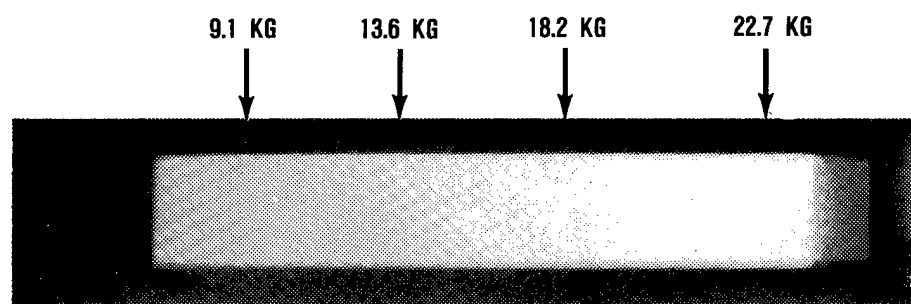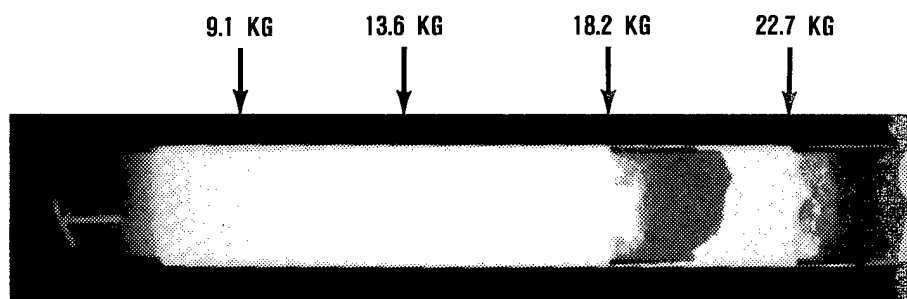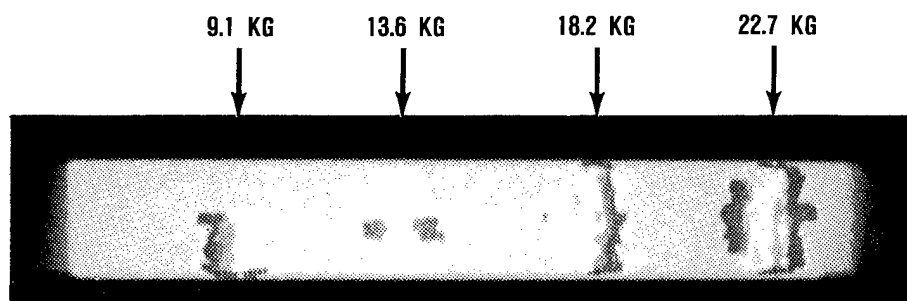
POOR ADHERENCE

Figure 19. After line contact testing, coating adherence is assessed using visual observations.

CVD alumina interlayer specimens were evaluated using indentation and line contact testing. The indentation results are shown in Figure 20. The RBSN specimens exhibited excellent adherence before and after oxidation exposures of 100 hours at 1200C. However, the CVD Al_2O_3 interlayers did not improve the coating adherence for SSN and SSC (EB-PVD ZrO_2 on as-machined substrates). SSN and SSC exhibited good adherence in the as-coated condition, but poor adherence after oxidation exposure. The line contact test results for CVD alumina interlayer specimens with post-coating oxidation exposures are shown in Figure 21. Excellent adherence was observed for RBSN; up to 22.7 kg normal load was used with no evidence of coating separation (12.7 kg tangential load). Fair adherence was observed for SSN; the coating spalled during the 18.1 kg test. Poor adherence was observed for SSC which debonded at 13.6 kg. These results suggest CVD alumina does inhibit degradation of the interface during oxidation exposure for RBSN. However, the CVD alumina does not appear to benefit SSN or SSC. The hypothesis for this difference is that thermal expansion mismatches between the substrate and the coating resulted in interfacial cracking. Due to the residual surface porosity of RBSN, islands of interlayer remained adherent due to rooting into the substrate pores.

CVD aluminum nitride interlayer systems were evaluated using flexure, indentation and line contact testing. Flexure testing was only conducted on as-coated specimens. Debonding and/or spalling occurred under the load pins for all tests suggesting poor coating
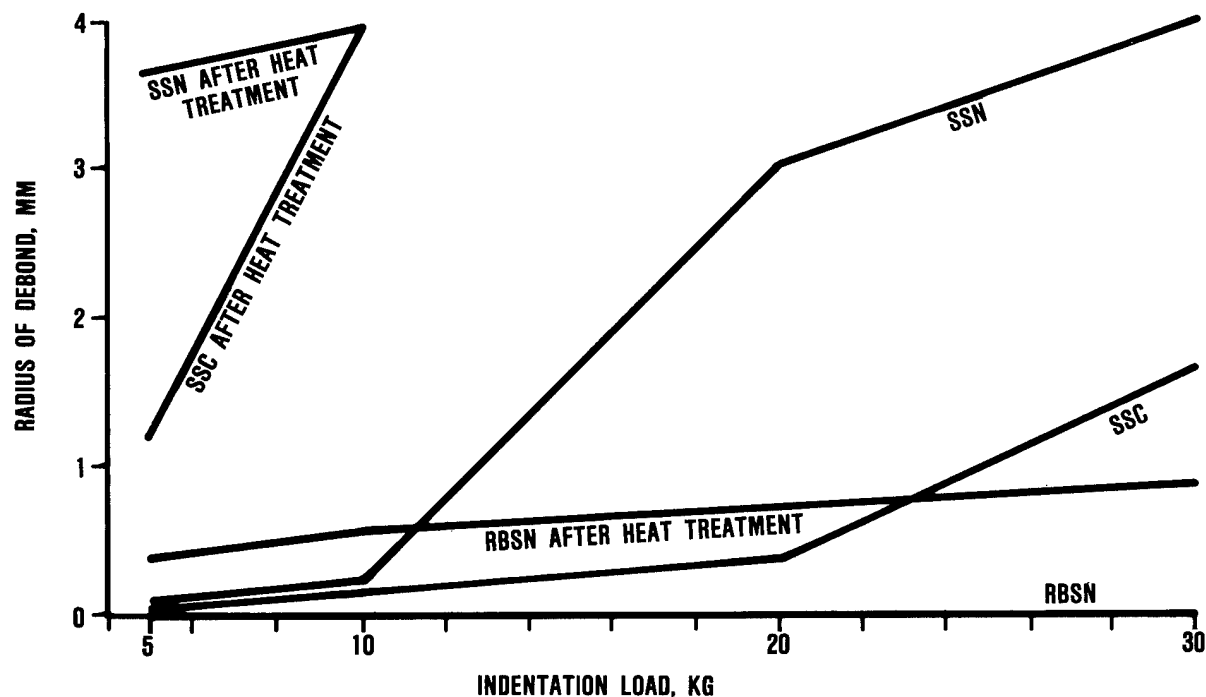
Figure 20. RBSN specimens with CVD Al_2O_3 interlayers exhibited excellent adherence before and after oxidation heat treatment.
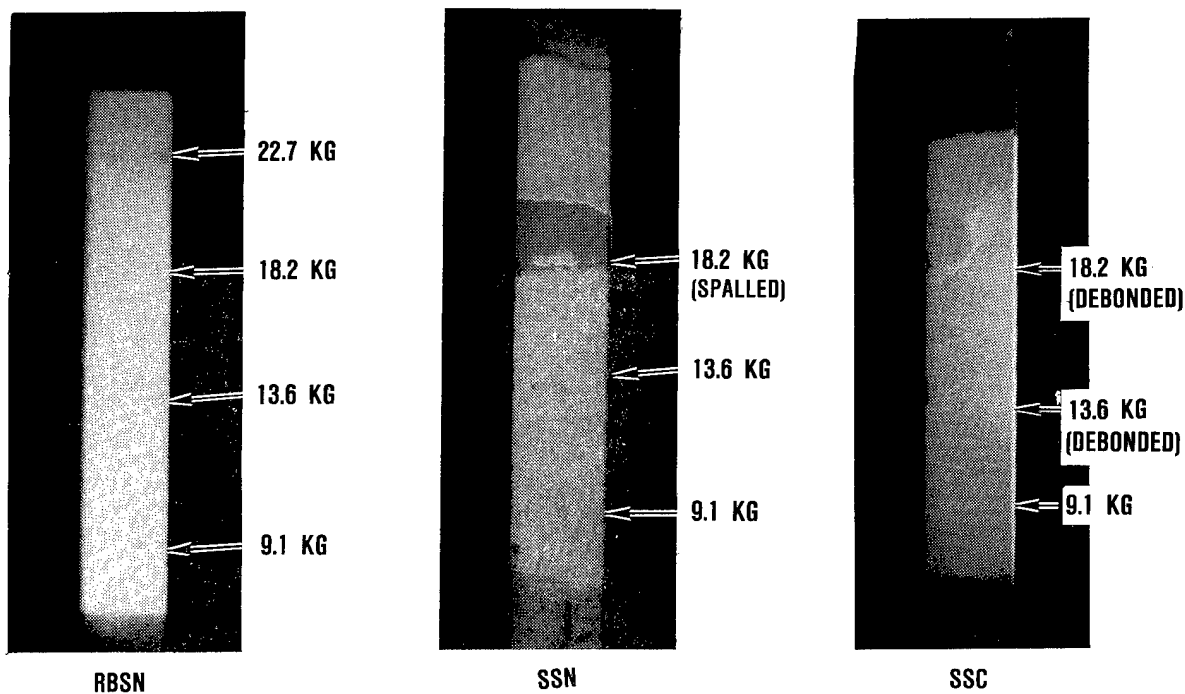
Figure 21. Contact testing results of oxidized CVD alumina
interlayer specimens show excellent adherence for RBSN,
fair adherence for SSN, and poor adherence for SSC.

adherence for all three substrate materials. EDX analysis of spalled
surfaces suggested that the zirconia spalled from the AlN interlayer
since a strong aluminum peak, and no silicon peak, was detected.
Indentation tests were conducted on both as-coated and oxidized speci-
mens. The results are shown in Figure 22. The as-coated ZrO_2
adherence was poor for all three materials, which agreed with the
flexure test results. However, the adherence improved significantly
after oxidation exposure for RBSN and slightly for SSN and SSC. RBSN
exhibited excellent adherence after oxidation. Fair adherence was
observed for SSN and SSC. The better adherence observed for RBSN may
have resulted from the CVD coating rooting into RBSN's residual
porosity. Line contact testing was used to evaluate the adherence of
oxidation exposed SSN and SSC specimens. Poor and fair adherence was
exhibited by SSN (spalled at 9.1 kg normal load) and SSC (debonded at
13.6 kg, no spalling up to 22.7 kg) respectively. The ZrO_2/CVD AlN/
RBSN specimens were oversize and could not be accommodated by the con-
tact rig. Therefore, a specimen was evaluated by scratch testing us-
ing the procedures described in Section 3.1.2.1. The adherence
observed was excellent as the coating could not be dislodged from the
substrate. The coating would only abrade when scratched under heavy
pressure. The increased adherence of the zirconia coating after oxi-
dation exposure suggests chemical interaction between the ziconia
coating and AlN interlayer. Optical, SEM and EDX analysis of the
interface, before and after oxidation, was performed to determine the
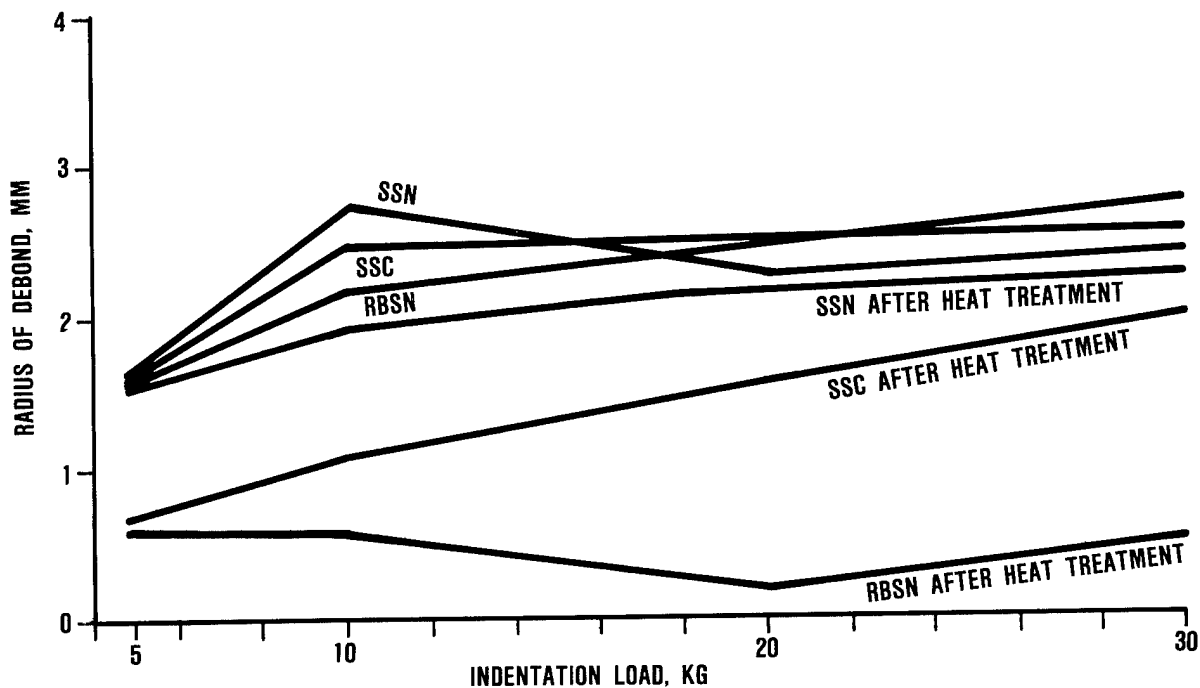
Figure 22. The adherence for ZrO_2/CVD AlN/RBSN increased
significantly after heat treatment.

nature of the adherence improvement. The optical and SEM results sug-
gest a change in interfacial characteristics (Figure 23). However,
EDX analysis did not suggest any diffusion took place during oxidation
exposure. Evidently, the CVD AlN oxidized to form Al_2O_3 which
resulted in the excellent post-oxidation adherence characteristics.

EB-PVD Al_2O_3 interlayer specimens (stoichiometric and non-
stoichiometric) were tested for adherence using flexure, indentation,
and line contact tests. For flexure tests, extensive chipping and/or
debonding was observed for non-stoichiometric Al_2O_3 interlayer speci-
mens (Figure 24). EDX analysis suggests that the non-stoichiometric
Al_2O_3 interlayers were contaminated prior to EB-PVD ZrO_2 coating since
sodium (Na) and potassium (K) were detected on the still-adhered
EB-PVD Al_2O_3 interlayer (Figure 25). A lesser degree of chipping and
debonding was observed for SSN and SSC with stoichiometric Al_2O_3
interlayers. RBSN with a stoichiometric Al_2O_3 interlayer was not
damaged during flexure testing. EDX analysis of spalled areas on SSN
specimens suggested that EB-PVD Al_2O_3 adhered poorly to SSN since pri-
marily Si (from the substrate) was detected. The indentation results
are shown in Figures 26 and 27. The ZrO_2 coating adherence was poor
for both Al_2O_3 interlayers, but the stoichiometric Al_2O_3 was slightly
better. Contact testing conducted on oxidation-exposed specimens
showed poor adherence for the non-stoichiometric interlayers but fair
adherence for stoichiometric Al_2O_3. However, the tangential loads
generated were lower than typical, resulting in a less severe stress
condition.

OPTICAL

SEM

← PVD ZrO$_2$

← CVD AIN

← RBSN

AS-COATED ⊢————⊣ 10μm

AS-COATED ⊢—⊣ 1μm

HEAT TREATED ⊢————⊣ 10 μM

HEAT TREATED ⊢—⊣ 1μm
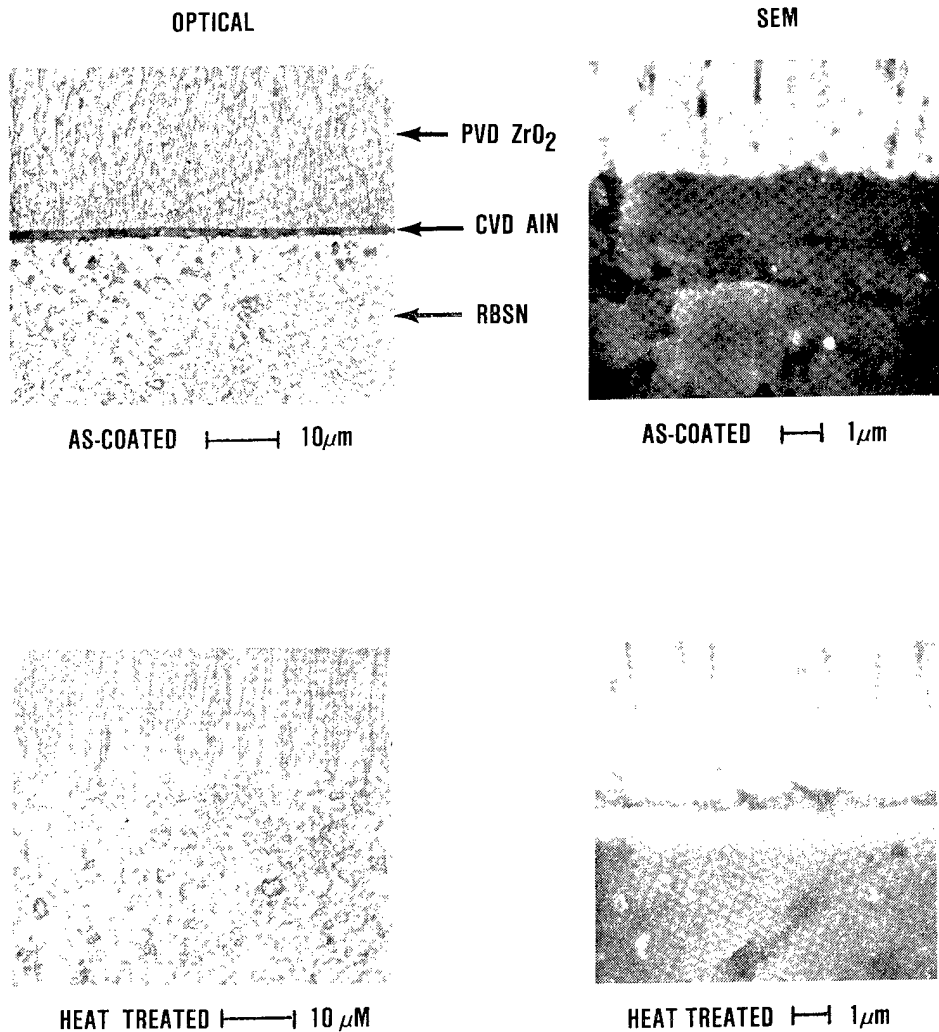
Figure 23. Optical and SEM analysis of the ZrO$_2$/CVD AlN/RBSN interface before and after oxidation exposure suggests a change in interfacial characteristics.

Sol-gel Al$_2$O$_3$ interlayer specimens were evaluated using flexure, indentation, and line contact testing, with varying results. Flexure test results suggested good adherence for RBSN and SSN (no spalling or debonding) and fair adherence for SSC (debonding under the flexure load pins). SEM micrographs of the fracture surfaces (Figure 28) show intimate contact at the interfaces for all three systems. In indentation tests with as-coated specimens, RBSN exhibited excellent adherence, while SSN and SSC exhibited fair adherence (Figure 29). After oxidation exposure, SSN and SSC exhibited no significant change in adherence characteristics, suggesting that the sol-gel Al$_2$O$_3$ prevented degradation. The ZrO$_2$/sol-gel Al$_2$O$_3$/RBSN coating adherence degraded significantly after oxidation. The retention in adherence observed for SSN and SSC was not expected since CVD Al$_2$O$_3$ did not provide adherence retention for these two substrates. Speculation is

EB-PVD ZrO$_2$

EB-PVD Al$_2$O$_3$
(NON-STOICHIOMETRIC)

SUBSTRATE
(RBSN)
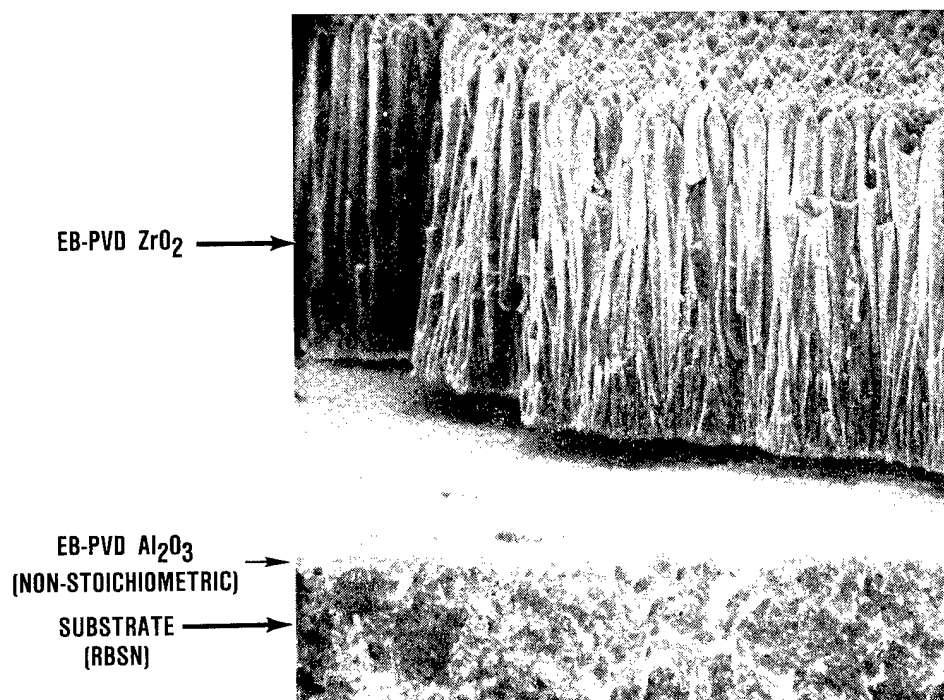
Figure 24. Zirconia coatings typically spalled from the
non-stoichiometric EB-PVD alumina interlayers during
flexure testing.

that the 50 percent porosity in the sol-gel interlayer (50A porosity)
provides improved strain tolerance to limit interfacial cracking
caused by thermal expansion mismatches. However, improved strain
tolerance is provided at the cost of the interlayer's cohesive
strength. Line contact testing on oxidized specimens suggested good
adherence for all three substrates, which contradicts the above
results. However, the tangential loads generated by friction were
lower than typically observed and resulted in a less severe stress
condition than used on other systems.

Surface Roughening. The results from surface roughening studies
suggested that 150-grit diamond grinding has no significant effect on
ZrO$_2$ coating adherence relative to 320-grit, and that laser texturing
can significantly increase both the as-coated and oxidized adherence.
The 150-grit machined substrates were indentation and line con-
tact tested for ZrO$_2$ coating adherence. Indentation results are shown
in Figure 30. The as-coated adherence was good to excellent. After
oxidation exposure, the adherence for RBSN, SSN, and SSC was poor.
Contact tests were performed on oxidized specimens. RBSN and SSN
exhibited fair adherence (spalled at 40 pounds) and SSC exhibited poor
adherence (spalled at 30 pounds). The results suggest that 150-grit
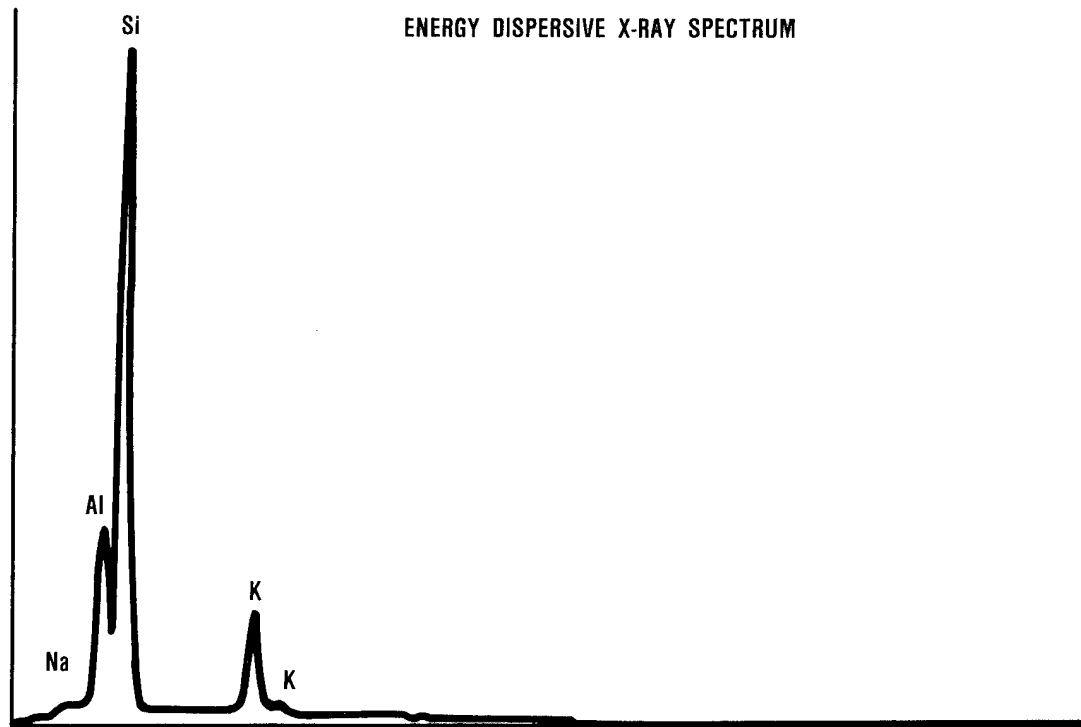
Figure 25. EDX analysis of spalled area suggests the
        non-stoichiometric alumina coatings were contaminated
        prior to EB-PVD zirconia application since sodium (Na)
        and potassium (K) were detected.

machining does not have beneficial effects on coating adherence relat-
ive to 320-grit machining.

Laser-textured specimens were evaluated for coating adherence
using indentation and line contact testing. Indentation tests were
conducted on as-coated and heat-treated specimens. The results show
excellent ZrO_2 adherence before and after oxidation (Figure 31). Line
contact tests were performed on heat treated specimens. The results
(Figure 32) did not completely agree with indentation test results.
The results only agreed for SSC, which exhibited very good adherence
(minor spalling at 22.7 kg). RBSN and SSN exhibited poor adherence
(spalled at 13.6 and 9.1 kg, respectively). The differences observed
in adherence were attributed to differences in the surface topography
of the substrates and not to substrate material. RBSN and SSN had
very deep surface cavities; analysis of spalled areas showed that
these deep cavities were not successfully filled in with by the zir-
conia and that only the walls of the cavities were coated (Figure 33).
SSC had much shallower cavities that were successfully filled with
ZrO_2 (Figure 34). The results for SSC were very encouraging because
good adherence after oxidation exposure was achieved without the use
of an oxygen diffusion barrier to prevent oxidation of the substrate.
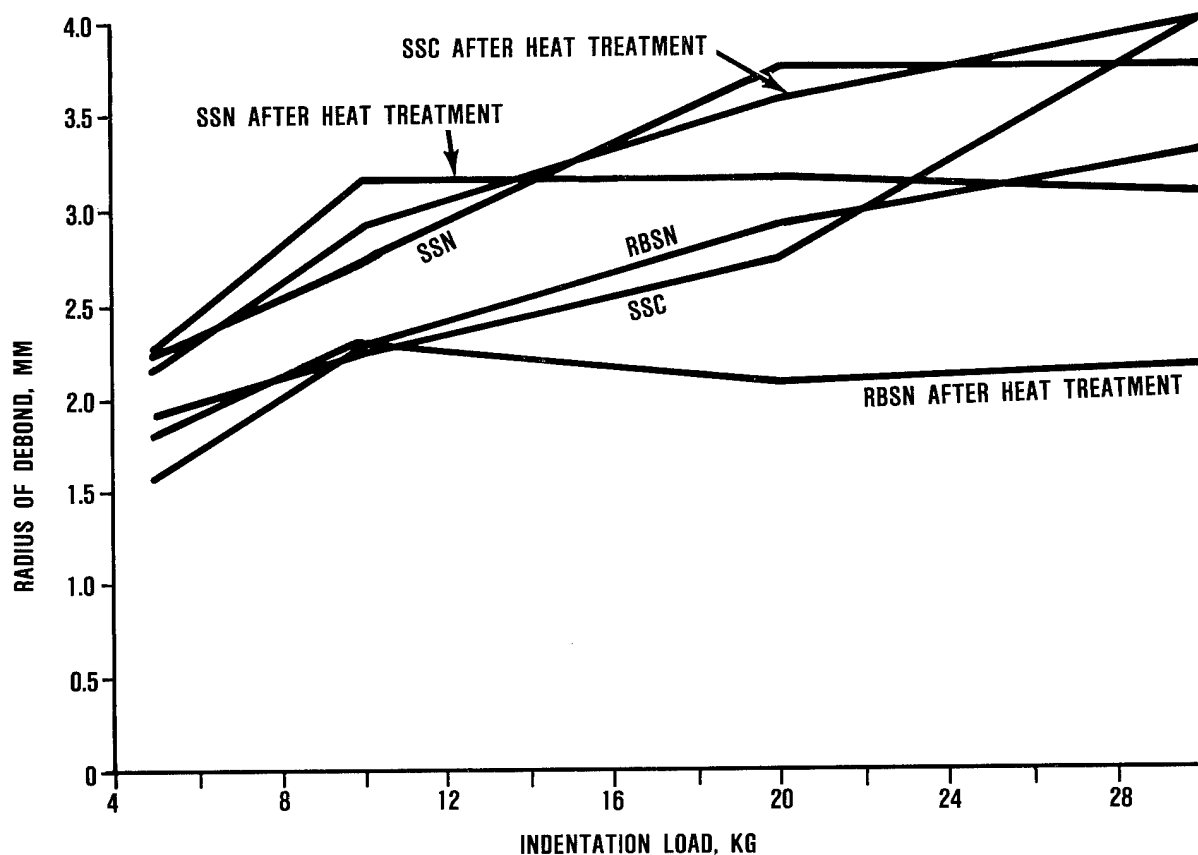
Figure 26. Stoichiometric EB-PVD interlayers resulted in
relatively poor initial adherence.

High-Purity Interlayers. ZrO_2/CVD SiC/SiC specimens were eval-
uated for coating adherence using indentation and line contact test-
ing. For indentation tests, both as-coated and oxidized specimens
spalled at the lowest test loads. Line contact test results were
similar as spalling occurred at the lowest contact loads. Because of
these preliminary results, high-purity interlayer efforts were not
continued.

Diffusion/Gradation Zones. SSN and SSC specimens with nitrogen
ion-mixed sputtered Al interlayers were evaluated for ZrO_2 adherence
using line contact testing. The RBSN system was not evaluated since
cracking and spalling occurred on heat treatment (Figure 35). Contact
testing was conducted on specimens with post-coating heat treatments.
The results suggested poor adherence for the SSN and SSC systems.

Coating Temperature. As-machined substrates coated at 1040C
rather than the baseline 980C were evaluated for adherence using
indentation testing. The results showed that coating at elevated tem-
peratures does not appear to benefit the coating adherence before or
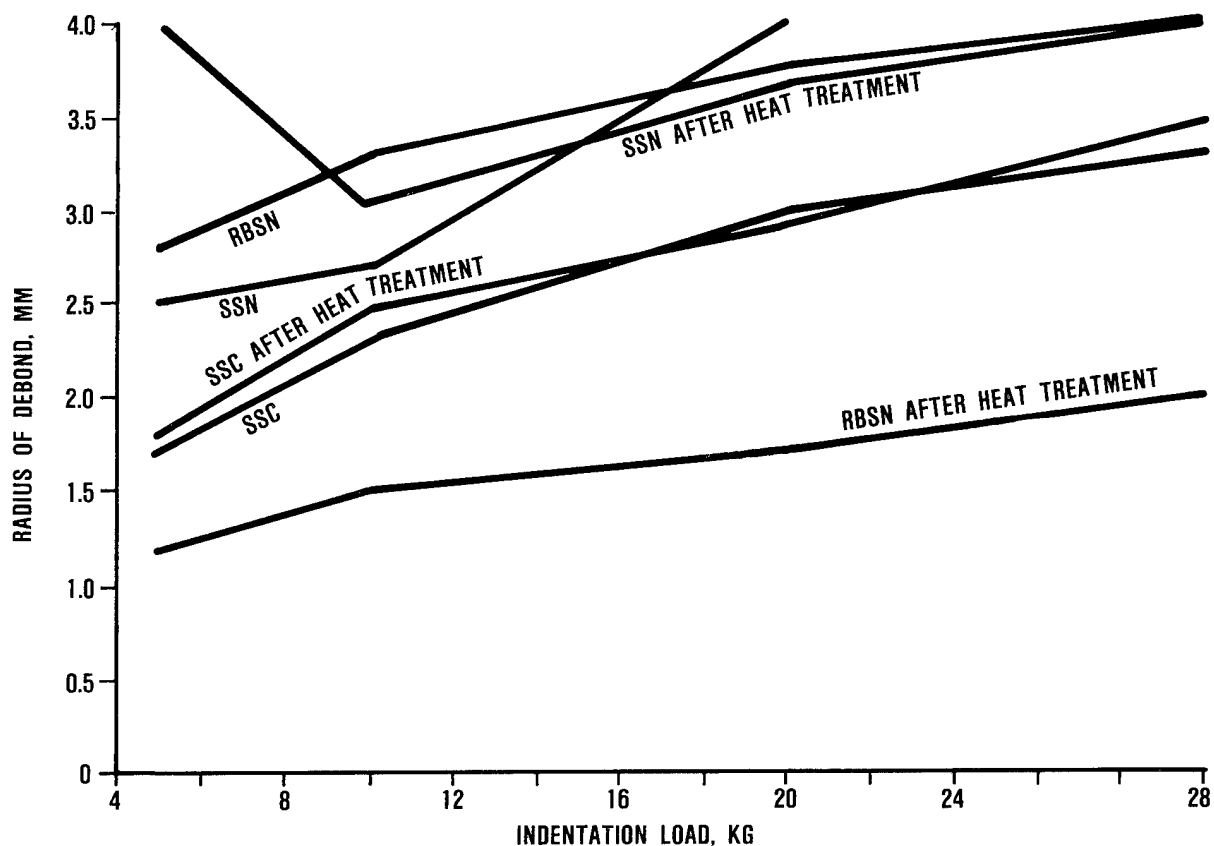
Figure 27. Non-stoichiometric EB-PVD Al₂O₃ interlayers resulted in poor initial coating adherence. The ZrO₂ adherence was slightly less than observed for stoichiometric EB-PVD Al₂O₃.

after oxidation. Adherence for as-coated specimens was equivalent to the baseline for SSN and SSC and slightly less for RBSN. After oxidation exposure, both the coating adherence and the baseline systems degraded significantly.

3.2.4 Selection of Coating/Substrate Systems for Tasks 3 and 4

The most adherent coatings were achieved under the Oxygen Diffusion Barrier and Surface Roughening Studies. From these coating/substrate systems, the two most adherent systems for each substrate were selected for analysis under Tasks 3 and 4. Adherence after oxidation exposure was emphasized more than as-coated adherence since oxidizing conditions exist in turbine engine applications. The indentation and line contact adherence results (after oxidation) are summarized in Tables 4 and 5, respectively, for the Oxygen Diffusion Barrier and Surface Roughening Studies and are combined in Table 6. Table 6 ranks the adherence of the pretreatments for each substrate on a scale of 0

ZrO$_2$

Al$_2$O$_3$

RBSN

1μm

ZrO$_2$

Al$_2$O$_3$

SSN

1μm

ZrO$_2$

Al$_2$O$_3$

SSC

1μm
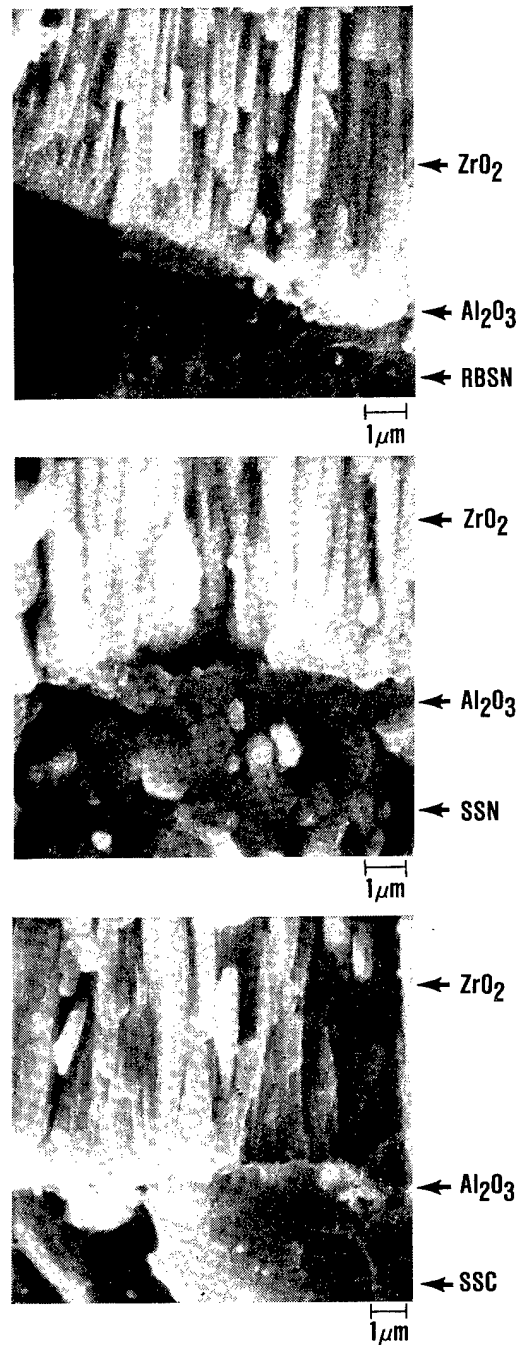
Figure 28. Fracture surfaces of sol-gel alumina interlayer specimens show the coating/interlayer/substrate interfaces exhibiting intimate contact.
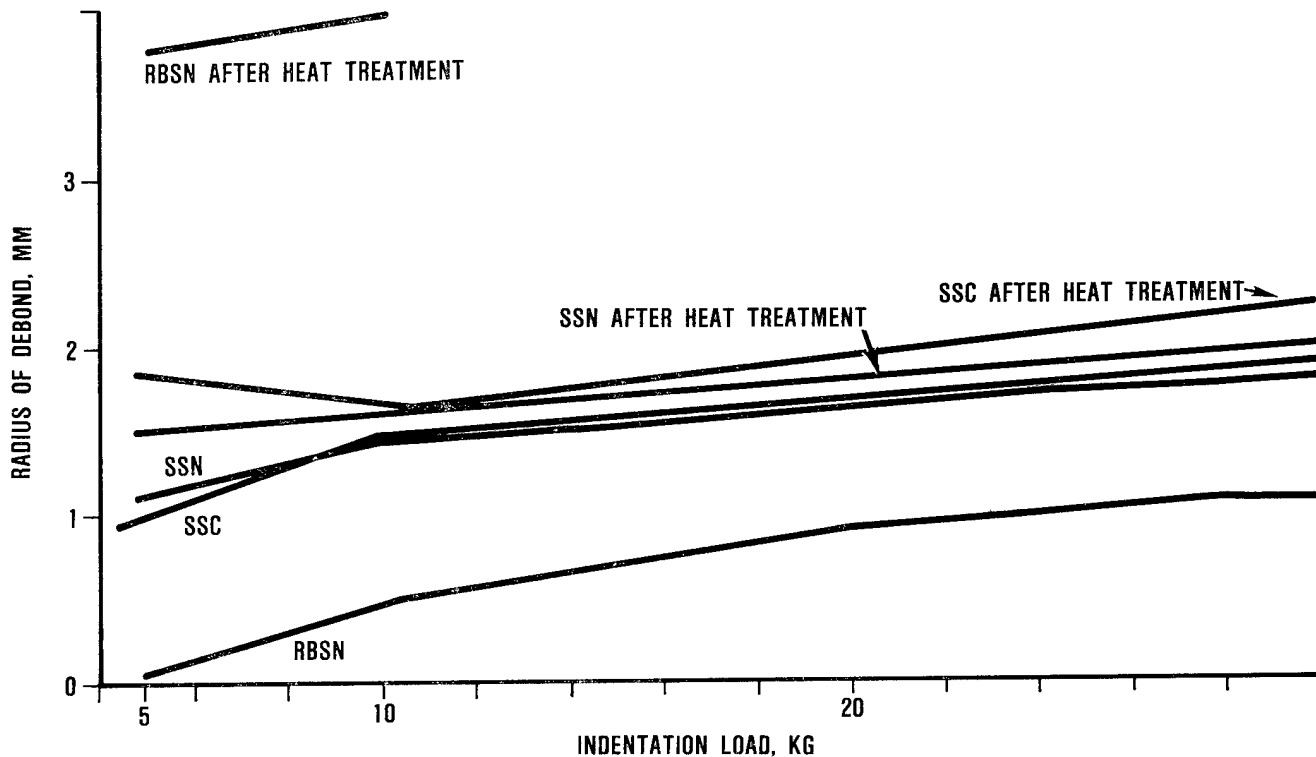
Figure 29. Sol-gel Al₂O₃ interlayers yielded fair adherence for
SSN and SSC which was retained through heat treatment. RBSN
exhibited excellent initial adherence but exhibited a large
adherence loss on heat treatment.

to 6; where 0 is worst and 6 is best. The results show that different pretreatments work best for different substrate materials. CVD Al₂O₃ and CVD AlN interlayers yielded excellent adherence for RBSN. The best adherence for SSN and SSC was achieved using sol-gel alumina interlayers and laser-texturing, though the level of adherence was less than observed for the ZrO₂/CVD Al₂O₃/RBSN and ZrO₂/CVD AlN/RBSN systems. Laser texturing actually resulted in poor adherence for SSN (2 ranking). However, the adherence can probably be improved by reproducing the surface topography obtained for laser-textured SSC, which had good to excellent adherence (5 ranking). Because the potential for improvement exists, laser-texturing was selected over 150-grit machining, which also had an adherence ranking of 2.

3.2.5 Task 2 Summary and Conclusions

During Task 2, Y₂O₃ stabilized ZrO₂ coatings were successfully deposited by EB-PVD on substrates having various pretreatments. The ZrO₂ coatings appeared as clean and adherent as those deposited in Task 1. ZrO₂ coatings deposited at a higher temperature (1040C rather
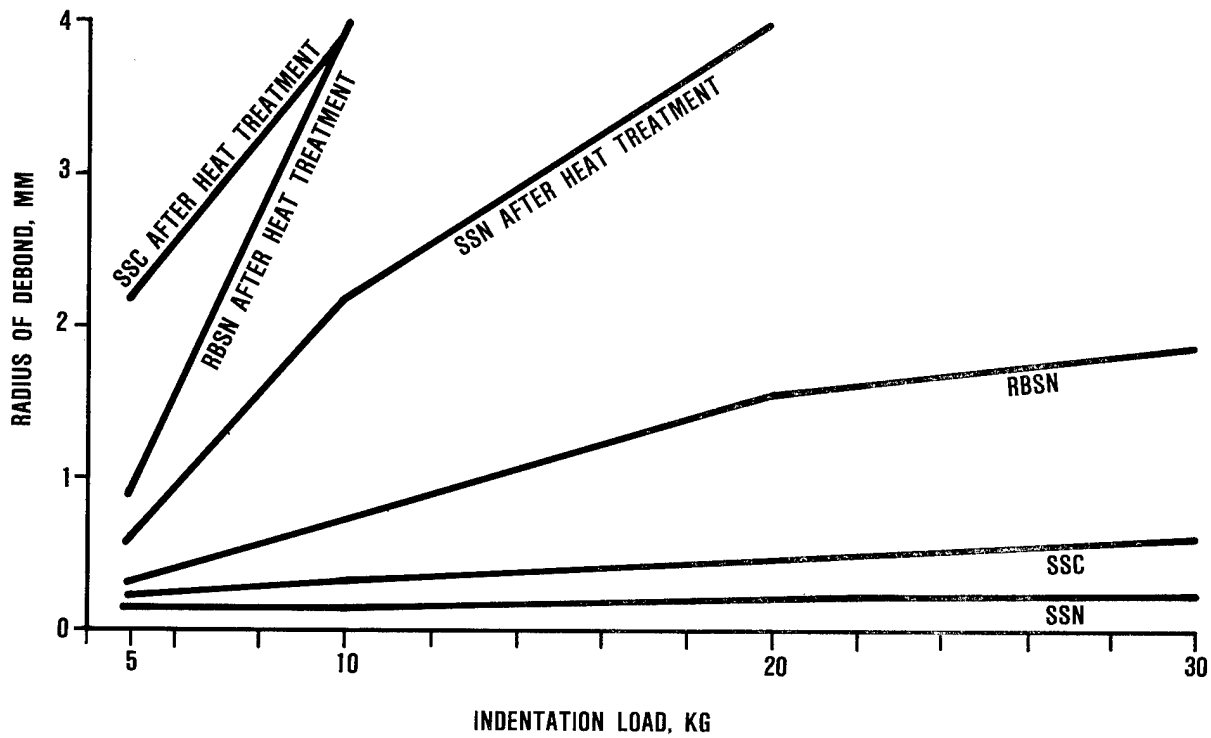
Figure 30.   Results for substrates with 150 grit surface finish.
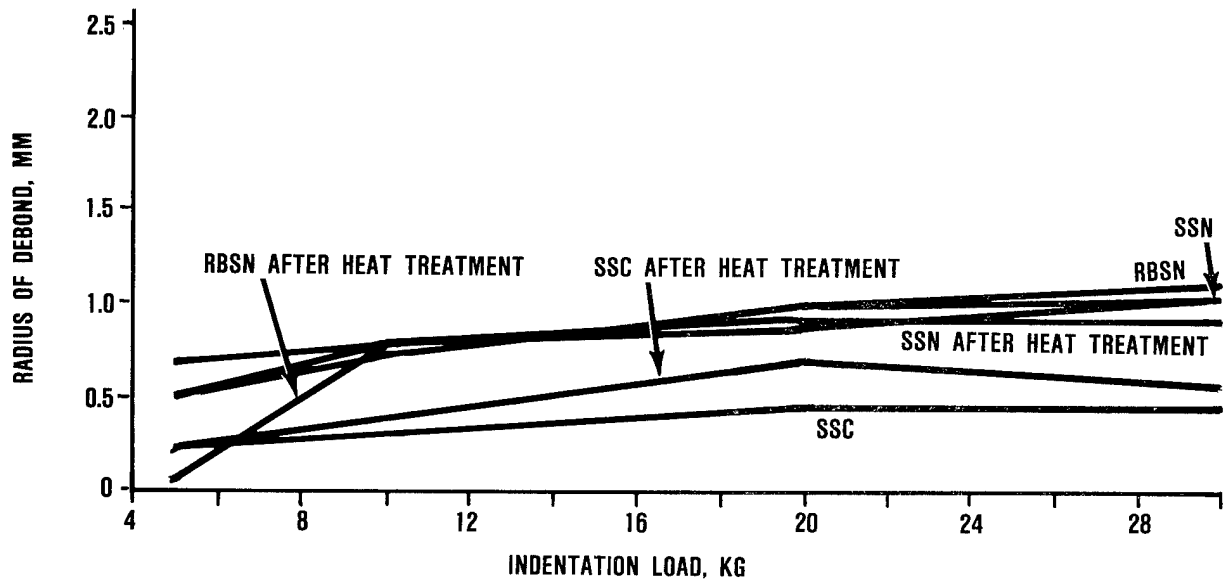
Figure 31.   Laser-textured specimens exhibited excellent coating
adherence before and after heat treatment.   The most
encouraging results were observed for laser textured SSC.

RBSN SSN SSC
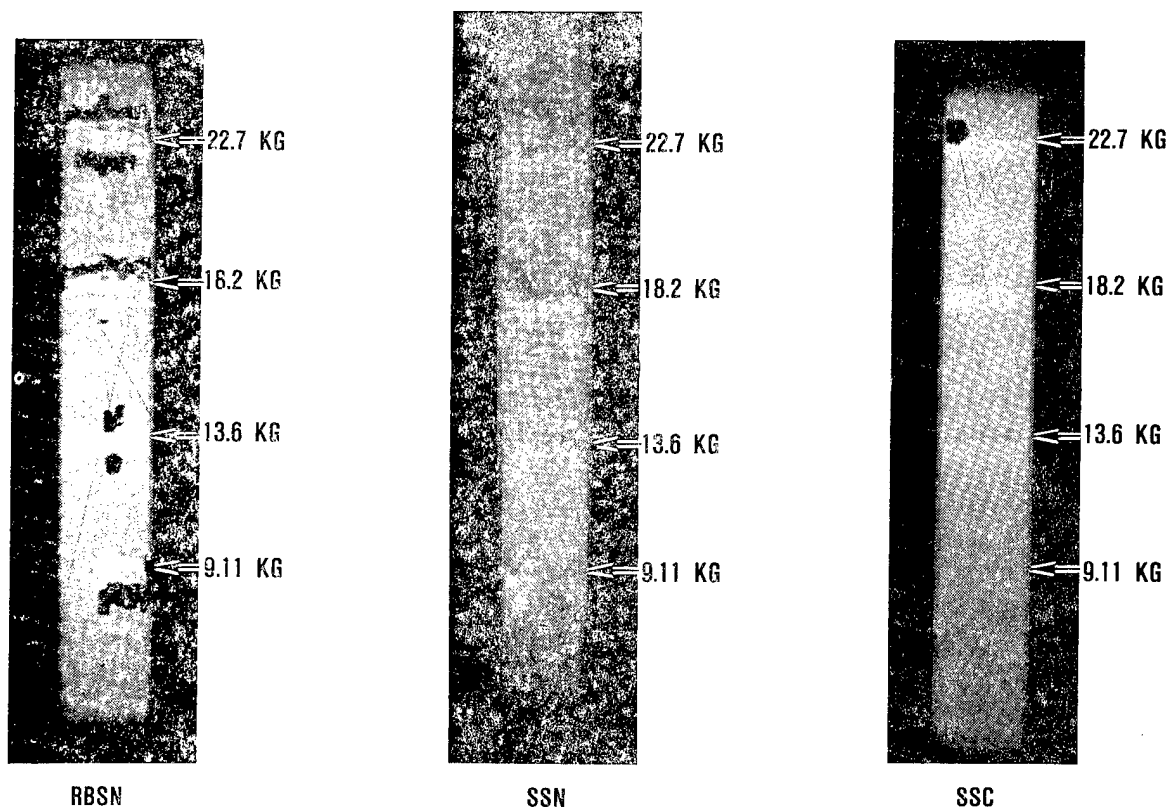
Figure 32. Contact test results on coated laser textured specimens
after oxidation suggest poor adherence for RBSN and SSN and
good adherence for SSC.

than 980C) also appeared clean and adherent, but did not provide any
additional coating adherence. EB-PVD mullite coatings and interlayers
could not be applied because the silica in the mullite source evap-
orated more easily than the alumina resulting in silica-rich coatings.

Oxygen diffusion barriers were developed which successfully pre-
vented adherence degradation previously observed for coated specimens
after oxidation. CVD Al_2O_3 and CVD AlN interlayers worked best for
RBSN, yielding excellent coating adherence after oxidation. Sol-gel
Al_2O_3 worked best for SSN and SSC, yielding fair adherence after
oxidation.

CVD Al_2O_3 and CVD AlN interlayers worked well for the porous RBSN
substrates but not for the dense SSN and SSC substrates. It is specu-
lated that thermal expansion mismatches between the dense interlayer
and the substrate result in interfacial cracking, and that the
residual porosity in the RBSN enables islands of interlayer to remain
adherent due to rooting in the substrate pores.

Sol-gel Al_2O_3 interlayers are preferred for SSN and SSC sub-
strates over CVD Al_2O_3 since relatively good adherence was retained
after oxidation, although the level of adherence was less than that
observed for ZrO_2/CVD Al_2O_3/RBSN. It appears that the 50 percent
porous sol-gel interlayer (submicron-sized porosity) provides improved
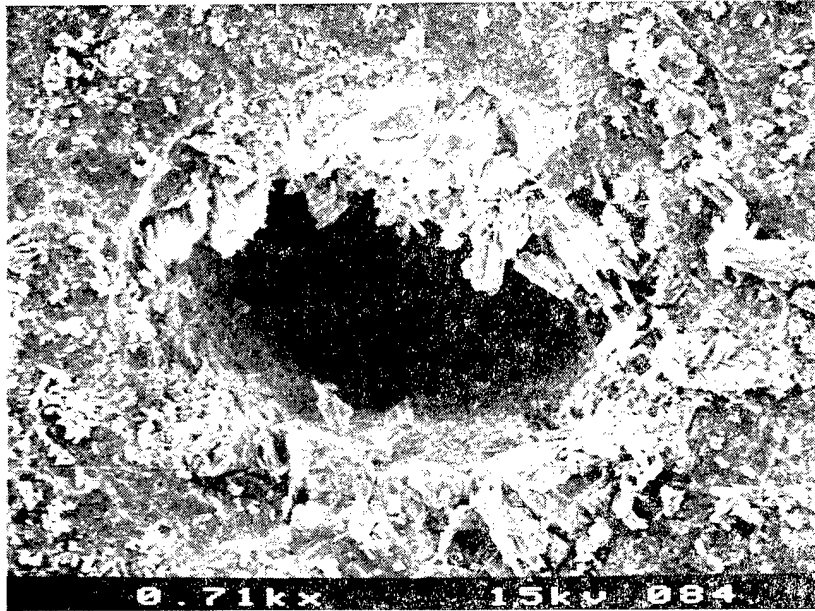
Figure 33. The EB-PVD ZrO_2 did not fill in the deep laser cavities of Si_3N_4 substrates (RBSN shown above) but only coated the cavity walls.
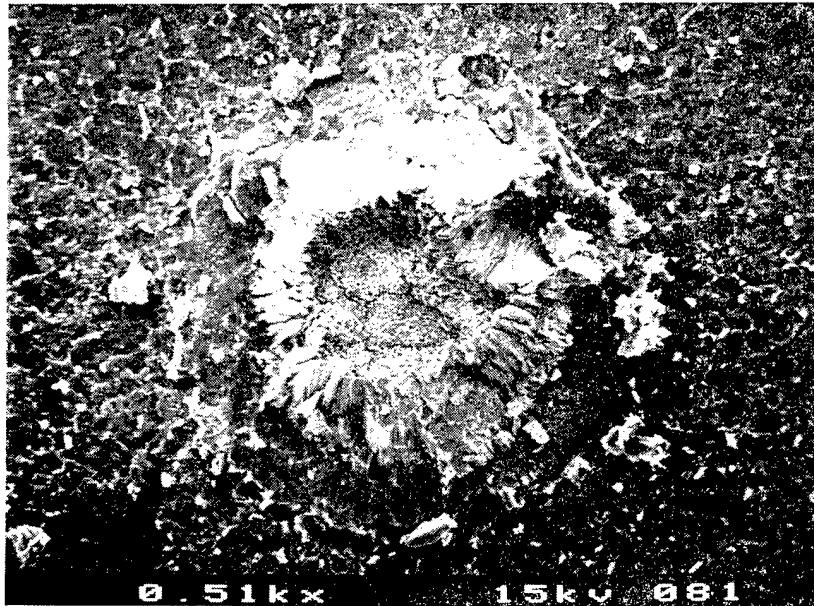
Figure 34. The EB-PVD ZrO_2 infiltrated and filled in the shallow laser cavities on SSC.
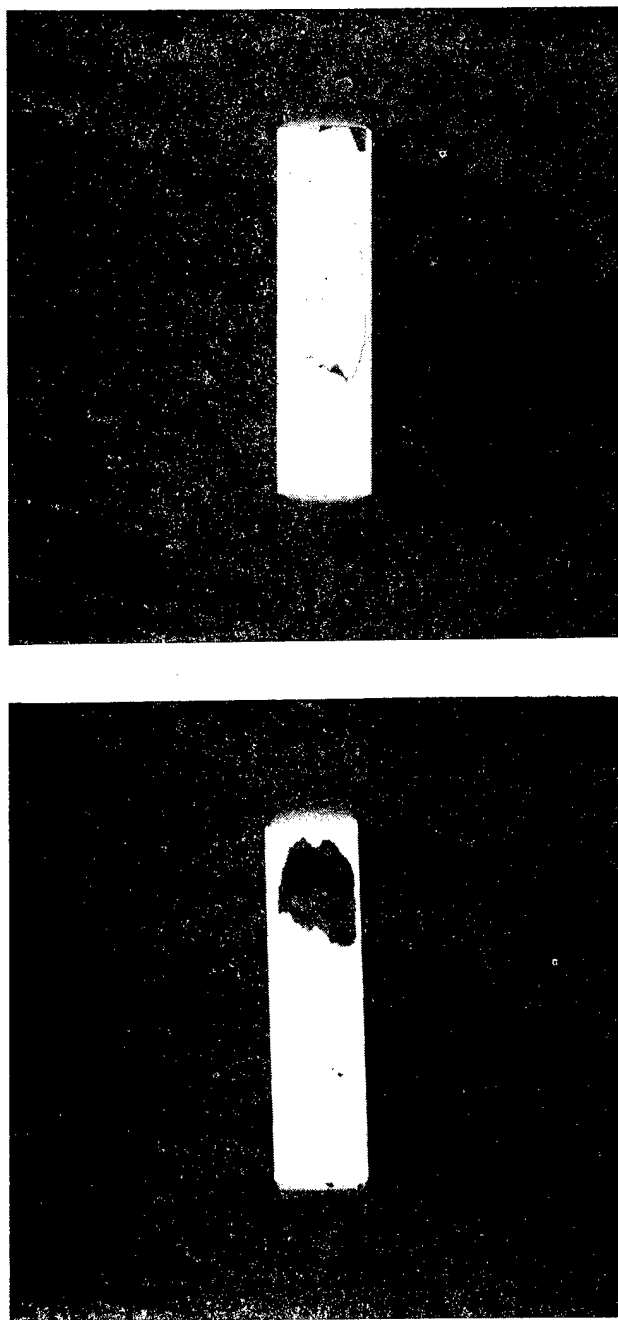
Figure 35. ZrO$_2$ spalling occurred on heat treatment of RBSN
substrates with Ion-mixed (Ar) sputtered Al interlayers.

49

Table 4. Indentation results (after oxidation) for oxygen
diffusion barrier and surface roughening studies

Pretreatment	RBSN	SSN	SSC
CVD Al_2O_3	excellent	poor	poor
CVD AlN	excellent	fair	fair
EB-PVD Al_2O_3 (stoichiometric)	poor	poor	poor
EB-PVD Al_2O_3 (non-stoichiometric)	poor	poor	poor
Sol-gel Al_2O_3	poor	fair	fair
150-grit machine	poor	poor	poor
Laser texture	poor	good	excellent

Table 5. Line contact results (after oxidation) for oxygen
diffusion barrier and surface roughening studies

Pretreatment	RBSN	SSN	SSC
CVD Al_2O_3	excellent	fair	fair
CVD AlN	excellent**	poor	fair
EB-PVD Al_2O_3 (stoichiometric)	good*	fair*	good*
EB-PVD Al_2O_3 (non-stoichiometric)	poor	poor	poor
Sol-gel Al_2O_3	good*	good*	good*
150-grit machine	good	good	fair
Laser texture	poor	poor	good

*Lower than typical coefficient of friction.
**Not tested in contact rig; manually scraped.

Table 6. Adherence summary* (after oxidation) for oxygen
diffusion barrier and surface roughening studies

Pretreatment	RBSN	SSN	SSC
CVD Al_2O_3	6	1	1
CVD AlN	6	1	2
EB-PVD Al_2O_3 (stoichiometric)	2	1	2
EB-PVD Al_2O_3 (non-stoichiometric)	0	0	0
Sol-gel Al_2O_3	2	3	3
150-grit machine	2	2	1
Laser texture	2	2**	5

*Adherence rankings assigned to pretreatment/substrate
combinations by giving numerical values to qualitative
results in Tables 4 and 5 (poor = 0, fair = 1, good =
2, and excellent = 3), then adding the tables together
(0 = worst, 6 = best).
**Chosen over 150-grit machining because potential for
improvement exists.

strain tolerance, which limits interfacial cracking due to thermal expansion mismatches but at the cost of interlayer coehesive strength.

Roughening the substrate through laser-texturing significantly improved both the as-coated and oxidized coating adherence for SSC. The good adherence observed for the laser-textured SSC after oxidation exposure was encouraging considering no interlayer was used to prevent oxidation of the interface. Results were not as encouraging for laser-textured RBSN and SSN. However, the surface cavities were much deeper than those produced on SSC and were not completely filled in with ZrO_2. Therefore, the potential for improvement exists. One negative aspect of laser-texturing is that the coating adherence improvement is accompanied by a decrease in substrate strength associated with the surface cavities.

The two pretreatments yielding the best ZrO_2 coating adherence for each substrate were selected for analysis in Tasks 3 and 4. The most adherent systems were chosen based on adherence after oxidation (Table 7). Different pretreatments worked best for different substrate materials. CVD Al_2O_3 and CVD AlN interlayers yielded the best adherence for RBSN, while sol-gel alumina interlayers and laser-texturing gave the best adherence for SSN and SSC.

3.3 TASK 3 - CONTACT STRESS TESTING AND FRICTION MEASUREMENTS

In Task 3, the most adherent coating/substrate systems from Task 2 were evaluated for strength, resistance to thermal spalling, and friction characteristics. Friction test specimens were exposed to high contact stresses during testing. These same specimens were then used in Task 4, Post-Contact Strength Measurements, to evaluate contact stress damage resistance.

3.3.1 Specimen Preparation and Inspection

Task 3 substrate pretreatments, selected at the conclusion of Task 2, are shown in Table 7. Test bars of each substrate material were procured, pretreated and EB-PVD coated according to the procedures used in Task 2. The laser texturing procedures were modified to yield shallower surface cavities in an attempt to minimize the strength loss associated with this treatment. Also, shallower cavities should yield better coating adherence for SSN than achieved in

Table 7. Pretreatments selected for Tasks 3 and 4

RBSN	SSN	SSC
CVD alumina	sol-gel alumina	sol-gel alumina
CVD aluminum nitride	laser machining	laser machining

Task 2.*   Extra laser-textured substrates were prepared for strength evaluation.   In addition, as-machined substrates were prepared to provide baseline strength, friction, and contact damage resistance.   All EB-PVD zirconia-coated specimens designated for testing were heat-treated at 1200C for 100 hours in order to stabilize the interface prior to evaluation.   A few as-coated specimens were used for interface analysis.

All coated specimens were visually inspected after EB-PVD coating.   Most coatings appeared clean and adherent, although coating discoloration was observed for coatings from EB-PVD Run No. 124, which involved CVD Al_2O_3-coated RBSN.   Most of the specimens from this run were brown, some having a mottled appearance.   However, EDX analysis of the zirconia coating surface detected no chemical impurities.   On heat treatment, several of these specimens spalled and most exhibited a rust-colored reaction product on the substrate.   This effect was not observed for specimens from any other coating run.   EDX analysis of a spalled area suggested that the Al_2O_3/RBSN substrate was contaminated prior to EB-PVD coating; EDX detected potassium (Figure 36).   The strong aluminum peak suggests that the failure occurred at the ZrO_2/Al_2O_3 interface.

For specimens other than those from Run No. 124, only color changes in the ZrO_2 coating from blue or gray to white (due to oxidation of excess zirconium in the ZrO_2 coating) occurred on heat treatment.

3.3.2 Flexure Strength

Flexure strength testing was conducted on both the as-machined substrates and coated specimens.   The as-machined substrate strengths served as a baseline in determining the effect of the coating procedures on the substrate strength.   The coated strengths served as a baseline in determining the retained strength (or contact damage resistance) after contact stress exposure.

3.3.2.1 Flexure Test Procedures.   Flexure testing was conducted at room temperature, 1000C, and 1375C in air.   The procedures for room temperature testing were the same as those used in Task 1.   Similar procedures were used at elevated temperatures except that specimens were held for 5 minutes at temperature prior to starting each test. The flexure strength test matrix is shown in Table 8.

Because Task 2 flexure results identified a strength loss associated with laser-texturing, additional testing of uncoated, laser-textured SSN and SSC was conducted in order to separate the strength effects of laser-texturing and coating.

---

*During Task 2, poor EB-PVD ZrO_2 coating adherence resulted from incomplete filling of the deep surface cavities in laser-textured SSN.

ENERGY DISPERSIVE X-RAY SPECTRUM
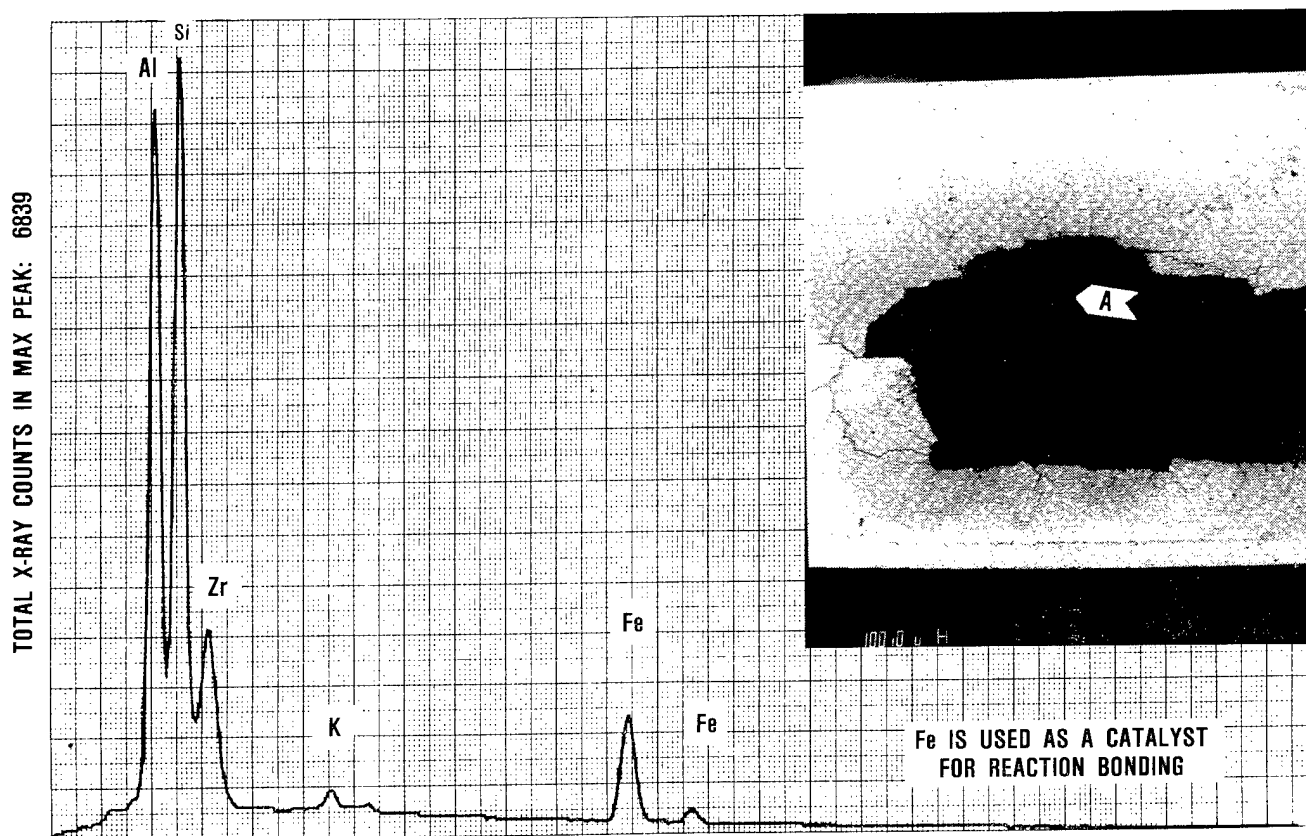
Figure 36.   ZrO$_2$ coatings from run #124 spalled during heat
treatment.   Potassium (K) was detected in the spalled area.

Table 8.   Task 3 flexure strength test matrix

| | Number of tests | | |
Substrate	25C	1000C	1375C
RBSN	10	6	6
SSN	10	6	6
SSC	10	6	6
Coating/substrate system			
ZrO$_2$/CVD Al$_2$O$_3$/RBSN	10	6	6
ZrO$_2$/CVD AlN/RBSN	10	6	6
ZrO$_2$/sol-gel Al$_2$O$_3$/SSN	10	6	6
ZrO$_2$/laser-textured SSN	10	6	6
ZrO$_2$/sol-gel Al$_2$O$_3$/SSC	10	6	6
ZrO$_2$/laser-textured SSC	10	6	6

After flexure testing, all fracture surfaces were examined optically up to 40X magnification to determine the failure origins for each system. The fractography results of as-machined substrates and coated specimens were compared to determine if the coating procedures had any effect on the failure characteristics.

3.3.2.2 Flexure Test Results. The flexure test results for the as-machined substrates are shown in Table 9. The strengths measured for RBSN and SSN are typical for these materials based on past GTEC experience. SSC strengths were lower than typical (340 to 400 MPa). In most cases, RBSN failed from either residual porosity or light colored inclusions at room and elevated temperatures. SSN exhibited high-energy failures at room temperature (bars broke into several pieces). The origins were primarily metallic-looking inclusions. At 1000C, low-energy fractures occurred (bar broke in two pieces having flat, relatively smooth fracture surfaces). All failures originated from the tensile face. At 1375C, SSN exhibited creep deformation as evidenced by the nonlinear load deflection curves and a rough fracture surface. SSC exhibited surface failures at room temperature and 1000C. At 1375C, the origins were light colored areas, usually associated with residual porosity in SSC.

Table 9. As-machined substrate strength

Substrate	Temperature (C)	Strength ± std dev (MPa)
RBSN	RT*	296 ±31
	1000	361 ±18
	1375	319 ±52
SSN	RT	592 ±67
	1000	611 ±51
	1375	134 ± 6
SSC	RT	286 ±26
	1000	272 ±21
	1375	295 ±12

*Room Temperature

The flexure test results for laser-textured SSN and SSC (Table 10) show that a significant strength loss results from laser texturing. Laser-textured specimens failed at the cavities produced by laser-texturing except for SSN at 1375C, where softening of the grain boundary phases predominated. For SSC, several of the failure origins were associated with spalling on the chamfered edges of the test bars which occurred during laser-texturing (Figure 37). To evaluate the effect on strength, some SSC specimens were laser-machined over the

Table 10. Laser-textured substrate strength

Substrate	Temperature (C)	Strength ± std dev (MPa)	Reduction (percent)
SSN	RT	450 ±30	24
	1000	502 ±57	18
	1375	111 ± 7	17
SSC	RT	205 ±17	28
	1000	224 ± 8	18
	1375	225 ±13	24
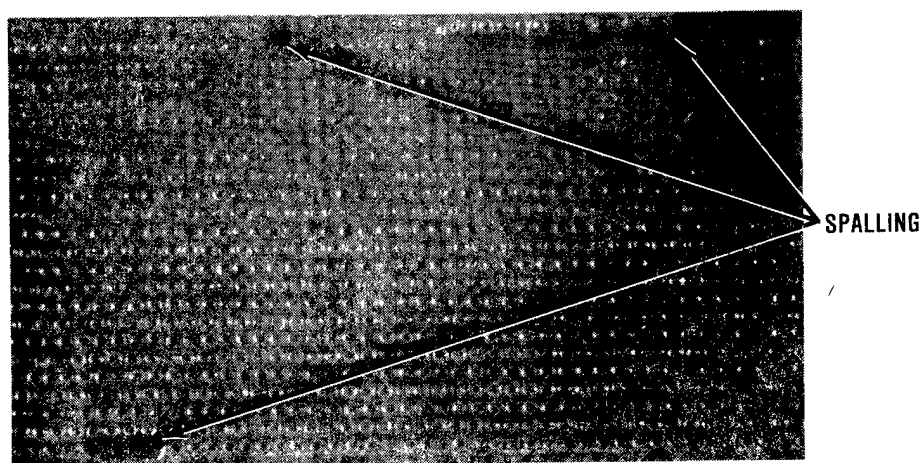
Figure 37. Laser machining of SSC substrates resulted in spalling on edges.

center section of the bar, leaving the edges non-textured by the laser (Figure 38). As shown in Table 11, the strength reduction was not as significant. Afterwards, all laser-textured SSC specimens to be coated were rechamfered on the edges to eliminate the effects of edge spalling. Therefore, the results in Table 11 are expected to better represent the strength characteristics of laser-textured SSC.

The room temperature strengths of the Task 3 laser-textured specimens were lower than exhibited by Task 2 laser-textured specimens which had cavity depths up to three times greater. This result suggests that the strength was not predominated by the cavity depth but possibly by microcracks extending from the cavities. Both SSN and SSC exhibited less strength reduction when tested at elevated temperatures. Possible explanations are that microcracks extending from the laser cavities blunt or heal during the test (5 minutes hold at temperature) or that laser-texturing produces residual stress effects relieved at elevated temperatures.
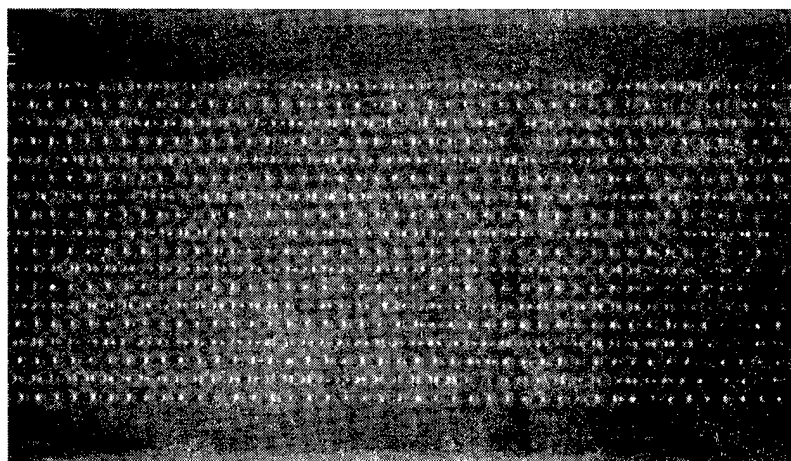
Figure 38. Some specimens were left untreated at the edges to eliminate spalling.

Table 11. Strength of rechamfered laser-textured SSC

Substrate	Temperature (C)	Strength ± std dev (MPa)	Reduction (percent)
SSC	RT	220 ±10	23
	1000	241 ± 3	11
	1375	271 ±13	8

The flexure test results for the six coated systems are summarized in Table 12. Both the ZrO_2/CVD Al_2O_3/RBSN and ZrO_2/CVD AlN/RBSN systems exhibited significantly lower room temprature strength than as-machined RBSN (-29 and -21 percent, respectively). However, these two systems regained strength at elevated temperatures, suggesting that the strength loss at room temperature was a residual stress effect. At 1375C the ZrO_2/CVD Al_2O_3/RBSN and ZrO_2/CVD AlN/RBSN systems exhibited strengths higher than baseline RBSN (+10 and +4 percent, respectively). Fractography results suggested that the room temperature and 1000C failures originate from substrate surface flaws and the 1375C failures from internal flaws. SEM analysis of these specimens showed that both the surface and internal origins were associated with the residual porosity of the RBSN (Figure 39).

The ZrO_2/sol-gel Al_2O_3/SSN system exhibited approximately 35 percent lower strength at room temperature and 1000C relative to as-machined SSN. Fractography suggested that the strength loss was not associated with the coating since the failures originated at large, yttria-based (sintering additive in SSN) flaws, as shown in Figure 40. The cause of the strength loss was determined to be due to the heat treatment at 1200C for 100 hours. Fifteen as-machined SSN substrates were exposed to the same heat treatment to support this hypothesis. A strength of 435 ±71 MPa resulted, a 27 percent drop. Therefore, the

Table 12. Baseline flexure strength results for coated systems
(heat-treated at 1200C for 100 hours)

Coating/substrate system	Temperature (C)	Strength ± std dev (MPa)	
ZrO_2/CVD Al_2O_3/RBSN	RT	211	±33
	1000	303	±32
	1375	352	±49
ZrO_2/CVD AlN/RBSN	RT	234	±39
	1000	321	±59
	1375	333	±78
ZrO_2/sol-gel Al_2O_3/SSN	RT	383	±46
	1000	411	±19
	1375	125	±17
ZrO_2/laser-textured SSN	RT	353	± 9
	1000	408	±101
	1375	125	±26
ZrO_2/sol-gel Al_2O_3/SSC	RT	279	±23
	1000	363	±22
	1375	268	±32
ZrO_2/laser-textured SSC	RT	238	±46
	1000	288	±22
	1375	263	±31

lower strength observed for ZrO_2/sol-gel Al_2O_3/SSN appears to be inde-
pendent of the coating, and 435 MPa was subsequently used as the room
temperature and 1000C baseline for SSN.

The ZrO_2/sol-gel Al_2O_3/SSC system exhibited no change in strength
at room temperature and 1375C relative to the as-machined SSC.* At
1000C, a 34 percent increase in strength was observed. However, since
all failures still originated from residual porosity in the SSC, the
strength increase at 1000C is believed to be coincidental.

Both the ZrO_2/laser-textured SSN and ZrO_2/laser-textured SSC sys-
tems exhibited some strength loss at room temperature relative to their
respective substrate materials.** At elevated temperatures, the strength

*The baseline strengths observed for SSC under the current program
were less than typical for this material. The lower strength was
attributed to the atypical residual porosity observed.

**435 MPa was used as the baseline for SSN because of the effect of the
heat treatment on strength.

ZrO₂/CVD Al₂O₃/RBSN TESTED
AT ROOM TEMPERATURE (214 MPa)

ZrO₂/CVD AlN/RBSN TESTED
AT ROOM TEMPERATURE (221 MPa)

ZrO₂/CVD Al₂O₃/RBSN TESTED
AT 1000C (330 MPa)

ZrO₂/CVD AlN/RBSN TESTED
AT 1375C (397 MPa)
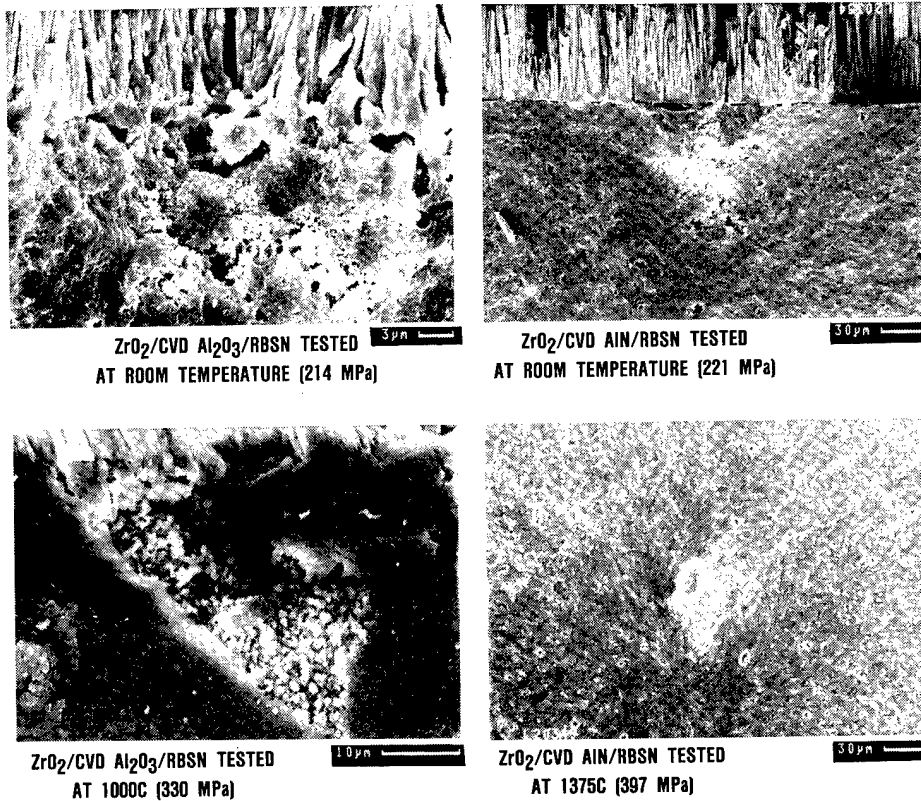
Figure 39. Both surface and internal failures for the ZrO_2/CVD Al_2O_3/RBSN and ZrO_2/CVD AlN/RBSN systems are associated with residual porosity in RBSN.

ROOM TEMPERATURE (383 MPa)

1000C (409 MPa)
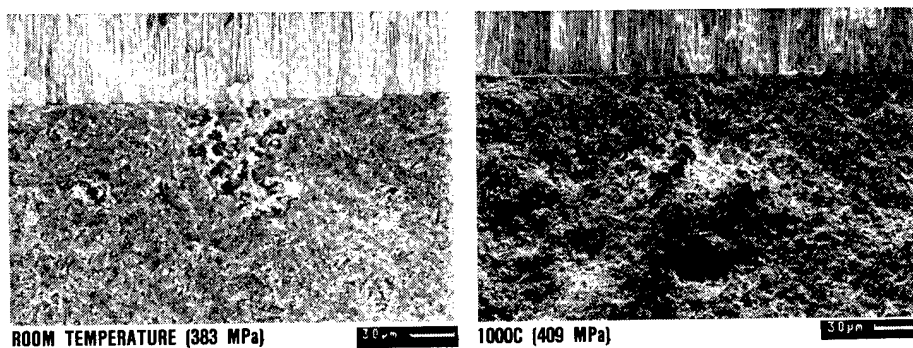
Figure 40. ZrO_2/Sol-gel Al_2O_3/SSN substrates failed primarily from large substrate flaws.

changes were insignificant (ZrO_2/laser-textured SSC actually exhibited a higher strength at 1000C than SSC). The failure origins were at the surface cavities produced by laser-texturing (except for ZrO_2/laser-textured SSN at 1375C where deformation in fast fracture was observed), as shown in Figure 41.

For all coating/substrate systems, glass buildup occurred on the ZrO_2 coatings under the hot-pressed SiC flexure load pins at 1375C (Figure 42). The glass buildup was most significant for systems exhibiting the highest strength at 1375C (e.g., ZrO_2/CVD Al_2O_3/RBSN and ZrO_2/CVD AlN/RBSN). Therefore, the magnitude of the load on the pin is a factor. These results suggest that there may be some sticking problems during the 1375C coated contact testing (SSC contact pins are to be used against the ZrO_2 coatings). To further assess this problem, studies

ROOM TEMPERATURE (265 MPa)   30μm

ZrO_2/LASER SSC

ROOM TEMPERATURE (354 MPa)   30μm

ZrO_2/LASER SSN
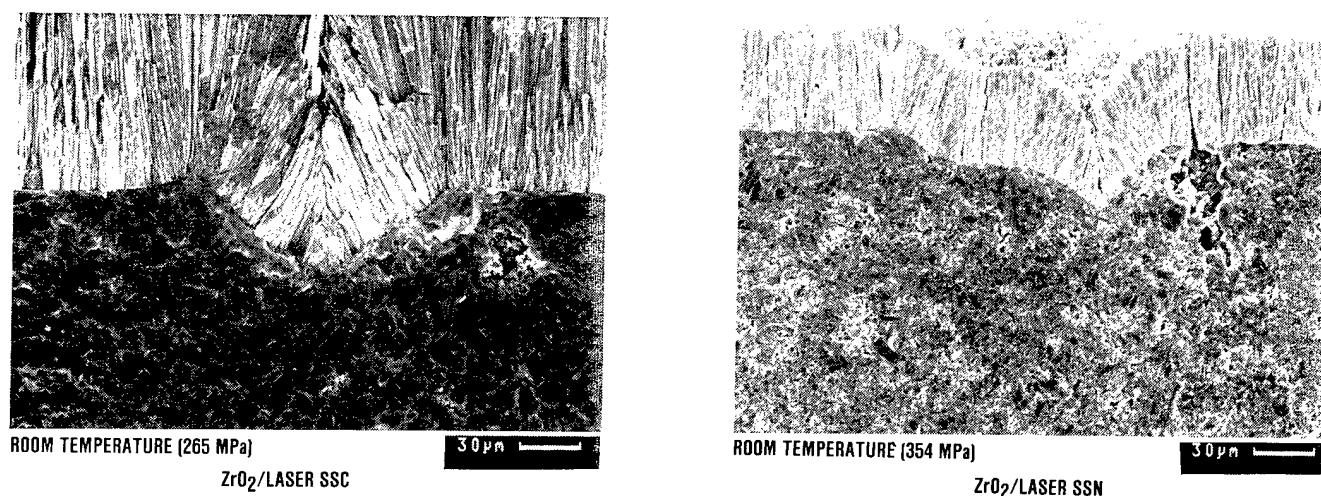
Figure 41. Failures in laser-textured specimens initiated at surface cavities on substrates.
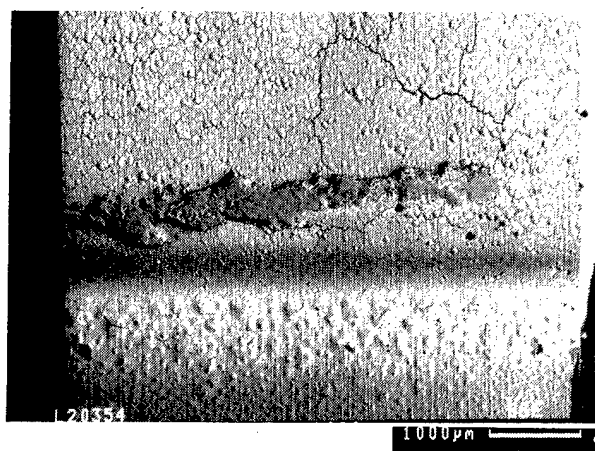
Figure 42. The EB-PVD ZrO_2 coatings exhibited glass buildup under the flexural load pins during 1375C tests.

were conducted to evaluate the sticking resistance of EB-PVD ZrO_2 against itself and the three substrate materials. The results indicate the ZrO_2 coating sticks to SiO_2 formers (e.g., Si_3N_4 and SiC) but not to itself. Therefore, in heat engine applications at this temperature, both contacting surfaces would need to be coated to prevent sticking.

3.3.3 Cyclic Thermal Testing

3.3.3.1 Cyclic Thermal Test Procedures. Thermal cyclic testing was conducted in GTEC's cyclic thermal shock rig. The Task 3 coating/ substrate systems were tested according to the test matrix in Table 13.

Each test consisted of three cycles. The specimens were heated to the test temperature in 15 seconds or less then airblast cooled to less than 150C. This cycle was repeated two times, followed by visual inspection of the specimens to check for spalling delamination or coating degradation.

3.3.3.2 Cyclic Thermal Test Results. The results for 1000C and 1375C cyclic thermal tests are shown in Figures 43 and 44, respectively. Three systems survived cyclic testing to 1000C: ZrO_2/CVD Al_2O_3/RBSN, ZrO_2/CVD AlN/RBSN, and ZrO_2/sol-gel Al_2O_3/SSN. These systems exhibited no visual evidence of reaction or degradation. For the three remaining systems, spalling occurred only on the chamfered edges where localized heating was observed during testing. For the ZrO_2/laser-textured SSN and ZrO_2/laser-textured SSC systems, only one of the four specimens tested exhibited edge spalling. Two ZrO_2/sol-gel Al_2O_3/SSC specimens edge spalled.

Three systems survived cyclic testing to 1375C: ZrO_2/CVD Al_2O_3/ RBSN, ZrO_2/laser-textured SSN, and ZrO_2/laser-textured SSC. These systems exhibited no visual evidence of reaction or degradation. For ZrO_2/CVD AlN/RBSN, one of four specimens exhibited spalling during the first quench. No further spalling occurred during subsequent cycles. The other specimens survived all three cycles. ZrO_2/sol-gel Al_2O_3/SSN and SSC exhibited poor spalling resistance in 1375C tests.

Table 13. Cyclic thermal test matrix and results

Coating/substrate system	Number of tests 1000C	1375C	Results 1000C	1375C
ZrO_2/CVD Al_2O_3/RBSN	4	4	OK	OK
ZrO_2/CVD AlN/RBSN	4	4	OK	1 spalled
ZrO_2/sol-gel Al_2O_3/SSN	4	4	OK	4 spalled
ZrO_2/laser-textured SSN	4	4	1 spalled+	OK
ZrO_2/sol-gel Al_2O_3/SSC	4	4	2 spalled	3 spalled
ZrO_2/laser-textured SSC	4	4	1 spalled+	OK

+ minor edge spalling only

ZrO$_2$/CVDAl$_2$O$_3$/RBSN   ZrO$_2$/SOL-GEL Al$_2$O$_3$/SSN   ZrO$_2$/SOL-GEL Al$_2$O$_3$/SSC

SPALL

ZrO$_2$/CVD AlN/RBSN   ZrO$_2$/LASER SSN   ZrO$_2$/LASER SSC
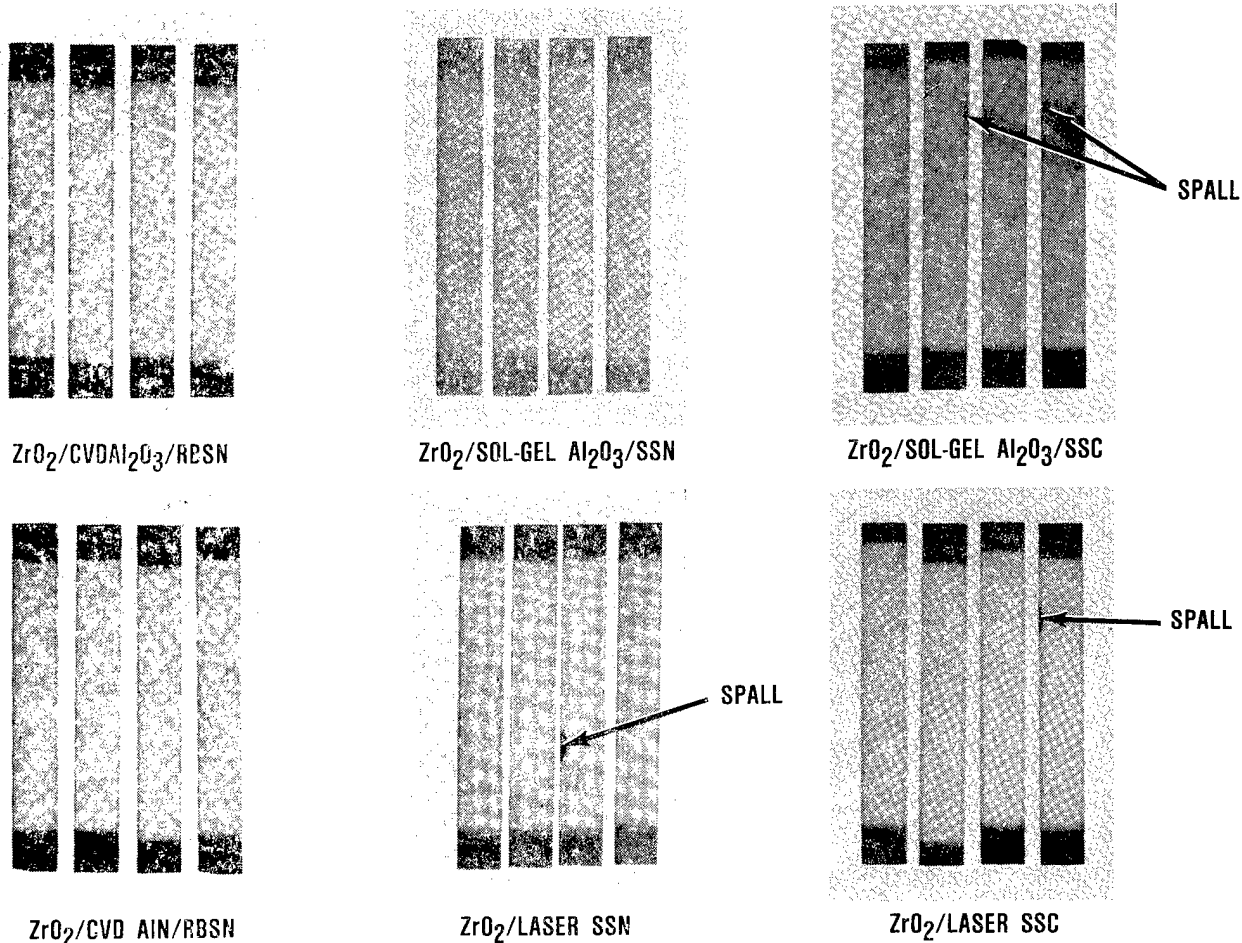
SPALL

SPALL

Figure 43.   Three systems survived 1000C cyclic thermal testing while
the remaining systems exhibited some edge spalling.

3.3.4 Uncoated Contact Testing

Contact testing was conducted on as-machined RBSN, SSN, and SSC to
establish the baseline friction characteristics and, through subsequent
flexure strength testing, to determine the threshold contact test condi-
tions for damaging the substrate materials.   The threshold contact test
conditions established were used to select test conditions for coated
contact tests.

3.3.4.1 Uncoated Contact Test Procedures.   Contact tests were con-
ducted using both point and line contact geometries.   The original test
plan included line contact only since prior analyses of Si$_3$N$_4$ and SiC
ceramics suggested the test conditions selected should induce contact
damage.   However, problems were encountered in obtaining thresholds for
contact damage.   Therefore, point contact, which generates higher con-
tact stresses, was incorporated into the test plan.

ZrO$_2$/CVDAl$_2$O$_3$/RBSN   ZrO$_2$/SOL-GEL Al$_2$O$_3$/SSN   ZrO$_2$/SOL-GEL Al$_2$O$_3$/SSC

SPALL   SPALL

ZrO$_2$/CVD AIN/RBSN   ZrO$_2$/LASER SSN   ZrO$_2$/LASER SSC
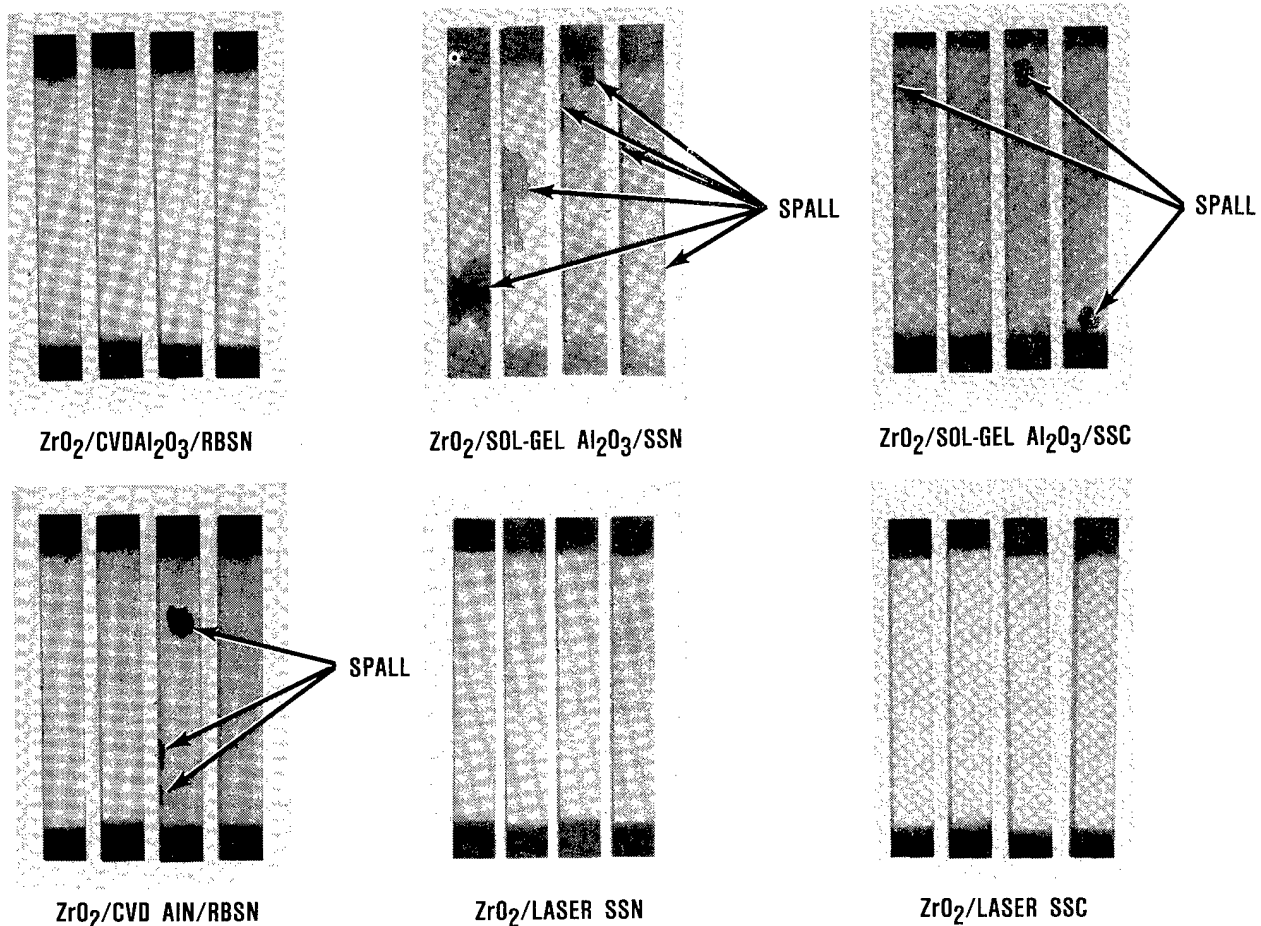
SPALL

Figure 44.   Three systems survived 1375C cyclic testing.   The remaining
systems exhibited face and edge spalling.

Contact testing involved displacing a normal force, applied through
a SSC contact pin onto the test specimen at its mid-span, 1.52 mm across
the surface while monitoring the tangential force (see Section 3.1.3.2
for description of test rig).   The original test matrix for contact
testing, which included only line contact, is shown in Table 14.   Tests
were conducted up to 1375C for RBSN and SSC.   SSN was only tested to
1200C since flexure test results suggested 1375C was beyond its range of
use.   For elevated temperature tests, the normal load was applied and
held 30 minutes at temperature before displacing the contact.   This hold
period allowed for sticking at the contact interface due to substrate
oxidation.   Sticking of component interfaces is frequently observed in
ceramic gas turbine engines.
     Because line contact did not yield the contact damage threshold
information necessary to choose the test conditions for coated contact
specimens, more severe test conditions were pursued.   Contact testing

Table 14. Line contact test matrix

Temperature (C)	Load (kg)		
	4.5	11.3	22.7
RT	4	4	4
1000	4	4	4
1375*	4	4	4

*SSN tested at 1200C instead of 1375C

was conducted on spare substrate specimens using a point contact geometry. As a first step, tests were conducted at the same temperatures and loads as used for line contact. For SSN*, testing was extended to loads of 27.2, 39.3, and 45.4 kg. The limited number of substrates available resulted in the test matrix shown in Table 15.

Contact tested specimens were flexure tested at room temperature to determine the retained strength. The contact tested side of the specimen was in tension. All fracture surfaces were examined up to 40X to characterize the failure origins as either contact or non-contact.

3.3.4.2 Uncoated Contact Test Results.

Friction Characteristics. The static and dynamic friction characteristics observed for the as-machined substrate materials are

Table 15. Point contact test matrix

Substrate	Temperature (C)	Load (kg)					
		4.5	11.3	22.7	27.2	39.3	45.4
RBSN	RT		1	2			
	1000			2			
	1375			2			
SSN	RT	3	3	3	3	4	4
	1000	3	3	3			
	1200	3	3	3			
SSC	RT	3	3	3			
	1000		1	3			
	1375		1	3			

*The SSN substrates were heat treated 100 hours at 1200C to provide a better baseline for coated SSN contact results.

summarized in Figures 45 and 46, respectively. The substrate materials exhibited significantly higher static coefficients of friction at elevated temperature. This trend was also observed for the dynamic friction of SSN and SSC. For RBSN, the increase was not as significant. The increased friction coefficient at elevated temperatures was attributed to SiO_2 formation on the substrate materials in oxidizing atmospheres. Based on GTEC's prior experience with Si_3N_4 and SiC ceramics, the friction coefficients observed are characteristic of the materials evaluated.[7,8]

STATIC FRICTION
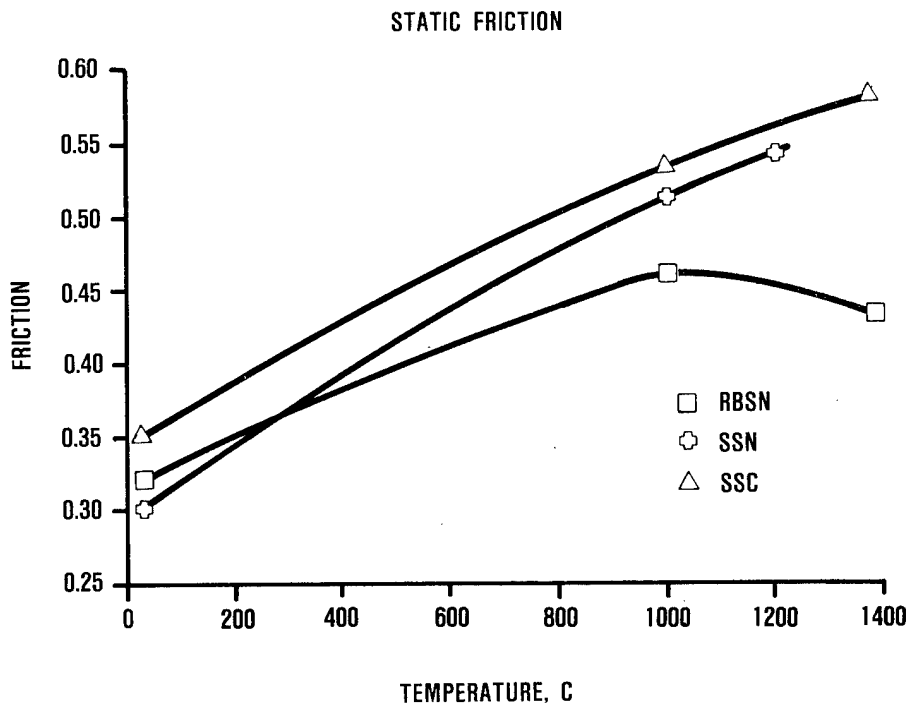
TEMPERATURE, C

Figure 45. The static friction of RBSN, SSN, and SSC increased at elevated temperatures.

Retained Strength. Strength results indicated line contact testing up to 22.7 kg was inadequate to cause contact stress damage in most cases. The only contact damage observed was for RBSN; two specimens exhibited 25 percent reductions in strength after contact testing at 1000C and 1375C using 22.7 kg normal loads. SSN exhibited a strength loss compared to baseline after 1200C testing. However, the strength loss was due attributed to the effect of elevated temperature exposures on SSN discussed in Section 3.3.2.2 since no failures initiated from the line of contact. SSC did not exhibit any strength losses. Prior GTEC experience suggests the line contact line loads utilized should have exceeded the thresholds for damaging RBSN and SSC (no data base existed for SSN). However, all prior contact test experience with materials at
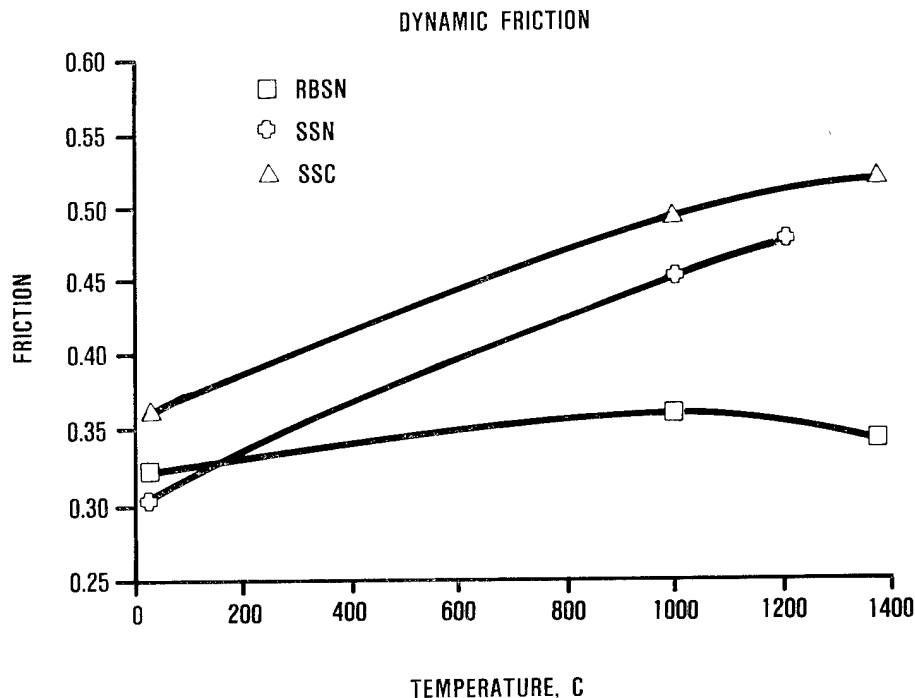
DYNAMIC FRICTION

Figure 46. The dynamic friction of RBSN, SSN, and SSC increased at elevated temperatures. The increase for RBSN was minor.

the loads of interest involved the use of a non-self-aligning contact test rig rather than the self-aligning rig used in the current program. The non-self-aligning system may have produced a concentrated contact load which is avoided in the self-aligning rig.

Point contact testing provided the higher contact stresses required to develop thresholds for RBSN and SSC at room and elevated temperatures. Threshold conditions were obtained for SSN at room temperature, but sufficient specimens were not available for obtaining elevated temperature thresholds. The results of the point contact tests are summarized in Table 16.

RBSN exhibited contact damage for all point contact tests.

SSN did not exhibit any contact damage up to 22.7 kg normal load. Therefore, the load range was extended at room temperature. At 27.2 kg, one of the three specimens tested exhibited contact damage and a strength loss of 40 percent. At 39.3 kg load, all specimens exhibited an average strength loss of 45 percent. At 45.4 kg, problems were encountered in testing. The end of the bottom load rod of the test rig contacted the upper load rod and shared some of the contact load applied. However, a 30 percent strength loss due to contact stress damage was still observed. Due to a limited quantity of SSN material, specimens were not available for additional elevated temperature testing at higher loads.

Table 16. Point contact test results*

Substrate	Temperature (C)	4.5	11.3	22.7	Load (kg) 27.2	39.3	45.4
RBSN	RT		-35%	-40%			
	1000			-45%			
	1375			-30%			
SSN	RT	ND+	ND	ND	-40%	-45%	-30%++
	1000	ND	ND	ND			
	1200	ND	ND	ND			
SSC	RT	ND	-12%	-30%			
	1000		ND	-30%			
	1375		ND	-35%			

*Numbers shown are average strength losses for specimens
  exhibiting contact damage.
+Not damaged; no contact damage was exhibited.
++Problem in testing at 45.4 kg resulted in a lower normal
  load on the specimen than applied.

SSC exhibited no contact damage for 4.5 kg load tests at room temperature. At 11.3 kg, one of three specimens was damaged and the strength loss was 12 percent. At 22.7 kg, all specimens exhibited contact damage at room temperature with an average strength loss of 30 percent. At 1000C, 22.7 kg loading caused damage on two of three SSC specimens; the average strength loss was 30 percent. Only one of three specimens exhibited contact damage at 1375C and 22.7 kg loading. The strength loss was 35 percent.

3.3.5 Coated Contact Testing

3.3.5.1 Coated Contact Test Procedures. Contact testing was conducted on coated specimens using procedures similar to those discussed in Section 3.3.4.1. The test matrices for coated contact testing are shown in Table 17. Preliminary contact tests (Table 17a) were conducted using both point and line contact. Three specimens from each system were evaluated. One specimen was used at each of the test temperatures and four tests were conducted per specimen. The preliminary test matrix provided friction characteristics under the same test conditions for all six coating/substrate systems.

The contact stress tests (Table 17b) were conducted using test conditions above the threshold for damaging the as-machined substrates (determined in uncoated contact tests). Therefore systems with different substrates were tested under different conditions. The contact stress test matrix utilized one specimen per test so that the coated

Table 17. Test matrix for coated contact testing

a. Preliminary friction tests

Temperature (C)	Line 22.7	Contact load (kg)		
		4.5	11.3	22.7
RT	1	1	1	1
1000	1	1	1	1
1375*	1	1	1	1

*SSN was tested at 1200C instead of 1375C.

b. Contact stress tests (point contact only)

Coating/Substrate System	Temperature (C)	Contact load (kg)		
		22.7	27.2	34.3
ZrO_2/CVD Al_2O_3/RBSN	RT	10		
and	1000	10		
ZRO_2/CVD Al_2O_3/RBSN	1375	5	5	
ZrO_2/sol-gel Al_2O_3/SSN	RT			10
and	1000			10
ZrO_2/laser-textured SSN	1200			10
ZrO_2/sol-gel Al_2O_3/SSN	RT	10		
and	1000	5	5	
ZrO_2/laser-textured SSN	1375	5	5	

specimens could be subsequently flexure tested for retained strength (Task 4).

3.3.5.2 Coated Contact Test Results. The coefficients of friction observed for the preliminary friction tests and contact stress tests are shown in Figures 47 and 48, respectively. The friction results from both test matrices agree. The static and dynamic friction coefficients were unexpectedly high. Previous studies on cubic stabilized zirconia (CSZ) and transformation toughened zirconia (TTZ) materials resulted in static and dynamic coefficients of friction less than 0.2 up to 1375C.[9,10] The high modulus SSC contact pin (e.g., 400 MPa) may deform the low modulus coating (e.g., 10 to 20 MPa) to create a plowing effect, which would increase the apparent room temperature friction.

The friction coefficients increased at elevated temperatures which is also uncharacteristic of zirconia. However, the contact pins used
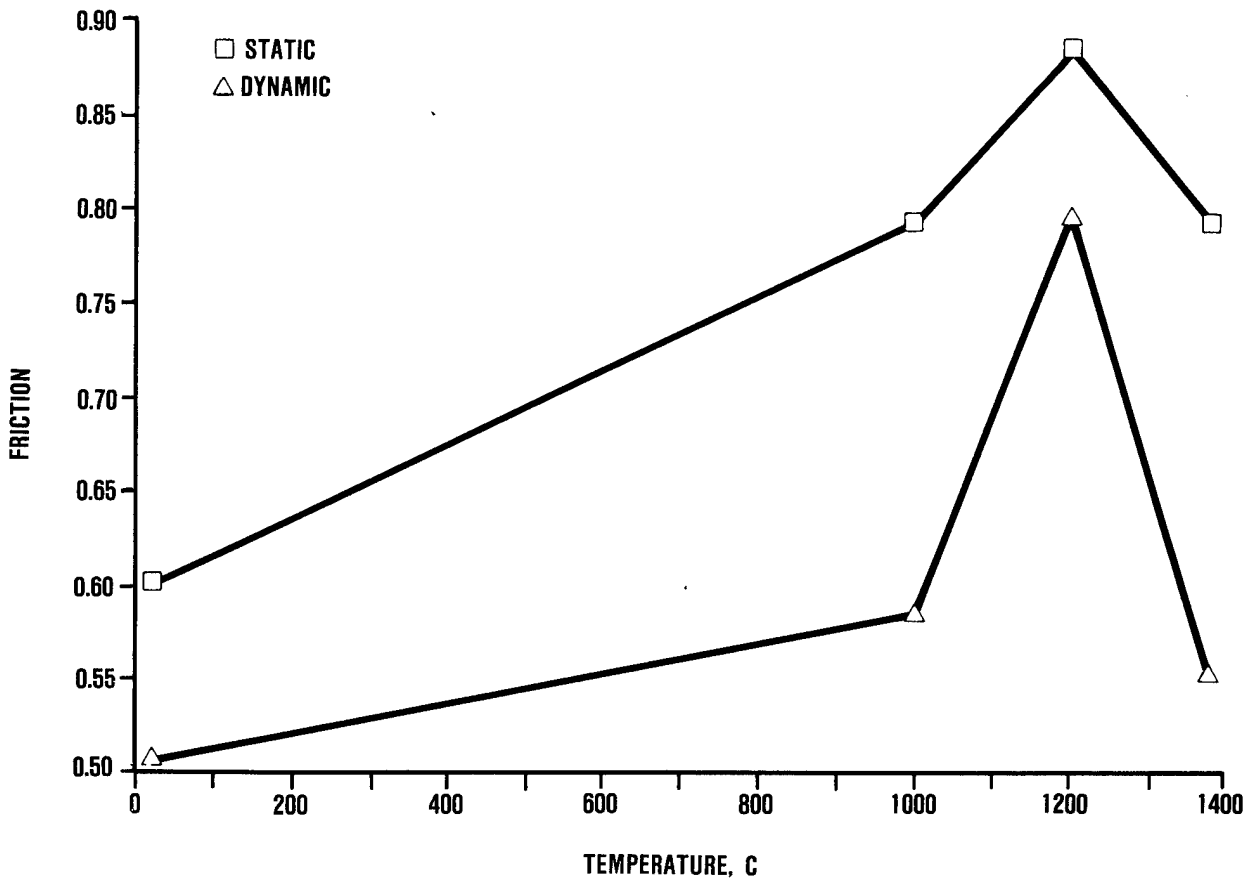
Figure 47. The EB-PVD ZrO$_2$ coatings exhibited high coefficients
of friction during preliminary friction tests.

were SSC, a silica former, whereas the early work on CSZ and TTZ used
contact pins of like material. Optical analysis of the contact region
showed the coating to be smeared and glassy after 1000C contact expo-
sure. As-discussed in Section 3.3, glass formation on the SSC contact
pin was anticipated as a potential problem since glass build-up was
observed on the ZrO$_2$ coating under the flexure load pins after 1375C
testing. Since coating failure occurred in all 1375C contact tests,
glass build up on the ZrO$_2$ coating could not be characterized. However,
glass formation may have contributed to frequent spalling observed at
1375C. Using a zirconia coated contact pin against the zirconia coated
specimen would probably yield more stable friction characteristics.

In many cases, the coating chipped or spalled during contact test-
ing, but the coating friction coefficients could be exuracted since the
spalling and chipping usually occurred after the point contact had tra-
versed a significant distrance. Some spalling occurred prior to the
initiation of sliding, and the static coefficient of friction measured
was actually the result of this spalling. After spalling, the dynamic
friction coefficient was for the SSC contact pin/substrate interface
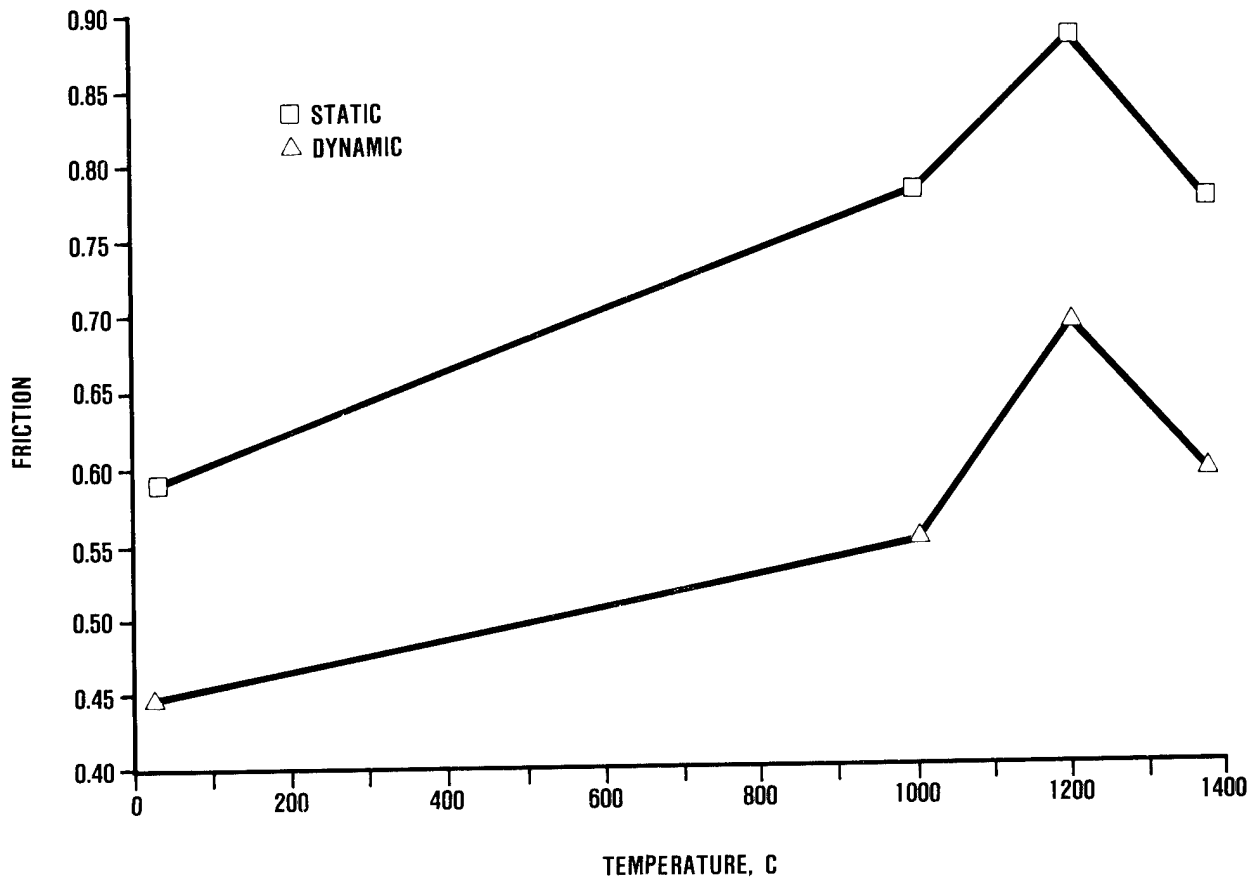
Figure 48. Friction results from contact stress tests were in
agreement with the preliminary friction test results.

since the ZrO$_2$ was no longer present. It should be pointed out that the
point contact conditions used in these contact stress tests are much
more severe than the line contact tests used to assess coating adherence
in previous tasks.

At room temperature, most systems exhibited chipping of the zir-
conia coating in the test zone. Laser-textured SSC performed the best
at room temperature (two specimens chipped) followed by CVD Al$_2$O$_3$/RBSN
(four chipped). The chipped areas of the laser-textured SSC still had
EB-PVD ZrO$_2$ in the surface cavities (Figure 49). Both the CVD AlN/RBSN
and laser-textured SSN had only a few survivors. Specimens from the
ZrO$_2$/sol-gel Al$_2$O$_3$/SSN and ZrO$_2$/sol-gel Al$_2$O$_3$/SSC systems all spalled.
The ZrO$_2$/sol-gel Al$_2$O$_3$/SSN system was the only system which exhibited
large area spalls. Laser-textured SSN, like laser-textured SSC, had
ZrO$_2$ still adhered in the surface cavities of spalled areas (Figure 50).

At 1000C most specimens exhibited better coating adherence. CVD
Al$_2$O$_3$/RBSN, CVD AlN/RBSN, and laser-textured SSC, no ZrO$_2$ spalling was
exhibited. Only two specimens each spalled for sol-gel Al$_2$O$_3$/SSN and

TEST DIRECTION →
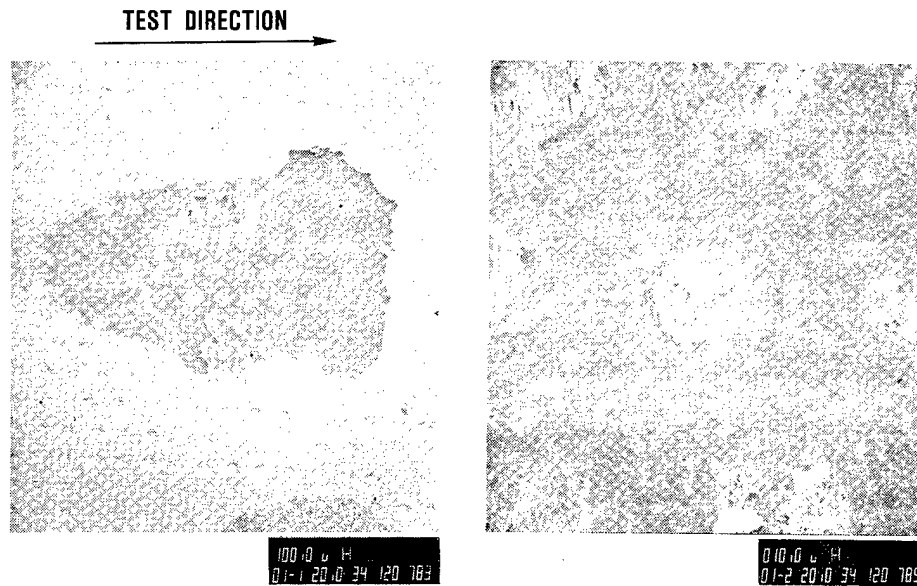
Figure 49. For laser-textured SSC, the EB-PVD ZrO$_2$ remained adherent adherent in the surface cavities even though the coating spalled on contact testing.

TEST DIRECTION →
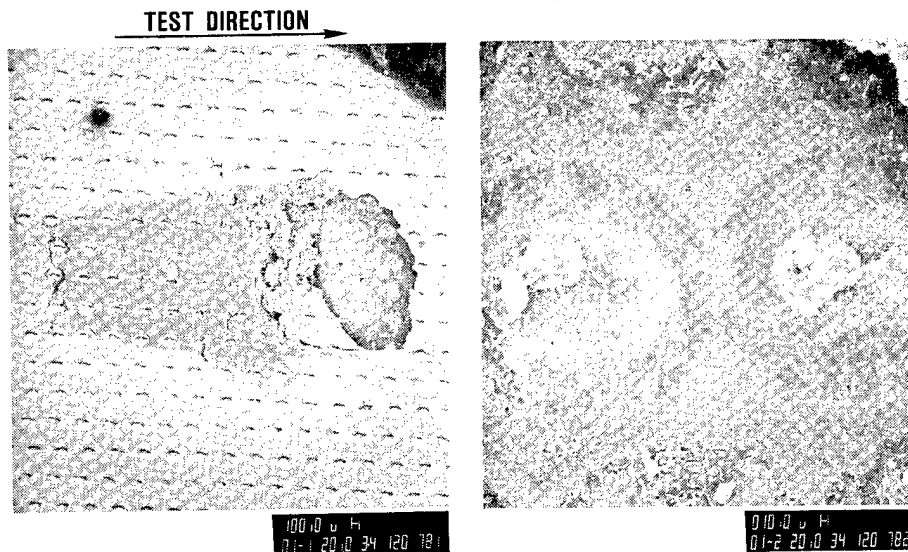
Figure 50. Like for laser-textured SSC, the EB-PVD ZrO$_2$ remained adherent in the surface cavities of the laser-textured SSN.

SSC. Laser-textured SSN spalled the most frequently (seven of ten spalled). The overall better adherence observed at 1000C may be due to relieving residual stresses at the interface near processing temperature (EB-PVD ZrO_2, CVD Al_2O_3, and CVD AlN were deposited near 1000C, and the sol-gel Al_2O_3 were calcined at 1000C).

Very few systems had specimens whose coating survived during 1200C or 1375C contact tests. The only survivors were three laser-textured SSN specimens tested at 1200C using 34.3 kg normal load.

3.3.6 Task 3 Summary and Conclusions

Strength Testing. The coating/substrate systems were flexure tested to determine the effect of pretreatment, coating, and heat treatment on substrate strength. ZrO_2/CVD Al_2O_3/RBSN and ZrO_2/CVD AlN/RBSN showed a strength loss at room temperature but regained the lost strength at elevated temperature. At 1375C, both systems exhibited higher than baseline strength. The results suggest that residual stresses may be effecting the strength of these systems.

ZrO_2/sol-gel Al_2O_3/SSN and ZrO_2/laser-textured SSN both exhibited strengths at room temperature and 1000C much lower than as-machined SSN. However, the strength loss was primarily due to the degradation of the SSN substrate during heat treatment since uncoated SSN exhibited a 27 percent strength loss after an exposure 1200C at 100 hours. At 1375C both systems exhibited creep deformation during testing and low strengths which was characteristic of SSN at that temperature.

The ZrO_2/sol-gel Al_2O_3/SSC and ZrO_2/laser-textured SSC systems exhibited no significant changes in strength. ZrO_2/sol-gel Al_2O_3/SSN exhibited no change in strength at room temperature and 1375C, and showed higher strength at 1000C which is believed to be coincidental. ZrO_2/laser-textured SSC exhibited a slight drop in strength at room temperature, but strengths equivalent to as-machined SSC at 1000C and 1375C.

Glass build-up occurred on the ZrO_2 coatings under the hot pressed SiC flexure load pins during testing at 1375C. This glass formation suggested there may be some sticking problems during the 1375C coated contact testing (SSC contact pins are to be used against the ZrO_2 coatings). To assess this problem, studies were conducted to evaluate the sticking resistance of EB-PVD ZrO_2 coatings). To assess this problem, studies were conducted to evaluate the sticking resistance of EB-PVD ZrO_2 against itself and the three substrate materials. The results suggested the ZrO_2 coating sticks to SiO_2 formers (e.g., Si_3N_4 and SiC) but not to itself. Therefore, in heat engine applications, both contacting surfaces may need to be coated to prevent sticking.

Cyclic Thermal Testing. Each coating/substrate system was subjected to cyclic thermal exposures to 1000C and 1375C to assess spalling resistance. The results were encouraging considering the large thermal expansion mismatch between the coating and the substrate. ZrO_2/CVD Al_2O_3/RBSN had the best spalling resistance as no specimens exhibited spalling. ZrO_2/laser-textured SSN and ZrO_2/laser-textured SSC performed

nearly as well; minor edge spalling occurred in some cases during 1000C testing. ZrO_2/CVD AlN/RBSN exhibited relatively good spalling resistance as only one of four spalled during 1375C tests. ZrO_2/sol-gel Al_2O_3/SSN and ZrO_2/sol-gel Al_2O_3/SSC exhibited poor spalling resistance as frequent spalling was observed.

Contact Testing. The contact damage resistance of RBSN, SSN, and SSC was significantly higher than originally thought. As a result, thresholds had to be established using point contact testing, rather than line contact testing. Contact damage was observed using point contact loads as low as 11.3 kg for RBSN and SSC. Contact damage occurred consistently using 22.7 kg point contact loads. SSN exhibited better contact damage resistance than RBSN and SSC. Loads of 27.2 kg were required to achieve conditions for damage. Contact damage was observed consistently using a 39.3 kg point contact load.

Coated specimens were also evaluated for friction characteristics during coated contact testing. Surprisingly, the ZrO_2 coatings had higher friction coefficients than the uncoated substrates and the coefficients of friction increased with temperature. The SSC contact pin may deform the low modulus coating to create a plowing effect, which would increase the apparent friction. Oxidation of the SSC contact pin may have caused the friction increase at elevated temperatures. The apparent room temperature friction may be reduced by depositing a dense layer over the porous coating to reduce the plowing effect; and the friction increase at elevated temperatures may be eliminated by using ZrO_2 coated contact pins so that two stable oxides are in contact.

The coating/substrate systems were more resistant to spalling at 1000C than at room temperature, 1200C, and 1375C. It appears that the residual stresses at the interface may be relieved near the coating deposition temperatures.

3.4 TASK 4 - POST-CONTACT STRENGTH TESTING

During Task 4, the specimens contact tested during Task 3 were flexure tested at room temperature to measure the retained strengths relative to the coated strengths generated under Task 3 (see Section 3.3.2.2, Table 18). Fractography was performed on each specimen to determine the nature of failure (i.e., contact versus noncontact failure).

3.4.1 Strength Test Procedures

The specimens subjected to contact stress conditions in Task 3 were flexure tested with the coated and contact tested side of the specimen in tension. The tests were conducted at room temperature using the test procedures described in Section 3.2.3. After flexure testing, all fracture surfaces were examined up to 40X magnification using an optical binocular microscope. Selected specimens were analyzed further using SEM and EDX analysis.

Table 18. Average retained strengths of contact tested specimens

		Retained strength (MPa)	
	Temperature (C)	Contact failures	Noncontact failures
ZrO_2/CVD Al_2O_3/RBSN	RT	(0)*	220
	1000	87 (2)	223
	1375	181 (1)	230
ZrO_2/CVD AlN/RBSN	RT	(0)	238
	1000	110 (2)	265
	1375	(0)	185
ZrO_2/sol-gel Al_2O_3/SSN	RT	(0)	370
	1000	(0)	393
	1200	325 (10)	–
ZrO_2/laser-textured SSN	RT	(0)	415
	1000	(0)	424
	1200	(0)	397
ZrO_2/sol-gel Al_2O_3/SSC	RT	(0)	291
	1000	180 (3)	288
	1375	(0)	287
ZrO_2/laser-textured SSC	RT	(0)	267
	1000	(0)	242
	1375	(0)	252

*Numbers in parenthesis indicate the number of specimens exhibiting contact damage.

3.4.2 Strength Test Results

The strength test results from contact tested specimens are shown in Table 18. No contact damage resulted from specimens tested at room temperature regardless of how well the coating held up during contact testing. In the cases where the coating chipped off the substrate, the chipping occurred at the onset of sliding or after the point contact had traversed a significant distance across the test specimen. Therefore, the contact pin was actually in contact with the bare substrate during dynamic (sliding) portion of the contact test exposure. In these cases, contact damage may have been prevented by avoiding the more severe static situations (typically, the static coefficients of friction were much higher). Where the coating chipped at the onset of sliding, the stress buildup during the static portion of the contact test where

relieved when the coating failed. In such cases, the friction coeffi-
cients actually increased after chipping. The increase was possibly
caused by asperity effects produced by debris from the coating increased
the apparent friction. It is possible that the presence of debris pro-
vided contact damage resistance.

For specimens tested at 1000C, the coatings prevented contact
stress damage in most cases, but some contact stress failures were
observed. For ZrO_2/CVD Al_2O_3/RBSN two of ten specimens exhibited con-
tact damage. The strength loss was to 87.2 MPa, a 59 percent drop.
Surprisingly, these were specimens which did not exhibit chipping of the
coating during contact testing. Two specimens from the ZrO_2/CVD AlN/
RBSN system also exhibited contact damage during 1000C contact testing.
Neither of these specimens exhibited spalling during contact testing
(all specimens from this system survived 1000C contact exposures). The
strength loss was to 110 MPa, a 53 percent drop in strenth. Three
specimens from the ZrO_2/sol-gel Al_2O_3/SSC system exhibited contact
damage during 1000C contact testing. The strength loss was to 180 MPa,
a 36 percent strength loss. In all cases, the coating remained adherent
during contact testing.

At 1200C all specimens from the ZrO_2/sol-gel Al_2O_3/SSN system
exhibited contact damage. As noted in Section 3.3.5.2, all ZrO_2/sol-gel
Al_2O_3/SSN specimens exhibited spalling during contact testing at 1200C.
The average strength loss was 15 percent relative the baseline, but
strength losses as high as 50 percent were observed. No ZrO_2/laser-
textured SSN specimens exhibited contact stress damage. All failure
origins were the surface cavities produced by the laser-texturing pre-
treatment.

At 1375C no contact damage was exhibited for ZrO_2/CVD AlN/RBSN,
ZrO_2/sol-gel Al_2O_3/SSC, and ZrO_2/laser-textured SSC. Only one specimen
exhibited contact damage for the ZrO_2/CVD Al_2O_3/RBSN system. The
resulting strength loss was 14 percent. ZrO_2/CVD AlN/RBSN did exhibit
some strength loss relative to baseline which did not result from con-
tact damage. Speculation is that the 1375C exposure may have caused
some degradation of the coating substrate interface.

3.4.3 Fractography

SEM and EDX analysis was performed on selected contact and strength
tested specimens to further characterize the failures.

As mentioned in the previous section, a few contact damage failures
did occur even though the coating remained adherent during contact test-
ing. This damage was observed for 1000C contact testing only. Figure
51 illustrates a contact flaw approximately 250 microns deep. This deep
crack was the most severe observed. In most cases, the crack was 25 to
75 microns deep. In all cases the failure origin was under the initial
contact point (i.e., where sliding was initiated). Evidently under cer-
tain conditioning, well adhered coatings can transmit damage to the sub-
strate.

Since the coatings were more adherent at 1000C (see Section
3.3.5.2), the specimens which did not exhibit contact stress damage may

ZrO$_2$/CVD Al$_2$O$_3$/RBSN (97 MPa)
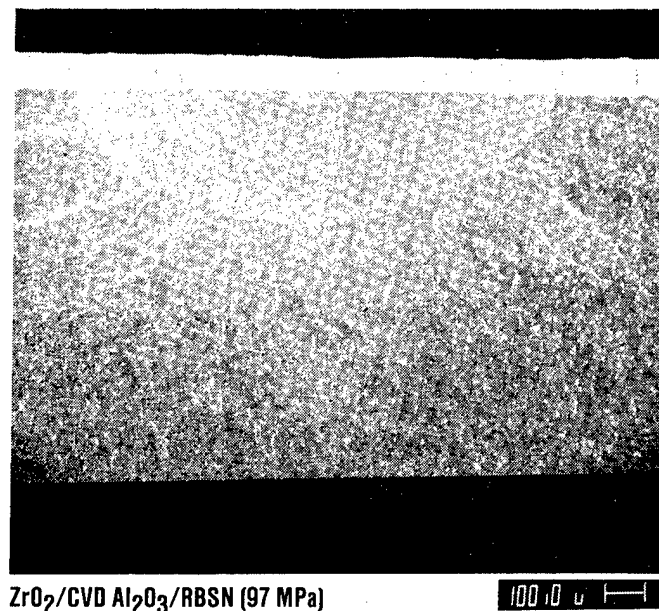
Figure 51. Contact damage occurred in a few cases for which the ZrO$_2$ coating remained adhered throughout contact testing.

have cracked at the interface or within the coating to relieve the contact stresses generated. At 1375C chipping occurred in all cases, and no contact damage occurred.

When coating chipping occurred, the only contact damage observed was at 1200C for the ZrO$_2$/sol-gel Al$_2$O$_3$/SSN system. All ten specimens contact tested at 1200C exhibited contact damage. The damage for one specimen appeared to be more of a slow crack growth effect due to softening of the grain boundary phases in the substrate. Figure 52 shows a large, wide crack located under contact test initiation point which resulted in a 50 percent strength loss. This crack evidently grew during the 30 minute normal loading of the 45.4 kg point contact and/or the point contact displacement. The contact damage observed for the other specimens appeared to be purely mechanical and resulted in a lesser strength loss averaging approximately 10 percent. ZrO$_2$/laser-textured SSN specimens were tested at 1200C under the same conditions, (i.e., 45.4 kg point contact loading) but did not exhibit any contact damage.

3.4.4 Task 4 Summary and Conclusions

The coatings successfully prevented contact damage during room temperature contact testing. However, the coatings were damaged during testing in most cases and, therefore, are not expected to provide contact damage resistance under cyclic loading conditions.

The ZrO$_2$ coatings exhibited better adherence at 1000C, spalling in only a few instances. Contact damage was prevented in most cases, but a few specimens did exhibit contact damage even though the coating remained adherent throughout testing. It appears the EB-PVD coating's

ZrO$_2$/SOL-GEL Al$_2$O$_3$/SSN

Figure 52. A large, wide crack in the SSN substrate resulting from
from contact stress damage caused a 50 percent strength loss.

columnar microstructure can transmit damage to the substrate under cer-
tain conditioning. The weakly adhered coatings appeared to protect the
substrate from contact damage sacrificially.

During 1200C and 1375C contact testing, contact damage was pre-
vented for all systems except the ZrO$_2$/sol-gel Al$_2$O$_3$/SSN system. All
specimens from this system spalled during 1200C and exhibited contact
damage. The undamaged systems also exhibited frequent spalling,
although the ZrO$_2$/laser-textured SSN had a few survivors at 1200C.

4.0   CONCLUSIONS

Conclusions related to the application and adherence, and to the strength, friction, and contact stress damage resistance are summarized below:

Application and Adherence

1.   The EB-PVD process can deposit controlled coatings of stabilized ZrO_2 with good to excellent adherence on 320 grit diamond ground surfaces of RBSN, SSN, and SSC. STEM and EDX results suggest that the bond interface is a zirconium silicate.

2.   Mechanical adherence contributes significantly to the overall adherence of EB-PVD ZrO_2 coatings. RBSN, which has the roughest surface of the substrate materials due to its 15 percent residual porosity, consistently exhibited better adherence than the dense SSN and SSC substrates. Also, lapping the 320 grit ground surfaces prior to coating resulted in poorer adherence in most cases.

3.   Roughening the substrate surface prior to applying the EB-PVD ZrO_2 coating improves the mechanical adherence. Laser-texturing of SSC and SSN substrates signifi-cantly improved the coating adherence both before and after oxidation without the use of an oxygen diffusion barrier.

4.   Oxidizing EB-PVD ZrO_2 coated RBSN, SSN, and SSC degrades the level of coating adherence significantly. The adherence degradation is due to the growth of the silicate layer at the interface. The high oxygen permeability of ZrO_2 allows oxygen transport to the coating/substrate which enables silicate growth at high temperatures.

5.   Depositing an oxygen diffusion barrier between the EB-PVD ZrO_2 coating and the Si_3N_4 or SiC substrate is a feasible approach for reducing or eliminating adherence degradation caused by interfacial oxidation.

6.   CVD Al_2O_3 and CVD AlN interlayers work well for the porous RBSN substrates but not for the dense SSN and SSC substrates. Apparently, thermal expansion mismatch between the dense interlayer and the substrate result in interfacial cracking, but the residual porosity in the RBSN enables islands of interlayer to remain adherent due to rooting into the substrate pores.

7.   Sol-gel Al_2O_3 interlayers are preferred for SSN and SSC substrates over CVD Al_2O_3 since relatively good adherence was retained after oxidation exposure. The 50 percent porous sol-gel interlayer (submicron sized porosity) evidently provides improved strain tolerance which limits interfacial cracking due to thermal expansion mismatch, but, at the cost of the cohesive strength of the interlayer.

Strength, Friction, and Contact Damage

8.   RBSN, SSN, and SSC exhibit significantly higher contact damage resistance than originally assumed.

9. EB-PVD Y_2O_3 stabilized ZrO_2 coatings increase the contact damage resistance of Si_3N_4 and SiC ceramics. However, the contact damage resistance provided appears to be sacrificial protection.

10. EB-PVD Y_2O_3 stabilized ZrO_2 coatings exhibit significantly higher coefficients of friction during contact testing than dense Y_2O_3 stabilized and transformation toughened ZrO_2. The high compliancy of the porous EB-PVD coating may allow the contact pin to imbed in the coating to create a plowing effect which increases the apparent friction.

11. EB-PVD Y_2O_3 stabilized ZrO_2 exhibits an increasing coefficient of friction with temperature when tested against SiC. This increase is probably due to the formation of SiO_2. EB-PVD ZrO_2 tested against itself, may not produce this increased friction. Compatibility studies at 1375C showed that a ZrO_2 coated specimen will stick severely to Si_3N_4 and SiC but will not stick to another ZrO_2 coated specimen. A suggestion for engine application of ZrO_2 coatings is that both mating surfaces of Si_3N_4 and/or SiC components should be coated to prevent sticking due to oxide formation.

12. Well bonded EB-PVD ZrO_2 coating can transmit damage to the substrate under certain conditions. Further work is needed to better understand this phenomenon and to prevent the damage transmittance.

13. Dense, strong interlayers may result in residual stress effects due to thermal expansion mismatch. During this program, CVD Al_2O_3 and CVD AlN interlayers reduced the room temperature strength of the substrate, but the strength recovered at elevated temperature. In future studies more emphasis should be placed on minimizing thermal expansion mismatches in order to minimize residual stress effects.

14. Laser-texturing can reduce the room temperature strength of Si_3N_4 and SiC substrates, although the strength is recovered at elevated temperatures. Microcracks extending from the laser produced cavities limit substrate strength. Further research is required on laser-texturing of Si_3N_4 and SiC to minimize the resulting strength losses.

REFERENCES

1. <u>Advanced Gas Turbine (AGT) Powertrain System Development for Automotive Applications, second Semiannual Progress Report</u>, Contract No. CR-165329, GTEC Report No. 31-3725(2), July 1981.

2. D.W. Richerson and K.M. Johansen, <u>Ceramic Gas Turbine Engine Demonstration Program, Final Report</u>, DARPA Contract N00024-76-C5352, May 1982, GTEC Report 21-4410.

3. J.M. Criscione, S. Sarian, H.F. Volk, et al., <u>High Temperature Protective Coatings for Graphite, Summary Technical Report for Work Conducted 1 June 1963 to 31 May 1964</u>, from ML-TDR-64-173, Part II, 1964.

4. Personal communication with Dr. A.G. Evans of the University of California, Berkeley, and Daniel Lee of Temescal, Berkeley, CA, during program coordination meeting held September 12, 1984, in Berkeley, CA.

5. <u>Highly Reliable High Performance Thermal Barrier Coatings (TBC), Technical Proposal</u>, GTEC Report 21-5132-2, August 23, 1984.

6. Unreported research conducted jointly by GTEC and Special Processes of Arizona in 1980.

7. D.W. Richerson, W.D. Carruthers, L.J. Lindberg, "Contact Stress and Coefficient of Friction Effects on Ceramic Interfaces," Surfaces and Interfaces in Ceramic and Ceramic Metal Systems, <u>Materials Science Research</u>, Volume 14, pp. 661-676. Edited by Joseph Pask and Anthorny Evans, Plenum Press, NY 1981.

8. J.R. Smyth, D.W. Richerson, "High Temperature Dynamic-Contact Behavior of Sintered Alpha Silicon Carbide," <u>Ceramic Engineering and Science Proceedings</u>, Vol. 4, No. 7-8, 1983, pp. 663-673.

9. L.J. Lindberg and D.W. Richerson, "Comparison of the Contact Stress and Friction Behavior of SiC and ZrO_2 Materials," <u>Ceramic Engineering and Science Proceedings</u>, Vol. 6, No. 7-8, 1985, pp. 1059-1066.

10. L.J. Lindberg, <u>Contact Stress and Frictional Behavior of Three Commercially Available Transformation Toughened Zirconia Materials</u>, Masters Thesis, Arizona State University, 1984.

INTERNAL DISTRIBUTION

1-2.	Central Research Library	34-38.	D. R. Johnson
3.	Document Reference Section	39.	R. R. Judkins
4-5.	Laboratory Records Department	40.	M. A. Karnitz
6.	Laboratory Records, ORNL RC	41.	M. P. Kertesz
7.	ORNL Patent Section	42.	T. B. Lindemer
8.	S. Baik	43.	K. C. Liu
9.	R. L. Beatty	44.	E. L. Long, Jr.
10.	P. F. Becher	45.	W. D. Manly
11.	J. Bentley	46	R. W. McClung
12.	T. M. Besmann	47.	D. L. McElroy
13.	A. Bleier	48.	A. J. Moorhead
14.	E. E. Bloom	49.	J. L. Rich
15.	K. W. Boling	50.	C. R. Richmond
16.	W. D. Bond	51.	J M Robbins
17.	R. A. Bradley	52.	M. W. Rosenthal
18.	C. R. Brinkman	53.	M. L. Santella
19.	V. R. Bullington	54-77.	A. C. Schaffhauser
20.	A. J. Caputo	78.	J. H. Schneibel
21.	R. S. Carlsmith	79.	J. L. Scott
22.	P. T. Carlson	80.	G. M. Slaughter
23.	J. A. Carpenter, Jr.	81.	E. J. Soderstrom
24.	J. V. Cathcart	82.	D. P. Stinton
25.	R. H. Cooper	83.	R. W. Swindeman
26.	S. A. David	84.	V. J. Tennery
27.	J. H. DeVan	85-87.	P. T. Thornton
28.	W. P. Eatherly	88.	T. N. Tiegs
29.	J. I. Federer	89.	J. R. Weir, Jr.
30.	W. Fulkerson	90.	F. W. Wiffen
31.	R. L. Graves	91.	R. K. Williams
32.	D. L. Greene	92.	C. S. Yust
33.	M. A. Janney	93.	A. Zucker

EXTERNAL DISTRIBUTION

94. Donald F. Adams
Composite Materials Research Group
Mechanical Engineering Department
University of Wyoming
Laramie, WY 82071

95. Jane W. Adams
Corning Glass Works
SP-DV-21
Corning, NY 14831

96. Donald J. Adrian
Chief Engineer
High Velocity Tool Corp.
2015 Indiana Street
Racine, WI 53405

97. Bruce J. Agle
Metallurgical Engineer
Sundstrand Corporation
Turbomach Division
Advanced Technology Group
4400 Ruffin Road
PO Box 85757
San Diego, CA 92138-5757

98. Richard T. Alpaugh
Department of Energy
Office of Transportation
    Systems
Forrestal Building CE-151
1000 Independence Avenue
Washington, DC 20585

99. H. Arbabi
Brunel University
Department of Materials
    Technology
Uxbridge Middlesex UB8 3PH
United Kingdom

100. James P. Arnold
U.S. Army Belvoir
R&D Center
ATTN: FTRBE-EMP
Fort Belvoir, VA 22060

101. V. S. Avva
North Carolina Agricultural and
    Technical State University
Department of Mechanical
    Engineering
Greensboro, NC 27411

102. John M. Bailey
Research Consultant
    Research Dept.
Technical Center
Caterpillar Tractor Company
100 NE Adams
Peoria, IL 61629

103. Murray Bailey
NASA Lewis Research Center
21000 Brookpark Road, MS 77-6
Cleveland, OH 44135

104. R. R. Baker
Ceradyne, Inc.
3030-A S. Red Hill Avenue
Santa Ana, CA 92705

105. J. Gary Baldoni
GTE Laboratories, Inc.
40 Sylvan Road
Waltham, MA 02254

106. Ken Baumert
Air Products and Chemicals,
    Inc.
Box 538
Allentown, PA 18105

107. A. L. Bement, Jr.
Vice President
Technical Resources
TRW, Inc.
23555 Euclid Avenue
Cleveland, OH 44117

108. M. Bentele
Xamag, Inc.
259 Melville Avenue
Fairfield, CT 06430

109. Clifton G. Bergeron
Head, Department of
    Ceramic Engineering
University of Illinois
204 Ceramics Building
Urbana, IL 61801

110. William D. Bjorndahl
TRW, Inc.
TRW Energy Development Group
Materials Characterization
    and Chemical Analysis Dept
One Space Park
Building 01, Room 2060
Redondo Beach, CA 90278

111. James A. Black
Vice President
American Matrix, Inc.
118 Sherlake Drive
Knoxville, TN 37922

112. John Blum
Norton Company
High Performance Ceramics
Goddard Road
Northboro, MA 01532-1545

113. Paul N. Blumberg
President
Integral Technologies Inc.
415 E. Plaza Drive
Westmont, IL 60559

114. Wolfgang D. G. Boecker
Sohio Engineered Materials
Company
Niagara Falls R&D Center
PO Box 832
Niagara Falls, NY 14302

115. Tibor Bornemisza
Sundstrand Corporation
Project Engineer,
Turbomach Division
Advanced Technology Group
4400 Ruffin Road, PO Box 85757
San Diego, CA 92138-5757

116. Seymour A. Bortz
Manager, Nonmetallic Materials
and Composites
Materials and Manufacturing
Technology
10 West 35th Street
Chicago, IL 60616

117. H. K. Bowen
Department of Materials Science
and Engineering, Room 12-009
Massachusetts Institute of
Technology
Cambridge, MA 02139

118. Richard C. Bradt
Chairman, Materials Science and
Engineering
University of Washington
Dept. of Materials Science and
Engineering
Roberts Hall, FB-10
Seattle, WA 98195

119. Raymond J. Bratton
Manager, Ceramic Science
Westinghouse Electric Corporation
R&D Center
1310 Beulah Road
Pittsburgh, PA 15235

120. Catherine E. Brown
E. I. DuPont de Nemours &
Company
Experimental Station
Information Center E302/301
Wilmington, DE 19898

121. J. J. Brown
Virginia Polytechnic
Institute and State
University
Department of Materials
Engineering
Blacksburg, VA 24061

122. W. Bryzik
U.S. Army Tank Automotive
Command
R&D Center, Propulsion
Systems Division
Warren, MI 48090

123. S. T. Buljan
GTE Laboratories Inc.
40 Sylvan Road
Waltham, MA 02254

124. John M. Byrne, Jr.
Manager, Busines
Development Co
Development Department
PPG Industries, Inc.
One PPG Place
Pittsburgh, PA 15272

125. Donald J. Campbell
Air Force Wright
Aeronautical Laboratory
AFWAL/POX
Wright-Patterson Air Force
Base
OH 45433

126. Harry W. Carpenter
Rockwell International
Rocketdyne Division
J39-169-FB39
6633 Canoga Avenue
Canoga Park, CA 91304

127. David Carruthers
Garrett Turbine Engine
  Company
111 South 34 Street
PO Box 5217
Phoenix, AZ 85010

128. Se-Tak Chang
GTE Laboratories
40 Sylvan Road
Dept. 312
Waltham, MA 02254

129. R. J. Charles, Manager
Ceramics Branch
Physical Chemistry
  Laboratory
General Electric Company
PO Box 8
Schenectady, NY 12301

130. En-sheng Chen
B&C Engineering Research
13906 Dentwood Drive
Houston, TX 77014

131. Albert A. Chesnes
Director, Heat Engine
  Propulsion Division
Office of Transportation Systems
Department of Energy
Forrestal Building CE-151
1000 Independence Avenue
Washington, DC 20585

132. Frank Childs
EG&G, Inc.
Idaho National Engineering
  Laboratory
PO Box 1625
Idaho Falls, ID 83415

133. Gilbert Y. Chin
Bell Telephone Laboratories
Research & Development
Murray Hill, NJ 07974

134. Melvin H. Chiogioji
Director, Office of
  Transportation Systems
Department of Energy
Forrestal Building CE-15
1000 Independence Avenue, SW
Washington, DC 20585

135. William J. Chmura
The Torrington Company
Corporate Research
59 Field Street
Torrington, CT 06790

136. Eugene V. Clark
Vice President
Technology Engineering
Turbine Metal Technology,
  Inc.
7327 Elmo Street
Tujunga, CA 91042-2204

137. William L. Cleary
Associate Division Director
ORI, Inc.
1375 Piccard Drive
Rockville, MD 20850

138. Jack L. Clem
General Manager
Carbon Black Division
Huber Technology Group
J. M. Huber Corporation
PO Box 2831
Borger, TX 79008-2831

139. Philip R. Compton
Energy Systems Office
National Aeronautics and
  Space Administration
Code REC-1
Washington, DC 20546

140. Harry E. Cook
Director, Automotive
  Research and Technical
  Planning
Chrysler Corporation
PO Box 857, CIMS:
  44-01-22
Detroit, MI 48288

141. Stephen Copley
Professor and Chairman
Materials Science
  Deapartment
University of Southern
  California
Los Angeles, CA 90089-0241

142. John A. Coppola
    Manager, Advanced Programs
    Structural Ceramics
      Division
    Standard Oil Engineered
      Materials Company
    PO Box 1054
    Niagara Falls, NY 14302

143. William J. Croft
    U.S. Army Materials
      Technology Laboratory
    Arsenal Street
    Watertown, MA 02172

144. Gary M. Crosbie
    Ford Motor Company
    PO Box 2053, Room S-2079
    Ceramics Materials Department
    Dearborn, MI 48121

145. Floyd W. Crouse, Jr.
    Department of Energy
    Morgantown Energy Technology
      Center
    PO Box 880
    Morgantown, WV 26505

146. Raymond Cutler
    Ceramatec, Inc.
    163 W. 1700 South
    Salt Lake City, UT 84115

147. David A. Dalman
    Research Manager
    Central Research
    Organic Specialties Lab
    Dow Chemical Company
    M. E. Pruitt Building
    Midland, MI 48640

148. Stephen C. Danforth
    Rutgers University
    PO Box 909
    Piscataway, NJ 08854

149. Stanley J. Dapkunas
    Ceramic Division
    Institute for Materials Science
      and Engineering
    National Bureau of Standards
    Gaithersburg, MD 20899

150. Robert F. Davis
    North Carolina State
      University
    Materials Engineering
      Department
    232 Riddick Laboratory
    Raleigh, NC 27607

151. Evelyn M. DeLiso
    Assistant Research Professor
      Center for Ceramics Research
    Rutgers University
    College of Engineering
    PO Box 909
    Piscataway, NJ 08854

152. Alan L. Dragoo
    Materials Scientist
      Inorganic Materials
      Division
    National Bureau of Standards
    Center for Materials Science
    Gaithersburg, MD 20899

153. Keith F. Dufrane
    Battelle Columbus
      Laboratories
    505 King Avenue
    Columbus, OH 43201

154. Robert J. Eagan
    Manager, Chemistry and
      Ceramics Department 1840
    Sandia National Laboratories
    Albuquerque, NM 87185

155. Christopher A. Ebel
    Program Manager
    High Performance Ceramics
    Norton Company
    Goddard Road
    Northboro, MA 01532

156. J. J. Eberhardt
    Director, Energy Conversion
      and Utilization
      Technologies Program
    Department of Energy
    Forrestal Building CE-12
    1000 Independence Ave SW
    Washington, DC 20585

157. E. E. Ecklund
Office of Transportation
Systems
Department of Energy
Forrestal Building CE-151
1000 Independence Avenue
Washington, DC 20585

158. William A. Ellingson
Argonne National Laboratory
9700 South Cass Avenue
Argonne, IL 60439

159. Director, Applied Technology
Laboratory
U.S. Army Research and Technology
Laboratory (AVSCOM)
ATTN: SAVDL-ATL-ATP
(Mr. Graydon A. Elliott)
Fort Eustis, VA 23604

160. A. Erdely
Chemical Engineer
26 Av. Gare des Eaux-vives
1208 Geneva
Switzerland

161. Charles D. Estes
U.S. Senate
Professional Staff Member
Committee on Appropriations
SD-152 Dirksen Senate Office
Building
Washington, DC 20510

162. Anthony G. Evans
University of California
College of Engineering
Santa Barbara, CA 93106

163. Robert C. Evans
Asst. Manager, Vehicular Gas
Turbine and Diesel Project
Office
NASA Lewis Research Center
21000 Brookpark Road
Cleveland, OH 44135

164. Katherine T. Faber
Assistant Professor of Ceramic
Engineering
Ohio State University
2041 College Road
Columbus, OH 43210

165. John Facey
National Aeronautics and
Space Administration
Energy Systems Office
Washington, DC 20546

166. John W. Fairbanks
Office of Transportation
Systems
Department of Energy
Forrestal Building CE-151
Washington, DC 20585

167. Larry Farrell
Babcock and Wilcox
PO Box 1260
Lynchburg, VA 24505

168. M. K. Ferber
University of Illinois
105 S. Goodwin Avenue
203 Ceramic Building
Urbana, IL 61801

169. H. W. Foglesong
Dow Corning Corporation
3901 S. Saginaw Road
Midland, MI 48640

170. Thomas F. Foltz
Manager, Product
Applications
Avco
Special Materials Division
Two Industrial Avenue
Lowell, MA 01851

171. Robert G. Frank
Manager, Non-Metallic
Materials
General Electric Company
One Neumann Way
Mail Drop M-87
PO Box 156301
Cincinnati, OH 45215-6301

172. Frank Gac
Los Alamos National
Laboratory
PO Box 1663
MSP6 MS G-770
Los Alamos, NM 87545

173. George E. Gazza
U.S. Army Materials
Technology Laboratory
Ceramics Research Division
Arsenal Street
Watertown, MA 02172

174. Charles M. Gilmore
Department of Civil, Mechanical,
and Environmental Engineering
The George Washington University
Washington, DC 20052

175. Paul Glance
Director, R&D
Concept Analysis Corporation
9145 General Court
Plymouth, MI 48170

176. Fred M. Glaser
Department of Energy
Office of Fossil Energy, FE-14
Washington, DC 20545

177. Joseph W. Glatz
Naval Air Propulsion Test Center
Science and Technology Group
Systems Technology Division
Box 7176, PE 34
Trenton, NJ 08628

178. Stephen T. Gonczy
Allied Signal Research Center
Materials Science Department
50 UOP Plaza
Des Plaines, IL 60016-6187

179. Robert J. Gottschall
Office of Material Sciences
Department of Energy
ER-131 GTN
Washington, DC 20545

180. Kenneth Green
Senior Development Engineer
Coors Porcelain Company
Golden, CO 80401

181. Michael Greenfield
National Aeronautics and
Space Administration
Energy Systems Office
Washington, DC 20546

182. Lance E. Groseclose
General Motors Corporation
Allison Gas Turbine Division
Indianapolis, IN 46206-0420

183. T. D. Gulden
Manager, Ceramics and
Chemistry
GA Technologies, Inc.
PO Box 81608
San Diego, CA 92138

184. M. D. Gurney
NIPER
PO Box 2128
Bartlesville, OK 74005

185. J. J. Habeeb
Senior Chemist
Research Division
Esso Petroleum Canada
PO Box 3022
Sarina, Ontario
Canada N7T 7M1

186. H. T. Hahn
Pennsylvania State
University
ESM Department
227 Hammond Building
University Park, PA 16802

187. Nabil S. Hakim
Staff Research Engineer,
Engineering R&D
General Motors Corporation
Detroit Diesel Allison
Division
36880 Ecorse Road
Romulus, MI 48174

188. John W. Halloran
Ceramic Process Systems
128 Spring Street
Lexington, MA 02173

189. R. A. Harmon
25 Schalren Drive
Latham, NY 12110

190. Stephen D. Hartline
     Norton Company
     High Performance Ceramics
     Goddard Road
     Northboro, MA 01532

191. Willard E. Hauth
     Section Manager, Composite
         Development Ceramics Program
     Dow Corning Corporation
     Midland, MI 48640

192. Norman L. Hecht
     University of Dayton Research
         Institute
     300 College Park
     Dayton, OH 45469-0001

193. S. S. Hecker
     Deputy Division Leader
     Material Science and Technology
         Division, G-756
     Los Alamos National Laboratory
     PO Box 1663
     Los Alamos, NM 87545

194. Peter W. Heitman
     General Motors Corporation
     Allison Gas Turbine Operation
     PO Box 420, W-5
     Indianapolis, IN 46206-0420

195. Richard L. Helferich
     The Duriron Company, Inc.
     PO Box 1145
     Dayton, OH 45401

196. H. E. Helms
     General Motors Corporation
     Allison Gas Turbine Operations
     PO Box 420
     Indianapolis, IN 46206-0420

197. Thomas L. Henson
     Director of Research and
         Engineering
     Chemical & Metallurgical
         Division
     GTE Products Corporation
     Hawes Street
     Towanda, PA 18848-0504

198. Thomas P. Herbell
     NASA Lewis Research Center
     21000 Brookpark Road
     MS 105-1
     Cleveland, OH 44135

199. Ben Heshmatpour
     Thermo Electron Corporation
     101 First Avenue
     Waltham, MA 02154

200. Hendrik Heystek
     Bureau of Mines
     Tuscaloosa Research Center
     PO Box L
     University, AL 35486

201. Robert V. Hillery
     Manager, Coating Materials
         and Processes
     General Electric Company
     Cincinnati, OH 45215

202. Jonathan W. Hinton
     Vice President and
         General Manager
     Structural Ceramics
         Division
     Standard Oil Engineered
         Materials
     PO Box 1054
     Niagara Falls, NY 14302

203. Stephen M. Hsu
     Chief, Ceramics Division
     Institute for Materials
         Science & Engineering
     National Bureau of Standards
     Gaithersburg, MD 20899

204. Harold A. Huckins, President
     Princeton Advanced
         Technology, Inc.
     56 Finley Road
     Princeton, NJ 08540

205. Joseph E. Hunter, Jr.
General Motors Corporation
Research Labs, Metallurgy
  Department
12 Mile and Mound Roads
Warren, MI 48090-9055

206. Louis C. Ianniello
Director, Office of Materials
  Sciences
Department of Energy
ER-13 GTN
Washington, DC 20545

207. Robert H. Insley
Champion Spark Plug Company
Ceramic Division
20000 Conner Avenue
Detroit, MI 48234

208. Curt A. Johnson
General Electric Company
Ceramics Branch
Physical Chemistry
  Laboratory
PO Box 8
Schenectady, NY 12301

209. Douglas C. Johnson
Technology Development Manager
Sundstrand Corporation
Turbomach Division
4400 Ruffin Road, PO Box 85757
San Diego, CA 92138-5757

210. Larry Johnson, Director
Center for Transportation Research
Argonne National Laboratory
9700 S. Cass Avenue, Building 362
Argonne, IL 60439

211. R. A. Johnson
General Motors Corporation
Allison Gas Turbine Division
PO Box 420
Indianapolis, IN 46206-0420

212. L. A. Joo
Associate Director of Research
Great Lakes Research Corporation
PO Box 1031
Elizabethton, TN 37643

213. A. David Joseph
Vice President, R&D Engineering
Sealed Power Corporation
100 Terrace Plaza
Muskegon, MI 49443

214. Roy Kamo, President
Adiabatics, Inc.
630 S. Mapleton
Columbus, IN 47201

215. Allan Katz
Air Force Wright
  Aeronautical Laboratory
Materials Laboratory,
  AFWAL/MLLM
Metals and Ceramics Division
Wright-Patterson Air Force Base
  OH 45433

216. R. N. Katz
Chief, Ceramics Research
  Division
U.S. Army Materials
  Technology Laboratory
Arsenal Street
Watertown, MA 02172

217. P. Victor Kelsey
Ceramics Technical Leader
Materials Science Division
Aluminum Company of America
Alcoa Technical Center B
Alcoa Center, PA 15061

218. Frederick L. Kennard, III
Supervisor, Ceramic Research
General Motors Corporation
AC Spark Plug Division,
  Dept. 32-24
1300 N. Dort Highway
Flint, MI 48556

219. J. R. Kidwell
AGT101 Assistant Project
  Engineer
Garrett Turbine Engine Company
111 S. 34th Street
PO Box 5217
Phoenix, AZ 85010

220. Max Klein
Senior Scientist, Thermodynamics
Gas Research Institute
8600 West Bryn Mawr Avenue
Chicago, IL 60631

221. C. E. Knapp
Norton Company
8001 Daly Street
Niagara Falls, Ontario
Canada

222. A. S. Kobayashi
University of Washington
Dept. of Mechanical Engineering
MS FU10
Seattle, WA 98195

223. James F. Kolbe
Group Vice President
Product Development and
   Engineering Services Group
Sealed Power Corporation
100 Terrace Plaza
Muskegon, MI 49443

224. David M. Kotchick
AiResearch Manufacturing Company
2525 W. 190th Street
Torrance, CA 90509

225. Bruce Kramer
George Washington University
Aerodynamic Center, Room T715
Washington, DC 20052

226. Saunders B. Kramer
Manager, AGT Program
Office of Transportation Systems
Department of Energy
Forrestal Building CE-151
1000 Independence Avenue
Washington, DC 20585

227. D. M. Kreiner
AGT101 Project Manager
Garrett Turbine Engine Company
111 S. 34th Street, PO Box 5217
Phoenix, AZ 85010

228. Pieter Krijgsman
Ceramic Design Int.
   Hold., Ltd.
PO Box 68
8050 AB Hattem
The Netherlands

229. W. J. Lackey
Georgia Tech Research
   Institute
Energy and Materials
   Sciences Laboratory
Georgia Institute of
   Technology
Atlanta, GA 30332

230. Everett A. Lake
Air Force Wright
   Aeronautical Laboratory
AFWAL/POOS
Wright-Patterson AFB
OH 45433

231. Fred F. Lange
University of California
College of Engineering
Santa Barbara, CA 93109

232. James Lankford
Department of Materials
   Sciences
Southwest Research Institute
6220 Culebra Road
PO Drawer 28510
San Antonio, TX 78284

233. John G. Lanning
Corning Glass Works
Advanced Engine Components
HP-BB-2
Corning, NY 14830

234. David C. Larsen
Corning Glass Works
Materials Research
   Department
Sullivan Park, FR-51
Corning, NY 14831

235. Patrick Lauzon
Ontario Research Foundation
Glass and Ceramics Centre
Materials Division
Sheridan Park Research
   Community
Mississauga, Ontario
Canada L5K 1B3

236. Harry A. Lawler
Senior Product Specialist
Structural Ceramics Division
Standard Oil Engineered
   Materials Company
PO Box 1054, Bldg. 91-2
Niagara Falls, NY 14302

237. Alan Lawley
Drexel University
Materials Engineering
Philadelphia, PA 19104

238. Daniel Lee
2850 7th Street
Berkeley, CA 94710

239. June-Gunn Lee
Head, Refractory Materials
   Laboratory
Korea Advanced Institute of
   Science and Technology
PO Box 131, Dong Dae Mun
Seoul
Korea

240. E. M. Lenoe
Office of Naval Research
Air Force Office of
   Scientific Research
Liaison Office, Far East
APO San Francisco, CA 96503-0110

241. Stanley R. Levine
NASA Lewis Research Center
21000 Brookpark Road
Cleveland, OH 44135

242. David Lewis
Naval Research Laboratory
Code 6360, Materials Science
   and Technology Division
4555 Overlook Avenue, SW
Washington, DC 20375

243. Winston W. Liang
Director of Program
   Development
Amercom, Inc.
8948 Fullbright Avenue
Chatsworth, GA 91311

244. Bill Long
Babcock and Wilcox
PO Box 1260
Lynchburg, VA 24505

245. L. A. Lott
EG&G, Inc.
Idaho National Engineering
   Laboratory
PO Box 1625
Idaho Falls, ID 83415

246. Bryan K. Luftglass
Staff Consultant
Chem Systems, Inc.
303 S. Broadway
Tarrytown, NY 10591

247. Michael J. Lynch
General Electric Company
Medical Systems Group
PO Box 414, 7B-36
Milwaukee, WI 53201

248. Vincent L. Magnotta
Senior Principal Development
   Engineer
Technical Diversification
   R&D Dept.
Air Products and Chemicals,
   Inc.
PO Box 538
Allentown, PA 18105

249. Tai-il Mah
Technical Manager, Ceramics
   and Composites Research
Universal Energy Systems
4401 Dayton-Xenia Road
Dayton, OH 45432

250. L. Manes
Material Scientist
Division of Prospective
  Studies and Knowledge
  Transfer
Commission of the European
  Communities
Joint Research Centre
Ispra Establishment
1-21020 Ispra (Varese)
Italy

251. Gerald R. Martin
Manager, Technology
Fleetguard, Inc.
Cookeville, TN 38501

252. John Mason
Vice President, Engineering
The Garrett Corporation
9851 Sepulveda Boulevard
PO Box 92248
Los Angeles, CA 90009

253. J. McCauley
U.S. Army Materials Technology
  Laboratory
DRXMR-MC
Arsenal Street
Watertown, MA 02172

254. Robert R. McDonald
President
Boride Products
2879 Aero Park Drive
Traverse City, MI 49684

255. William J. McDonough
Department of Energy
Office of Transportation Systems
Forrestal Building CE-151
1000 Independence Avenue
Washington, DC 20585

256. Thomas D. McGee
Iowa State University
Department of Materials Science
  and Engineering
Ames, IA 50011

257. Malcolm G. McLaren
Head, Department of Ceramics
Rutgers University
Busch Campus
Bowser Road, Box 909
Piscataway, NJ 08854

258. Arthur F. McLean
Manager, Ceramics Materials
  Department
Ford Motor Company
20000 Rotunda Drive
Dearborn, MI 48121

259. Brian L. Mehosky
Development Engineer, R&D
Standard Oil Engineered
  Materials
4440 Warrensville Center Rd.
Cleveland, OH 44128

260. P. K. Mehrotra
Kennametal, Inc.
PO Box 639
Greensburg, PA 15601

261. Joseph J. Meindl
Reynolds International, Inc.
PO Box 27002
6603 W. Broad St.
Richmond, VA 23261

262. D. Messier
U.S. Army Materials
  Technology Laboratory
DRXMR-MC
Arsenal Street
Watertown, MA 02172

263. Arthur G. Metcalfe
Director
Research Department
Solar Turbines, Inc.
2200 Pacific Highway
PO Box 80966
San Diego, CA 92138

264. Thomas N. Meyer
Senior Technical Specialist
Alumina, Chemicals and
  Ceramics Division
Aluminum Company of America
Alcoa Technical Center
Alcoa Center, PA 15069

265. W. Miloscia
      Standard Oil Engineered
         Materials
      Research and Development
      4440 Warrensville Center Rd.
      Cleveland, OH 44128

266. Bill Moehle
      Ethyl Corporation
      451 Florida Blvd.
      Ethyl Tower
      Baton Rouge, LA 70801

267. Helen Moeller
      Babcock and Wilcox
      PO Box 11165
      Lynchburg, VA 24506

268. Thomas Morel
      Vice President
      Integral Technologies Inc.
      415 E. Plaza Drive
      Westmont, IL 60559

269. Frederick E. Moreno, President
      Turbo Energy Systems, Inc.
      350 Second Street, Suite 5
      Los Altos, CA 94022

270. Peter E. D. Morgan
      Member Technical Staff
      Structural Ceramics
      Rockwell International
      Science Center
      1049 Camino Dos Rios
      PO Box 1085
      Thousand Oaks, CA 91360

271. Solomon Musikant
      General Electric Company
      Space Systems Division
      PO Box 8555, Mail Stop U-1219
      Philadelphia, PA 19101

272. Pero Nannelli
      Pennwalt Corporation
      900 First Avenue, PO Box C
      King of Prussia, PA 19406-0018

273. Robert M. Neilson, Jr.
      EG&G Idaho, Inc.
      Materials Research
      PO Box 1625
      Idaho Falls, ID 83415

274. Dale E. Niesz
      Manager, Materials
         Department
      Battelle Columbus
         Laboratories
      505 King Avenue
      Columbus, OH 43201

275. William D. Nix
      Stanford University
      Dept. of Materials Science
         and Engineering
      Stanford, CA 94305

276. Dick Nixdorf
      Vice President
      American Matrix, Inc.
      118 Sherlake Drive
      Knoxville, TN 37922

277. Norton Company
      HPC Library/D. M. Jacques
      Goddard Road
      Northboro, MA 01532-1545

278. W. Richard Ott
      New York State College of
         Ceramics
      Alfred University
      Alfred, NY 14802

279. Muktesh Paliwal
      GTE Products Corporation
      Hawes Street
      Towanda, PA 18848

280. Hayne Palmour III
      North Carolina State
         University
      Engineering Research
         Services Division
      2158 Burlington Engineering
         Laboratories
      PO Box 5995
      Raleigh, NC 27607

281. Joseph N. Panzarino
Norton Company
Director, R&D, High Performance
  Ceramics
Goddard Road
Northboro, MA 01532-1545

282. Pellegrino Papa
Manager, Technical and Business
  Development
Corning Technical Products
  Division
Corning Glass Works
Corning, NY 14831

283. James G. Paschal
Chemical Sales, Regional Manager
Reynolds Metals Company
PO Box 76154
Atlanta, GA 30358

284. Arvid E. Pasto
Member of Technical Staff
Precision Materials Technology
GTE Laboratories, Inc.
40 Sylvan Road
Waltham, MA 02254

285. James W. Patten
Director, Materials Engineering
Cummins Engine Company, Inc.
Box 3005, Mail Code 50183
Columbus, IN 47201

286. Robert A. Penty
Development Engineer
Manufacturing Technology Dept.
Apparatus Div.
Eastman Kodak Company
901 Elmgrove Road
Rochester, NY 14650

287. Gary R. Peterson
U.S. Department of Energy
Idaho Operations Office
785 DOE Place
Idaho Falls, ID 83402

288. Dan Petrak
Babcock and Wilcox
PO Box 1260
Lynchburg, VA 24505

289. R. Byron Pipes
University of Delaware
Center for Composite
  Materials
2001 Spencer Laboratory
Newark, DE 19716

290. Robert C. Pohanka
Office of Naval Research
800 N. Quincy Street
Code 431
Arlington, VA 22217

291. Stephen C. Pred
Product Manager
ICD Group, Inc.
641 Lexington Avenue
New York, NY 10022

292. Karl M. Prewo
United Technologies Corp.
Research Center
Silver Lane, MS 24
East Hartford, CT 06108

293. Hubert B. Probst
Chief Scientist, Materials
  Div., MS 49-1
NASA Lewis Research Center
21000 Brookpark Road
Cleveland, OH 44135

294. Carr Lane Quackenbush
Norton Company
High Performance Ceramics
Goddard Road
Northboro, MA 01532-1545

295. George Quinn
U.S. Army Materials
  Technology Laboratory
Arsenal Street
Watertown, MA 02172

296. Dennis T. Quinto
Kennametal, Inc.
Phillip M. McKenna
  Laboratory
PO Box 639
Greensburg, PA 15601

297. S. Venkat Raman
Manager, New Technology
    Marketing
Contract Research Dept.
Air Products and Chemicals, Inc.
PO Box 538
Allentown, PA 18105

298. Dennis Readey
Department Chairman
    Ceramic Engineering
Ohio State University
2041 College Road
Columbus, OH 43210

299. Robert R. Reeber
U.S. Army Research Office
PO Box 12211
Research Triangle Park, NC 27709

300. K. L. Reifsnider
Virginia Polytechnic Institute
    and State University
Department of Engineering
    Science and Mechanics
Blacksburg, VA 24061

301. Paul Rempes
Champion Spark Plug Company
Ceramic Division
20000 Conner Avenue
Detroit, MI 48234

302. T. M. Resetar
U.S. Army Materials Technology
    Laboratory
DRXMR-MC
Arsenal Street
Watertown, MA 02472

303. K. T. Rhee
Rutgers University
College of Engineering
PO Box 909
Piscataway, NJ 08854

304. Roy W. Rice
W. R. Grace and Company
7379 Route 32
Columbus, MD 21044

305. David W. Richerson
Ceramatec, Inc.
163 West 1700 South
Salt Lake City, UT 84115

306. Paul Rieth
Ferro Corporation
661 Willet Road
Buffalo, NY 14218

307. Michael A. Rigdon
Institute for Defense
    Analyses
1801 Beauregard Street
Alexandria, VA 22311

308. John E. Ritter, Jr.
University of Massachusetts
Mechanical Engineering
    Department
Amherst, MA 01003

309. Giulio A. Rossi
Norton Company
High Performance Ceramics
Goddard Road
Northboro, MA 01532-1545

310. Barry R. Rossing
Aluminum Company of America
Alcoa Technical Center
Alcoa Center, PA 15069

311. David J. Rowcliffe
SRI International
333 Ravenswood Avenue
Menlo Park, CA 94025

312. Donald W. Roy
Manager, Carbide and
    Optical Material
Research and Development
Coors Porcelain Company
Golden, CO 80401

313. Bruce Rubinger
Gobal
50 Milk Street, 15th Floor
Boston, MA 02109

314. Robert Ruh
Air Force Wright
    Aeronautical Laboratory
Materials Laboratory,
    AFWAL/MLLM
Metals and Ceramics
    Division
Wright-Patterson AFB,
    OH 45433

315. Robert J. Russell, Sr.
Divisional Vice President
Technology and Planning
High Performance Ceramics
Norton Company
Goddard Street
Northboro, MA 01532-1545

316. George P. Safol
Westinghouse Electric
Corporation
R&D Center
Pittsburgh, PA 15235

317. J. Sankar
North Carolina Agricultural and
Technical State University
Department of Mechanical
Engineering
Greensboro, NC 27411

318. Maxine Savitz
Assistant to Vice President,
Engineering
The Garrett Corporation
PO Box 92248
Los Angeles, CA 90009

319. Richard Schapery
Texas A&M University
Civil Engineering Department
College Station, TX 77843

320. J. L. Schienle
Garrett Turbine Engine Company
111 S. 34th Street
Phoenix, AZ 85034

321. L. J. Schioler
Aerojet Tech Systems Company
PO Box 13222
Dept. 9990, Bldg. 2001
Sacramento, CA 95813

322. Arnie Schneck
Deere and Company
PO Box 128
Wood-Ridge, NJ 07075

323. Matthew Schreiner
Project Manager
Ceramic Materials
and Components
Gas Research Institute
8600 W. Bryn Mawr Avenue
Chicago, IL 60631

324. John Schuldies
Industrial Ceramic
Technology, Inc.
141 Enterprise Drive
Ann Arbor, MI 48103

325-345. R. B. Schulz, Manager
Advanced Materials
Development
Office of Transportation
Systems
Department of Energy
Forrestal Building CE-151
1000 Independence Avenue
Washington, DC 20585

346. Wesley J. C. Schuster,
President
Thermo Electron Corporation
Metals Division
115 Eames Street
PO Box 340
Wilmington, MA 01887

347. Murray A. Schwartz
Bureau of Mines
2401 Eye Street, NW
Washington, DC 20241

348. Douglas B. Schwarz
Dow Chemical U.S.A.
52 Building
Midland, MI 48674

349. Thomas M. Sebestyen
U.S. Army Tank-Automotive
Command
AMSTA-RGRT
Warren, MI 48397-5000

350. Brian Seegmiller
Senior Development Engineer
Coors Porcelain Company
17750 North 32 Street
Golden, CO 80401

351. S. G. Seshadri
Research Associate
Standard Oil Engineered Materials
  Company
Niagara Falls R&D Center
PO Box 832
Niagara Falls, NY 14302

352. Peter T. B. Shaffer
Executive Vice President
Advanced Refractory Technologies,
  Inc.
699 Hertel Avenue
Buffalo, NY 14207

353. Maurice E. Shank
Director, Engineering Technology
  Assessment
United Technologies Corporation
Pratt and Whitney Engrg. Div.
MS 162-31
East Hartford, CT 06108

354. Laurel M. Sheppard
Associate Editor
Advanced Materials and Processes
Route 87
Metals Park, OH 44073

355. Dinesh K. Shetty
The University of Utah
Dept. of Materials Science and
  Engineering
Salt Lake City, UT 84112

356. Jack D. Sibold
Coors Porcelain Company
17750 North 32 Street
Golden, CO 80401

357. Neal Sigmon
Appropriations Committee
Subcommittee on Interior and
  Related Events
U.S. House of Representatives
Rayburn Building, Room B308
Washington, DC 20515

358. Richard Silberglitt
DHR, Inc.
6849 Old Dominion Drive
Suite 228
McLean, VA 22101

359. Maurice J. Sinnott
University of Michigan
Chemical and Metallurgical
  Engineering
438 W. Engineering Building
Ann Arbor, MI 48109

360. S. R. Skaggs
Los Alamos National
  Laboratory
PO Box 1663
MS F-682, Program Office
Los Alamos, NM 87545

361. J. Thomas Smith
Director, Precision
  Materials Tech.
GTE Laboratories, Inc.
40 Sylvan Road
Waltham, MA 02254

362. Jay R. Smyth
Senior Development Specialist
Garrett Turbine Engine
  Company
PO Box 5217
MS 93-172/1302-2K
Phoenix, AZ 85010

363. Rafal Sobotowski
Standard Oil Engineered
  Materials
Research and Development
3092 Broadway Avenue
Cleveland, OH 44115

364. Boyd W. Sorenson
E. I. DuPont de Nemours
  & Company
Textile Fibers Dept. —
  E304C123
Wilmington, DE 19898

365. Richard M. Spriggs
National Materials Advisory
  Board
National Research Council
2101 Constitution Avenue
Washington, DC 20418

366. John D. Spuller
Division Manager
  Government Products
Deere and Company
John Deere Road
Moline, IL 61265

367. M. Srinivasan
Standard Oil Engineered
  Materials
Niagara Falls R&D Center
PO Box 832
Niagara Falls, NY 14302

368. Gordon L. Starr
Manager, Metallic/Ceramic
  Materials Dept.
Cummins Engine Company, Inc.
Box 3005, Mail Code 50183
Columbus, IN 47202-3005

369. Harold L. Stocker
Manager, Low Heat Rejection
  Program
General Motors Corporation
Allison Gas Turbine Operations
PO Box 420, T-23
Indinapolis, IN 46206-0420

370. Roger Storm
Director, Niagara Falls R&D
  Center
Standard Oil Engineered Materials
  Company
PO Box 832
Niagara Falls, NY 14302

371. E. E. Strain
Program Manager AGT-101
Garrett Turbine Engine Company
111 S. 34th Street
PO Box 5217, Mail Stop 301-2N
Phoenix, AZ 85010

372. Thomas N. Strom
NASA Lewis Research Center
21000 Brookpark Road, 77-6
Cleveland, OH 44135

373. Richard Suddeth
Boeing Motor Airplane Company
PO Box 7730, MS K-76-67
Wichita, KS 67277

374. Paul Sutor
Midwest Research Institute
425 Volker Blvd.
Kansas City, MO 64116

375. J. J. Swab
U.S. Army Materials
  Technology Laboratory
Ceramics Research Division
Arsenal Street
Watertown, MA 02172

376. Lewis Swank
Ford Motor Company
PO Box 2053
Building SRL, Room E3172
Dearborn, MI 48121

377. Anthony C. Taylor
Staff Director,
  Subcommittee on
  Transportation, Aviation,
  & Materials
Committee on Science and
  Technology
U.S. House of Representative
Rayburn Building, Room 2321
Washington, DC 20515

378. W. H. Thielbahr
Chief, Energy Programs
  Branch
Department of Energy
Idaho Operations Office
550 2nd Street
Idaho Falls, ID 83401

379. John K. Tien
Director of Center for
  Strategic Materials
Columbia University
1137 SW Mudd Building
New York, NY 10027

380. T. Y. Tien
University of Michigan
Materials and Metallurgical
  Engineering
Dow Building
Ann Arbor, MI 48109-2136

381. Julian M. Tishkoff
Air Force Office of Scientific
   Research
Directorate of Aerospace Sciences
Bolling AFB
Washington, DC 20332

382. Louis E. Toth
National Science Foundation
Division of Materials Research
1800 G Street, NW
Washington, DC 20550

383. Richard E. Tressler
Chairman, Ceramic Science and
   Engineering Department
The Pennsylvania State University
201 Steidle Building
University Park, PA 16802

384. Donald R. Uhlmann
Professor, Ceramics and Polymers
Department of Materials Science
   and Engineering
Massachusetts Institute of
   Technology
Cambridge, MA 02139

385. Edward C. van Reuth
President
Technology Strategies, Inc.
10722 Shingle Oak Court
Burke, VA 22015

386. Thomas Vasilos
Manager, Electro Chemical
   Facility
Avco Corporation
201 Towell Street
Wilmington, MA 01887

387. V. Venkateswaran
Standard Oil Engineered Materials
   Company
PO Box 832
Niagara Falls, NY 14302

388. John B. Wachtman, Jr.
Director, Center for Ceramics
   Research
Rutgers University
PO Box 909
Piscataway, NJ 08854

389. Richard B. Wallace
Manager, Government
   Research and Development
   Programs
General Motors Corporation
Detroit Diesel Allison
   Division
36880 Ecorse Road
Romulus, MI 48174

390. Harlan L. Watson
Subcommittee on Energy
   Research and Production
U.S. House of Representatives
Committee on Science and
   Technology
Rayburn Building
Suite 2321
Washington, DC 20515

391. Steven G. Wax
Department of Defense
Advanced Research Projects
   Agency
Materials Science Division
1400 Wilson Boulevard
Arlington, VA 22209

392. Albert R. C. Westwood
Corporate Director, R&D
Martin Marietta Laboratories
1450 South Rolling Road
Baltimore, MD 21227

393. Thomas J. Whalen
Principal Research Scientist
Ford Motor Company
Scientific Lab, Room 2023
Dearborn, MI 48121

394. Sheldon M. Wiederhorn
U.S. Department of Commerce
National Bureau of Standards
Inorganic Materials Division
Mechanical Properties Group
Gaithersburg, MD 20899

395. James C. Williams
Dean, Carnegie Institute of
   Technology
Carnegie-Mellon University
Schenley Park
Pittsburgh, PA 15213

396. Roger R. Wills
Manager, Advanced Ceramic
Components
TRW, Inc.
Automotive Worldwide Sector,
Valve Division
Cleveland, OH 44110

397. J. M. Wimmer
Supervisor, Nonmetallic Materials
Group
Garrett Turbine Engine Company
111 S. 34th Street, PO Box 5217
Phoenix, AZ 85010

398. David Wirth
Vice President, Technical
Operations & Engineering
Coors Porcelain Company
17750 North 32 Street
Golden, CO 80401

399. Thomas J. Wissing
Manager, Government Contract
Administration
Eaton Corporation
Engineering & Research Center
26201 Northwestern Highway
PO Box 766
Southfield, MI 48037

400. George W. Wolter
Howmet Turbine Components
Corporation
Technical Center
699 Benston Road
Whitehall, MI 49461

401. James C. Wood
NASA Lewis Research Center
21000 Brookpark Road
MS 500-210
Cleveland, OH 44135

402. Hun C. Yeh
Ceramic Supervisor
AiResearch Casting Company
19800 Van Ness Avenue
Torrance, CA 90509

403. Thomas M. Yonushonis
Cummins Engine Company, Inc
Box 3005, Mail Code 50183
Columbus, IN 47202-3005

404. Don Zabierek
Air Force Wright
Aeronautical Laboratory
AFWAL/POTC
Wright-Patterson AFB,
OH 45433

405. Charles Zeh
Department of Energy
Morgantown Energy
Technology Center
PO Box 880
Morgantown, WV 26505

406. Klaus M. Zwilsky
Executive Director
National Materials
Advisory Board
National Research Council
2101 Constitution Avenue
Washington, DC 20418

407. Department of Energy
Oak Ridge Operations Office
Assistant Manager for
Energy Research and
Development
PO Box E
Oak Ridge, TN 37831

408-437. Department of Energy
Technical Information
Center
Office of Information
Services
PO Box 62
Oak Ridge, TN 37831

For distribution by
microfiche as shown in
DOE/TIC-4500,
Distribution Category UC-95.